AD-A233 957

MICROMECHANICS ANALYSIS OF FIBER TOUGHENING IN CERAMIC-MATRIX COMPOSITES[+]

C.D. Balis[*] and S.S. Wang[**]

December, 1989

National Center for Composite Material Research
at University of Illinois, Urbana - Champaign
A DoD University Research Initiatives Center funded by the
Office of Naval Research, Arlington, VA

91 3 27 104

ABSTRACT

The finite element method combined with elasticity results governing fiber pullout is used to investigate toughening of unidirectional fiber-reinforced ceramic matrix composites. The most important literature concerned with toughening of refractory fiber-reinforced ceramic matrix composites is reviewed, including both experimental attempts to produce tougher composites and analytical models to predict and describe the toughening mechanisms. The primary toughening mechanisms include crack-bridging, crack-tip/fiber interaction and crack front bowing. Of these, the bridging and interaction, which are idealistically two-dimensional mechanisms, dominant the toughening and control the third bowing mechanism. A two-dimensional elasticity solution governing the fiber pullout mechanics of crack bridging is presented and applied in a two-dimensional finite element toughening model. This model includes both the crack bridging coupled with the crack-tip/fiber interaction mechanisms and is used to investigate the role of various parameters in the composite toughening. In addition, certain stresses of interest governing crack propagation are reported. The investigated parameters include fiber/matrix stiffness ratio, interfacial friction coefficient, crack-tip position and remote applied load. It is found that crack bridging is the dominant mechanism and the toughening in the bridged composite is strongly dependent on stiffness ratio, crack tip position and remote applied load. Additionally, the stress results indicate that crack propagation in the bridged composite is controlled only by very local crack tip effects, while propagation in an unbridged composite may be more of a structural phenomena. The predicted toughening results agree well with the limited experimental results in the literature.

TABLE OF CONTENTS

1. INTRODUCTION

Recently, a large degree of effort has been focused on the problem of toughening structural ceramics, particularly in the region of ultra-high temperature applications. Fiber, whisker and particulate reinforcements as well as transformation toughening are the most popular toughening routes being pursued. Among these various approaches, fiber toughening currently shows the most promise for producing not only a tougher, stronger and most importantly, a gently failing ceramic composite, but also one which behaves in a more deterministic manner (as opposed to the probablistic behavior of monolithic ceramics). The literature survey of this paper summarizes some of the attempts to produce successful refractory fiber toughened ceramics.

A typical (idealized) longitudinal tensile stress-strain curve of a unidirectional, continuous fiber-reinforced ceramic composite is shown in Fig. 1.1. The unreinforced ceramic matrix exhibits complete linear-elastic behavior and fails catastrophically at a low strain (0.1-0.2% typically). The fiber reinforced ceramic exhibits linear-elastic behavior up to the matrix microcracking stress. At this point, multiple cracks bridged by intact fibers form in the matrix and softer, nonlinear stress-strain behavior is developed. Continued loading is essentially carried by the bridging fibers and eventually causes the fibers to fail, leading to the composite fracture with an ultimate strain generally greater than 0.5%.

Although the increase in ultimate strength and strain depicted in Fig. 1.1 are important concerns for improving properties of fiber reinforced ceramics, currently the most critical, life limiting issue for thermo-structural applications is the matrix microcracking stress. Before the matrix cracks it protects the fibers and the interface from the hot oxidizing environment.

Once the matrix cracks, the environment penetrates to the fibers and interface region with subsequent degradation of both the fiber and the interface. This typically leads to fiber weakening and the formation of a strong fiber-matrix bond, causing the composite to fracture in a brittle fracture mode.

Adequate understanding of the fiber toughening mechanism provides proper control of matrix microcracking, and becomes paramount to the successful production and employment of fiber-reinforced ceramics. Although crack propagation in fiber reinforced ceramics is physically a complicated process, stable matrix cracking and growth often observed during microcracking may be modeled conveniently as a repeating sequence of three major steps. The three steps are shown in Figs. 1.2a through 1.2c, where the fibers are idealized as arranged so that on the x_2-x_3 plane they appear in a periodic (e.g., square) array. In the first step, the crack is propagating along the x_2-x_3 plane so that the crack front is parallel to and between two rows of fibers. Interface debonding and slipping along the fiber-matrix interface may occur so that the fibers behind the crack front are bridging the crack as shown in Fig. 1.2a. As the crack progresses forward, the regions of the crack front with fibers in their path experience a lower stress intensity factor K_I [25-28] compared to those regions with free paths, due to the restraining effect of the fibers. This variation in K_I along the crack front causes it start bowing as it moves closer to the fiber, as shown in Fig. 1.2b.

When the crack reaches the fibers, the matrix is now disconnected at the fibers and the interface slips or debonds so that the crack front is essentially broken into a series of arcs between the fibers, as shown in Fig. 1.2c. As the bows move forward, their ends move around the fibers. At some

point the periodic bowing crack fronts reach their maximum, critical bowing depth and the ends of the bows touch, forming one united crack front again. The row of fibers originally in front of the crack have passed through and are now bridging the crack. The crack front straightens as it progresses and returns to the configuration of Fig. 1.2a.

Many coupled three-dimensional toughening mechanisms occur in the idealized sequence outlined above. The dominant mechanisms include, among others, crack bridging and crack-tip/fiber interactions. The literature survey of this paper covers the major attempts to model some of these toughening mechanisms. Unfortunately, many of these models suffer from unrealistic simplifications and/or ignore coupling between different mechanisms.

The object of this research is to model the two dominant longitudinal toughening mechanisms in fiber reinforced ceramics, i.e., crack bridging and crack-tip/fiber interaction, in an accurate manner which also includes coupling effects. Because the crack bridging generally involves fiber pullout, an additional effort is made to understand and apply the mechanics of the pullout process. In next chapter, the important relevant literature is reviewed, including both experimental attempts to produce successful refractory composites and analytical approaches to model the toughening mechanisms. The mechanics of two-dimensional fiber pullout are studied in Chapter 3 and analytical solutions governing the pullout process are derived. In Chapter 4, a two-dimensional toughening analysis is conducted, employing the pullout results of Chapter 3. Conclusions of the research are presented in Chapter 5.

2. LITERATURE REVIEW

Thorough understanding of the fiber crack bridging process has helped to produce significant recent successes in developing tough fiber-reinforced ceramics, as shown in the experimental review below. It is now understood that a tough, low-stiffness matrix, coupled with strong, high-stiffness, small diameter fibers and a weak fiber/matrix interface are essential to raise the matrix microcracking stress and to promote crack bridging in a brittle ceramic composite. Crack bridging, although dominant, however, is not the only significant toughening mechanism of fiber-reinforced ceramics. Analytical models describing crack bridging and other toughening mechanisms are reviewed in the second half of this chapter.

2.1 EXPERIMENTAL APPROACH

The interface condition necessary for successful crack bridging (and resulting stress-strain response depicted in Fig. 1.1) is usually manifested in a thin carbon layer between the fiber and matrix. Many glass ceramic matrices can be tailored (depending on fiber surface chemistry) to promote the formation of a carbon fiber-matrix interface, with the result that successful fiber-reinforced glass ceramics have been produced without undue difficulty. However, these composites are limited in high-temperature capabilities by their glass matrices. To extend the high-temperature capabilities of fiber-reinforced ceramics, recent attempts have focused on the use of polycrystalline silicon-based ceramics (SiC and Si_3N_4) as matrix materials, particularly on Si_3N_4 because of its high toughness, strength and low stiffness. Although these polycrystalline ceramic materials generally have high stiffness and are difficult to process (compared to glass ceramics), they are attractive as matrix

4

materials both because of their refractoriness and their high strength and fracture toughness.

2.1.1 Fiber—Reinforced Si_3N_4 Ceramics

Attempts [3-7] to produce Si_3N_4 based composites use both hot-pressed Si_3N_4 matrices and reaction-bonded Si_3N_4 (RBSN) matrices reinforced with either polymer-precursor (Nippon Carbon Co. NICALON) or chemical vapor deposition (CVD) (Avco SCS-2 and SCS-6) SiC fibers. The NICALON and SCS fibers by way of their fabrication methods differ considerably physically, chemically and mechanically, as summarized by DiCarlo [1]. The SCS fibers have a large diameter (143 micron), a pyrolitic carbon core and a thin outer carbon coating. The main body of the SCS fibers, however, is near stoichiometric SiC. This high chemical purity of the SCS fibers is reflected in their high modulus (400 GPa) and strength (near 4 GPa). The NICALON fibers, conversely, have a small diameter (15 micron) and a microstructure containing SiO_2 and excess carbon [1] These impurities result in a low stiffness (180 GPa) and strength (2 GPa), as well as reduced thermal stability [2].

Rice et. al. [3] investigate NICALON reinforced hot-pressed silicon nitride and find a small improvement in strength. However, the high fabrication temperature required both degrades the NICALON fiber (through grain growth) and facilitates a strong fiber-matrix bond [3], limiting the improvement in composite properties. Shetty et. al. [4] utilize a similar hot-pressed Si_3N_4 matrix but incorporate the SCS-6 fibers as reinforcements. Their results are successful in that a weak carbon interface layer is maintained, allowing the fiber bridging to occur. The SCS-6/hot-pressed Si_3N_4 composite shows increased toughness (greater than 8 MPa$\sqrt{m}$ at 30% V_f) and graceful failure; however, the composite ultimate strength is nearly half of the monolithic hot-

pressed Si_3N_4 [4]. This reduction in strength is mainly attributed to the change in fiber microstructure, indicating that, similar to the Rice et. al. study with NICALON fibers [3], the high fabrication temperatures required for hot-pressing Si_3N_4 degrade the reinforcing fibers.

To avoid the problems associated with the hot-pressed SiC/Si_3N_4 composites, Bhatt and Phillips [5] use a RBSN matrix reinforced with SCS-6 fibers, and Corbin, Rossetti and Hartline [6] use a similar matrix reinforced with both SCS-6 and SCS-2 fibers. The SCS-2 fibers are identical to the SCS-6 fibers except that they have a thinner (approximately 60%) outer layer of carbon [6]. The RBSN is attractive as a matrix material because of its lower processing temperature (1450°C), lower modulus and higher creep resistance [6] relative to the hot-pressed Si_3N_4 (typically processed at 1750°C with glassy densification aids). In both investigations, excellent properties of the SCS-6 reinforced composite are obtained with a typical strength near 700 MPa ($\epsilon_f \approx$ 0.5%) [5] for $V_f = 30\%$ and in some cases, the strength exceeds 900 MPa ($\epsilon_f >$ 0.5%) [6] for 50% V_f. (Strength of a comparable monolithic RBSN is approximately 350 MPa ($\epsilon_f \approx .18\%$) [6].) Composites utilizing the SCS-2 fibers [6] show a slight improvement in strength of near 450 MPa ($\epsilon_f > 0.5\%$). The difference in strength between the SCS-6 and the SCS-2 fiber-reinforced materials demonstrates the importance of the carbon interface layer.

In an attempt to produce a successful NICALON/RBSN composite, Corbin, Willkens and Hartline [7] coat the thinner NICALON fibers by a CVD method with several materials before composite fabrication. Composites containing uncoated, Si_3N_4-coated, Al_2O_3-coated and SiC-coated fibers all fail catastrophically in a brittle fracture mode, while carbon-coated composites fail gracefully ($\epsilon_f \approx 0.5\%$), again demonstrating the importance of the weak carbon

interface. The strength of the carbon-coated NICALON-reinforced composites is only about 400 MPa, a reflection of the weaker NICALON fibers.

2.1.2 Fiber—Reinforced SiC Ceramics

The recent developments of SiC/RBSN composites, however, have also been accompanied by some successes with SiC-fiber reinforced, chemical-vapor-infiltration (CVI) SiC composites. The CVI SiC as a matrix material has, much like RBSN, certain advantages over its hot-pressed counterpart. These advantages include lower fabrication temperatures (1200°C), lower modulus and higher creep resistance (again due to the absence of glassy densification aids).

NICALON-reinforced CVI SiC composites have been investigated by several researchers [8-10]. Stinton, Caputo and Lowden [8] and Lamicq et. al. [9] observe composite strengths between 250 MPa and 350 MPa while Moeller et. al. [10] obtain a strength greater than 600 MPa by using a different processing technique. Extensive fiber pullout and large failure strains (near 1.0%) are observed in all three investigations [8-10], reflecting good interface properties. Moeller et. al. find the composite strength drops to near 200 MPA at an elevated temperature of 1200°C while Lamicq et. al. actually observe a slight increase in composite strength to greater than 300 MPa up to 1400°C. Additionally, Moeller et. al. [10] determine that CVD coating the NICALON fibers with carbon prior to infiltration of the matrix increases the composite strength only slightly to near 690 MPa at room temperature.

Fitzer and Gadow [11] investigate a variety of SiC-based composites, using both CVI and reaction-bonded SiC matrices reinforced with NICALON, SCS-6 and carbon fibers. The SCS-6 reinforced materials exhibit the highest strengths of 950 MPa and 600 MPa for the composites with CVI and RB SiC

7

matrices respectively. But, good fiber-matrix bonding results from both processing methods so that failure is mostly catastrophic for all unidirectional composites, as indicated by the small (0.2%) failure strain.

2.1.3 Experimental Summary

The success of Moeller et. al. [10] and the limited progress of Stinton, Caputo and Lowden [8] and Lamicq et. al. [9] suggest that the SiC/CVI-SiC composites are also promising, although the SiC/RBSN, particularly the SCS-6/RBSN, composites (e.g., [5] and [6]) have been more successful. Despite these successes (where testing temperatures have typically been limited to 1200°C), however, it is important to recognize, as is noted by DiCarlo [1], currently there exist no truly satisfactory fibers for refractory ceramic reinforcement applications. Also of concern, as mentioned before, is the vulnerability of the all-important carbon interface layer (once matrix cracks have formed). For fiber-reinforced ceramics to become truly reliable and useful materials, then these goals (among others) need to be met: development of strong, stiff, small-diameter fibers which retain their strength both during composite fabrication and when exposed to a refractory air environment; and innovative approaches to either protect the carbon interface from environmental exposure after matrix microcracking or to develop more stable diffusion barriers to control fiber-matrix bonding.

2.2 ANALYTICAL APPROACH -- TOUGHENING MODELS

Reinforced ceramics are unique in the field of composite materials because the major constituents, the fiber and matrix, generally exhibit similar (in contrast to fiber-reinforced polymer matrix composites), linear-elastic stress-strain responses up to failure for most loading modes (creep loading

8

being an obvious exception). The linear behavior allows not only the use of simple stress-strain and energy-balance laws, but, in some cases, permits the use of linear-elastic fracture mechanics (LEFM) for modeling purposes. Thus, many of the models surveyed below are based on applications of elastic energy-balance formulations and basic, often classical LEFM solutions.

Various mechanisms of the idealized sequence outlined in Fig. 1.2 have been modeled in the literature. These models have been grouped below in the following categories: the crack-bridging models, which model one aspect of Fig. 1.2, the inclusion-interaction models, which are concerned with portions of both Fig. 1.2b and Fig. 1.2c., and the crack-bowing models, which describe the breakaway bowing configuration in Fig. 1.2c.

2.2.1 Crack-Bridging Models

The first crack-bridging model, commonly called the ACK theory of microcracking, was introduced by Aveston, Cooper and Kelly [12] in 1971. Assuming a crack is completely bridged by stronger fibers, they use an energy-balance analysis to determine the first matrix microcracking strain as

$$\epsilon_{mu} = \left[\frac{24\tau_o G_m E_f V_f^2}{E_c E_m^2 d_f (1-V_f)} \right]^{1/3} \tag{2.1}$$

where ϵ_{mu} is the matrix microcracking strain, τ_o is the interfacial sliding shear stress, E_m, E_f and E_c are the moduli of the matrix, fiber and composite, respectively, d_f is the diameter of the fibers, V_f is the volume fraction of fibers, and G_m is the matrix energy release rate. According to this model, ϵ_{mu} is <u>independent</u> of the total crack length a_o; rather, the microcracking strain is controlled by the <u>fiber diameter</u> d_f. This behavior is commonly referred to as <u>steady-state</u> microcracking or crack-bridging, due to the invariance of the microcracking criteria with crack growth, and the resulting stability of that

9

growth. Additionally, according to Eq. (2.1), ϵ_{mu} increases as τ_o, G_m, E_f and V_f increase and as E_m decrease. Although this model predicts with reasonable accuracy the microcracking stresses observed in experiments [12,13], it does contain certain ideological deficiencies. For example, fiber-matrix interfaces more realistically exhibit stick/frictional slip behavior rather than a purely frictional response. Also, as seen in experiments, as interface strength is increased the fibers will pass, rather than bridge the crack. In this case, the microcracking stress of the composite is maximum, but the toughness of the composite is decreased as catastrophic failure of the composite occurs. However, despite its limitation in actual physical processes, the ACK model is important for two reasons: its simple formulation helps to give an understanding of the basic fiber-bridging process, and it introduces the first steady-state (i.e., crack-length independent) microcracking criteria. The steady-state cracking concept is further developed in the later crack-bridging models reviewed below.

In 1985, Marshall, Cox and Evans [13] (MCE) used a combined shear-lag/fracture mechanics analysis to model a completely bridged matrix crack as an edge crack in an isotropic, homogeneous plate with closure tractions on the crack surface. The fibers are assumed to be frictionally constrained in the matrix and the pullout relationship for the bridging fibers is of the form F α $\sqrt{v_o}$, where F is the pullout force on the end of a fiber and v_o is the matrix crack opening displacement. This relationship is based on a questionable, assumed variation of interfacial shear stress that is constant along the slipping length of the fiber and zero elsewhere. A linear-elastic fracture mechanics concept is used to predict a matrix microcracking stress for steady-state crack growth similar to that predicted by the ACK energy-balance

derived model [12] in Eq. (2.1). However, the fracture mechanics formulation adopted in [13] also reveals the behavior of the stress intensity factor K_I at the crack tip. The K_{tip} is found to be a strong function of the crack length a_o only for short cracks. As the crack grows in length, the K_{tip} asymptotically approaches the constant steady-state bridging stress intensity factor K_{ss}, for a given remote applied load. For a crack length typically greater than ten fiber diameters, K_{tip} is nearly equal to K_{ss} and thus independent of crack length, indicating stable crack growth. For long (e.g., steady-state) cracks, K_{tip} is controlled by the fiber size, rather than the total crack length, in a manner similar to Eq. (2.1). Additionally, the ratio K_{tip}/K_{rem}, where $K_{rem} = \sigma_c \sqrt{(\pi a_o)}$ is related to the total crack length and the external applied load σ_c, is less than unity for all crack lengths, indicating macroscopic toughening. Although this fracture mechanics model suffers from realistic limitations similar to the ACK model, (isotropic homogeneity is an obvious assumption here) it is an important model for two reasons: it discloses the nature of K_{tip} and its dependence on crack length and material properties, and it validates the steady-state growth assumptions (i.e., a crack-length independent solution exists) implicit in the ACK energy-balance analysis.

In 1986 Budiansky, Hutchinson and Evans [14] (BHE) use a more rigorous energy-based fracture mechanics approach to examine the steady-state bridging process with both bonded/debonding fibers and unbonded frictionally sliding fibers. The focus of the BHE analysis is on the large-slip (i.e. small interface toughness/friction) and no-slip (no-debonding/no-sliding for large interface toughness/friction) solutions and the transition between these two modes. The large-slip solution is identical to the ACK [12] microcracking model, and describes a composite with a large failure strain and

high toughness. Conversely, the no-slip condition produces the highest microcracking stress, but not the highest composite toughness. The BHE formulation describes the transition between these two modes (maximum toughness and maximum microcracking stress) in terms of interface properties. The no-debonding condition occurs typically for G_d greater than $\approx G_m/5$, where G_d and G_m are the debonding and matrix fracture energy release rates, while the no-sliding condition is dependent on material properties, friction coefficient, and residual thermal stresses. Thus, the BHE steady-state crack-bridging model expands the ACK [12] model by the addition of the debonding interface consideration and the recognition and quantification of interface properties (friction or toughness) that cause a transition to the no-slip (maximum microcracking stress) mode.

Budiansky and Amazigo [15] (BA) model a steady-state bridged crack as reinforced by distributed springs, a fracture mechanics technique developed by Rose [16], to investigate the frictional interface fiber bridging in terms of the large-slip and no-slip conditions. The BA model contains the important elements from the previous bridging models [12-14]. It includes the transition from large-slip to no-slip conditions (i.e. the BHE [14] model); its fracture mechanics formulation explicitly reveals K_{tip} (similar to the MCE [13] model), and additionally it allows orthotropic composite elastic properties. The authors present their results in an equally comprehensive manner that reveals the interplay between matrix microcracking strength, composite ultimate strength and composite fracture toughness. Generally as the microcracking strength is increased (by altering interface friction, fiber stiffness, etc) towards the composite ultimate strength (given by volume fraction * fiber strength) the composite toughness declines. This BA bridging model essentially represents

the most complete steady-state bridging model of the form introduced in the ACK [11] model.

Majumdar, Newaz and Rosenfield [17] (MNR) slightly modify the shear-lag model of the MCE steady-state bridging analysis [13] and account for crack interactions in an analysis essentially the same as the MCE model. The resulting pullout behavior, however, is of the same form as that used in the MCE model. If the parallel periodic microcracks in the composite are spaced too closely then the shear-lag cannot develop to its maximum value, essentially reducing the maximum bridging force the fibers can exert on the crack. The MNR approach shows that the constant K_{tip} for steady-state crack growth K_{ss} is then higher (for a given remote loading) and reached discontinuously, compared to the smoothly asymptotically approached value predicted by the MCE model. This K_{tip} behavior would result in discontinuous stress-strain response during composite "yielding" (microcracking), as is often seen in experiment. Although the shear-lag and crack interaction corrections are (realistically) important, this steady-state bridging model is essentially a refinement of the earlier MCE model and thus lacks the completeness and insight given by the later BA [15] model.

These steady-state fiber-bridging models, with the BA model being the most comprehensive, are essentially refinements of the original ACK model and its important concept of stable, crack-length independent microcracking. Despite its simplicity, the ACK [12] model gives surprisingly accurate predictions of the matrix microcracking stress. The later BA analysis [15], however, gives much more insight into the mechanics of fiber bridging. All frictionally sliding fiber-bridging models, however, employ the same unproved fiber pullout hypothesis derived in the MCE analysis.

2.2.2 Crack-Tip/Inclusion Interaction Models

A crack tip approaching an inclusion may interact through various mechanisms, including deflection of the crack and alteration of the crack-tip K_{tip}. These mechanisms are discussed below, with the second mechanism, alteration of K_{tip}, being broken into two sections covering particle and fiber effects. Mechanisms not considered here include, among others, crack branching, crack blunting and crack arrest.

2.2.2.1 Crack-Deflection Models

Theoretically, crack-deflection toughening occurs whenever interactions between the crack front and a second-phase inclusion cause the crack to propagate out of plane, reducing the stress intensity factor at the crack tip compared to self-similar planar crack growth. This toughening mechanism for different inclusions (spheres, rods and plates) is analyzed by Faber and Evans [18] (by using the method of quadratures [19] to predict the mode I and mode II stress intensity factors at the tip of a slightly kinked crack). Numerical results, predicting toughness increases for spherical and ellipsoidal inclusions, are conducted by Seshadri, Srinivasan and Keeler [20]. Both analyses [18,20] are simplistic in that they ignore the perturbed stress field introduced by the inclusions and also assume that the crack front progresses so as to globally deflect around the inclusions through a combination of tilting (the crack rotates about an axis parallel to the crack front) and twisting (the crack rotates about an axis parallel to the direction of crack propagation). In continuous fiber-reinforced ceramics although the crack tip may be locally deflected up and down along an approached debonding fiber, the progressing crack as a whole generally remains in-plane in a self-similar growth manner and passes fibers by a bowing rather than the deflecting mechanism, i.e., the

14

global crack deflection modeled in these analyses is not a toughening mechanism of interest for continuous fiber-reinforced ceramics.

2.2.2.2 Particulate-Interactions Models

Using Muskhelishvili complex variable methods, Tamate [21] investigates the problem of a crack in a plate approaching a circular inclusion for the case of a completely bonded inclusion with no residual stresses. Tamate [21] finds that the K_{tip} depends on, besides the geometrical parameters, the ratio of the elastic moduli of the particle and the matrix (E_p/E_m). If E_p/E_m is greater than unity, then the K_{tip} declines as the crack approaches the inclusion (compared to K_{tip} for a homogeneous plate); and, if E_p/E_m is less than unity, K_{tip} rises as the crack approaches the inclusion. The results [21] suggest that a material may be toughened in this manner, i.e. through lowering the crack-driving force, by adding stiffer inclusions.

Tirosh and Tetelman [22] and Khaund, Krstic and Nicholson [23] both extended, using an approximate image-stress formulation, the problem of a crack approaching a circular inclusion to allow for residual stresses due to an interference fit of the inclusion. Additionally, Tirosh and Tetelman [22] allowed for unbonded (frictionless interface) inclusions and examined, using finite element methods, the effect of a thin interface layer between the inclusion and the matrix. The results of both Tirosh and Tetelman [22] and Khaund, Krstic and Nicholson [23] for perfectly-bonded inclusions without residual stresses are similar to Tamate's [21]. Khaund, Krstic and Nicholson find that the effect of residual stresses for perfectly bonded inclusions is small, increasing or decreasing K_{tip} slightly depending upon whether the residual matrix hoop stress is tensile or compressive. If the inclusions are unbonded Tirosh and Tetelman find that K_{tip} increases with increasing

15

interference. Additionally, the finite element study of Tirosh and Tetelman

[22] on the effect of a finite thickness interface shows that as E_i/E_p, where E_i

is the interface modulus, decreases from unity, K_{tip} increases, reducing the

toughening effect. These results suggest that the toughening effect due to

particle/crack interaction (in the sense discussed here) can be maximized by

using stiff, well bonded inclusions with thermal expansion characteristics that

generate a compressive hoop stress in the matrix. Note that these particle

properties may not, however, be optimum for promoting other types of

particle/crack interactions, specifically crack bridging and crack deflection.

2.2.2.3 Fiber—Interaction Models

The problem of a crack tip approaching a finite-width fiber with various

interface conditions (perfectly bonded, bonded/debonding, frictional sliding,

etc) has not specifically been examined, to the author's knowledge, by any

investigators. However, certain related classical fracture mechanics solutions

lend insight into this problem. Zak and Williams [24] in 1963 first solved the

problem of a semi-infinite crack terminating at and normal to the interface in

a bimaterial plate containing isotropic phases. Zak and Williams used an

eigenfunction expansion technique to investigate the resulting stress

singularity at the crack tip. Rather than obeying the standard $1/\sqrt{r}$ crack tip

singularity, the stress follow a singularity that depends upon the ratios of

elastic properties of the two phases [24]. If E_2/E_1 is greater than unity,

where E_1 is the modulus of the first, cracked region and E_2 is the modulus of

the second, uncracked region, then the strength of the singularity is lessened

(compared to the $1/\sqrt{r}$ singularity). Similarly, if E_2/E_1 is less than unity, the

strength of the singularity is increased. Note that when the stresses do not

exhibit a $1/\sqrt{r}$ singularity the stress intensity factor K_{tip} is undefined, i.e. it

either becomes zero or infinite.

Solutions for finite-length cracks normal to and terminating at a bimaterial interface have been derived by Krapkov [25], using an asymptotic Weiner-Hopf technique, and Cook and Erdogan [26], who formulated a wedge problem solved by a Mellin transformation. The strength of the stress singularity determined by these [25,26] analyses follows trends similar to the Zak and Williams semi-infinite crack solution [24]. Additionally, Cook and Erdogan [26] determined the stress distributions in the cracked bimaterial plate.

Hilton and Sih [27] and later Cook and Erdogan [26] investigate problems of cracks terminating near (not touching) and normal to a bimaterial interface. Hilton and Sih, using integral transform methods, solve the symmetric problem of a Griffith crack lying in a finite width strip which is bounded at equal distances from each crack tip by a second material. The crack is normal to the bimaterial interfaces. This geometry is intended to represent a partially cracked layer in a laminated composite. Cook and Erdogan [26] again use a wedge solution method to consider the unsymmetrical problem of a finite length crack normal to the interface of a bimaterial plate. Although the geometry of these two problems [26,27] is different, the essential features of the solutions are the same. As the crack approaches the bimaterial interface, the stresses still obey a $1/\sqrt{r}$ singularity so that the stress intensity factor K_{tip} is suitably defined. The magnitude of K_{tip}, however, is dependent upon the elastic properties of the two plates. In a manner similar to the particulate/crack tip interaction results discussed in §2.2.2.2, if E_1/E_2 is greater than unity K_{tip} increases (compared to K_{tip} for a similar cracked homogeneous plate) while if E_1/E_2 is less than unity K_{tip}

17

decreases.

These results from the problems of a crack approaching and of a crack touching a bimaterial interface suggest that part of the toughening of fiber-reinforced ceramics may be due to the fiber/crack tip interaction discussed above. However, none of these works [24-27] specifically address the toughening issue for a fiber-reinforced ceramic. A more accurate study requires the consideration of the local periodic arrangement of the fibers and the imperfect bonding between fiber and matrix, as a crack moves through the composite.

2.2.3 Crack-Bowing Models

In 1970 Lange [28] observed that a crack front tends to increase its length by bowing between inhomogeneities in a brittle material. Based on these observations, the concept of a crack front possessing line energy is postulated. Lange theorizes that this bowing increases the line energy (fracture surface energy) of the crack and thus causes an increase in the toughness of the material, in a manner similar to Orowan's dislocation bowing model. The increase in fracture energy is found to be inversely proportional to the inclusion spacing. Evans [29] considers this bowing in more detail and allows the crack front to adopt a semi-circular or semi-elliptical crack front between inclusions. The toughening is estimated using a stress analysis of an isolated circular or elliptical crack under a uniform (averaged) stress. For brittle particulate-reinforced brittle materials, Evans' calculations [29] indicate that crack bowing is a major contributor to increased toughness. However, predicted toughness values from this model are reasonably near experimentally observed values only for systems reinforced with small volume fractions of brittle particulates. Evans assumes the obstacles are impenetrable and

suggests that obstacle penetration at higher volume fractions accounts for the experimentally observed maximum in the relationship between toughness and volume fraction of reinforcement, which is not predicted nor can be accounted for by the model.

Green, Nicholson and Embury [30] modify Evans' crack-bowing model [29] to account for penetrable obstacles, obstacle shape and crack interactions. Even with these modifications, however, the model is still largely unsuccessful, i.e., it is only successful in predicting toughness increases for systems reinforced with small volume fractions of brittle particulates.

Recently (1987) Rose [31] introduced a crack-bowing model significantly different from previous models [28-30]. Penetrable obstacles are assumed to toughen the material by inducing closure tractions on the bowed portion of the crack. These closure tractions are modeled as distributed springs acting between the crack faces (from Rose [16]) in the bowing region. The stiffness of the reinforcing springs and the depth of the bow (at the critical breakaway position) are related to penetrability of the obstacles, i.e., more penetrable obstacles are modeled with more compliant reinforcing springs and less bowing depth. Using this model, Rose was largely successful [31] in matching earlier experimental data of Lange and Radford [32] for an alumina/epoxy system. Rose's model also predicts a maximum in the relationship between toughness and volume fraction of obstacles, matching the trends observed in experiments [30,32].

Of the bowing models mentioned above [28-31], Rose's model [31] is the only analysis that accurately predicts toughness values and trends observed in experiment. This suggests that the line energy formulation adopted in the other models [28-30] is too simplistic. Interestingly, the formulation of Rose's

successful bowing model actually reduce it to a small-scale bridging problem, very much like the model presented by Budiansky and Amazigo [15]. Like the BA bridging model [15], Rose's bowing model is based on a fracture mechanics formulation such that it reveals the nature of K_{tip} in a comprehensive manner.

2.2.4 Analytical Summary

It should be recognized that most of the models surveyed above analyze one mechanism, which is assumed decoupled from other mechanisms, of the crack propagation. Neglect of the coupled mechanisms, for example, partially explains why the bowing models based only on the line energy concept [28-30] are generally inaccurate for predictive purposes while Rose's bowing model [31], which considers the accompanying crack bridging, is more successful. Thus, a more accurate fiber-toughening model for predicting composite response should consider all important mechanisms, including the bridging, bowing and interaction toughening effects.

It should be noted, however, that as shown in the idealized sequence depicted in Fig. 1.2, the crack bowing/breakaway necessary for crack propagation actually results from interaction between the crack front and stiffer fibers. This strong interplay between crack-tip/fiber interaction, crack bowing, crack bridging and ultimately, crack propagation, demonstrates the importance of considering the toughening mechanisms as coupled.

3. ANALYSIS OF STEADY-STATE FIBER PULLOUT

As seen in the previous chapters, steady-state crack bridging is a dominant toughening mechanism in fiber-reinforced ceramics. The bridging process, in turn, is controlled by fiber pullout. Thus understanding of the mechanics of fiber pullout is required in any consideration of crack bridging. In the steady-state fiber-bridging models surveyed in Chapter 2, all of the fiber pullout models proposed are based on the hypothesis of an interfacial shear stress that is constant in the sliding region and zero elsewhere. Although this assumption renders a reasonably approximate overall pullout response, the basic underlying pullout mechanisms are not clearly described. In this chapter, the mechanics of fiber pullout in the steady-state region of a bridged crack is investigated in a more complete manner.

For a long bridged crack the crack opening displacement far from the crack tip asymptotically approaches a steady-state equilibrium value $2v_o$, which is the separation when the matrix is completely failed. Thus, the crack opening $2v_o$ results when the net force carried by the bridging fibers balances the remote applied force. Subsequently, in the steady-state fiber bridging region the resulting crack surfaces are parallel and straight (in the smeared-out global/structural scale) such that the pullout forces F on all bridging fibers are identical. Figure 3.1a illustrates a steady-state bridged crack, including the steady-state and crack-tip gradient bridging regions. Figure 3.1b shows a single two-dimensional "unit cell", containing a bridging fiber and the surrounding matrix, from the steady-state region of the crack.

We desire a simple, but accurate general two-dimensional pullout force-relative displacement relationship for modeling the steady-state bridging region of a long bridged crack for use in the analysis of fiber toughening

21

mechanisms presented in Chapter 4. This chapter presents, in order, a finite element simulation of steady-state fiber pullout, two basic two-dimensional elasticity solutions governing the dominant mechanisms of steady-state fiber pullout, and a straightforward application of these elasticity solutions in a mechanics-of-materials approximation of the pullout process.

3.1 FINITE ELEMENT SIMULATION OF STEADY-STATE FIBER PULLOUT

Figures 3.2 and 3.3, which represent one symmetric half of the unit cell of Fig. 3.1, indicate the steady-state fiber pullout problem considered and show a simple finite element model initially used to investigate the fiber pullout. In Fig. 3.2, the fiber/matrix interface, which is along x = 0, is closed but frictionally slipping over some region. The model of Fig. 3.3 contains discrete fiber and matrix portions connected by a frictional interface to simulate this slipping. The fiber and matrix regions consist of standard eight-node isoparimetric continuum elements under a plane strain condition. One-dimensional interface line elements capable of open/closed contact behavior and stick/frictional slip response (when closed) are used to model the fiber/matrix interface. The interface elements are preloaded by a compressive stress $\sigma_i^{(o)}$ such that they are initially closed and sticking. This interface preload condition is described by a nominal interfacial shear stress $\tau_i^{(o)}$ given by

$$\tau_i^{(o)} = -\mu\sigma_i^{(o)} \tag{3.1}$$

where μ is the interface friction coefficient and $\sigma_i^{(o)}$ is the initial interface compression. The boundary conditions shown in Fig. 3.2 result from the periodicity of the fibers and symmetry within the unit cell. These boundary

conditions are shown in Fig. 3.3 at only a few edge nodes for illustration. The ABAQUS[1] finite element program installed on a CONVEX XP-1 computer and a SUN 4-280 workstation was used to perform the fiber pullout analysis.

Figures 3.4a and 3.4b show typical results from the finite element pullout analysis and illustrate the variation of the interfacial shear stress τ_i for the cases $E_f/E_m = 1$ and $E_f/E_m = 16$, respectively. Figure 3.5 idealizes the variation of τ_i as consisting of 3 regions and 2 transition points. Relative fiber-matrix slipping occurs in $0 \leq y \leq L$ (region 1) but not above the sticking point $y = L$ in regions 2 and 3. In region 2 ($L \leq y \leq H$), τ_i decays with y until isostrain holds above $y = H$ in region 3. In the asymptotic regions around $y = 0$ and $y = L$, free edge [33,34] and mode II crack tip singularities [35-39] exist but are not revealed by this simple displacement based finite element method. Note that in Fig. 3.4 and in the idealization of Fig. 3.5 the interfacial shear stress τ_i does not follow the simple constant profile hypothesized in the earlier pullout analyses [12-17].

3.2 ANALYTICAL DESCRIPTION OF STEADY-STATE FIBER PULLOUT

The overall steady-state fiber pullout behavior is dominated by the interfacial shear stress in the slipping and sticking regions such that the small singular regions depicted in Fig. 3.5 can be neglected for simplicity. Then, the progression of τ_i throughout the pullout process can be idealized as shown in Fig. 3.6. Note that in Fig. 3.6 the additional simplification

$$\tau_i = \tau_i^{(o)} \qquad \text{at } y = L \qquad (3.2)$$

is made. As seen in Fig. 3.7, the finite element results for $E_f/E_m = 1$ support

---

[1] Hibbit, Karlsson and Sorensen, Inc., Providence, RI.

23

this simplification, as do the results for $E_f/E_m = 3$ and $E_f/E_m = 16$ where the deviation of τ_i at $y = L$ from the nominal shear stress $\tau_i^{(o)}$ is small. Specifically, Eq. (3.2) should be accurate for the case of a ceramic matrix composite, where typically $E_f/E_m \leq 5$. Also note that the idealization of Fig. 3.6 includes the well known stick/slip behavior, and that τ_i varies in the slipping region and is non-zero in a portion of the sticking region -- realistic aspects missing from the earlier analyses [12-17]. Elasticity solutions governing the simplified variation of τ_i depicted in Fig. 3.6 are presented below. A mechanics-of-materials approximation of the pullout force-relative crack opening displacement relationship, based on the simplified elasticity description of the interfacial shear stress, is also given.

3.2.1 Slipping Region Elasticity Problem Formulation

An approximate equilibrium argument presented in Appendix 1 as well as the finite element results depicted in Figs. 3.4a and 3.4b suggest that τ_i behaves exponentially in the slipping region. We then assume the stresses in the fiber and matrix behave exponential in y and are each given by separable Airy stress functions of the form

$$\Phi_1 = \exp[a(y - L)]f(x), \tag{3.3}$$

where a is a constant controlling the exponential stress behavior in y. Equilibrium and compatibility equations require [40] that Φ_1 satisfy the biharmonic equation

$$\nabla^4 \Phi_1 = 0$$

which yields the general solution for $f(x)$,

$$f(x) = (C_1 + C_2 x)\cos(ax) + (C_3 + C_4 x)\sin(ax), \tag{3.4}$$

24

where the C_i are constants controlling the stress variation in x. The periodicity of $f(x)$ is required owing to the periodic boundary conditions of the unit cell. Note that a controls not only the exponential stress behavior in y, but also the stress variation in x. The stresses and plane strain displacements are determined as

$$\sigma_{xx} = a^2 \exp[a(y - L)]\{[C_3 + C_4 x]\sin(ax) + [C_1 + C_2 x]\cos(ax)\} \qquad (3.5)$$

$$\sigma_{yy} = a\exp[a(y - L)]\{[-2C_2 - C_3 a - C_4 ax]\sin(ax) + [2C_4 - C_1 a - C_2 ax]\cos(ax)\}$$

$$\sigma_{xy} = a\exp[a(y - L)]\{[C_4 - C_1 a - C_2 ax]\sin(ax) + [C_2 + C_3 a + C_4 ax]\cos(ax)\}$$

and

$$u_x = [(1 + \nu)/E]\exp[a(y - L)]\{[(1 - 2\nu)C_4 + C_1 a + C_2 ax]\sin(ax) +$$
$$[(1 - 2\nu)C_2 - C_3 a - C_4 ax]\cos(ax)\}$$

$$u_y = [(1 + \nu)/E]\exp[a(y - L)]\{[2(1 - \nu)C_2 + C_3 a + C_4 ax]\sin(ax) +$$
$$[2(1 - \nu)C_4 + C_1 a + C_2 ax]\cos(ax)\}. \qquad (3.6)$$

In this manner stress functions for the fiber and matrix yield 10 unknowns: a_f and C_1 through C_4 for the fiber and, similarly, a_m and D_1 through D_4 for the matrix. The boundary conditions at the fiber and matrix edges of the half cell of Fig. 3.2 are

$$\sigma_{xy}^{(f)} = 0 \qquad \text{at } x = x_f$$
$$\sigma_{xy}^{(m)} = 0 \qquad \text{at } x = x_m \qquad (3.7a)$$

and

$$u_x^{(f)} = 0 \qquad \text{at } x = x_f$$
$$u_x^{(m)} = 0 \qquad \text{at } x = x_m \qquad (3.7b)$$

25

which arise from symmetry considerations as mentioned above. The constant displacements u_x at the fiber and matrix edges are zero since $u_x \longrightarrow 0$ for large y. Continuity across the interface requires

$$\sigma_{xx}^{(f)} = \sigma_{xx}^{(m)}$$
$$\sigma_{xy}^{(f)} = \sigma_{xy}^{(m)} \qquad \text{at } x = 0 \qquad (3.8)$$
$$u_x^{(f)} = u_x^{(m)}$$

while for a frictional slip problem,

$$\sigma_{xy} = \mu\sigma_{xx} \qquad \text{at } x = 0 \qquad (3.9)$$

where μ is the friction coefficient. The shear and normal stresses in Eq. (3.9) have the same sign because σ_{xx} is compressive at the interface and σ_{xy} is negative for the fiber to pull out. Additionally, for the conditions in Eq. (3.8) to be independent of y,

$$\alpha_f = \alpha_m \qquad (3.10)$$

must also hold. Finally, we specify the magnitude of the stress by

$$\sigma_{xy}(0,L) = -\tau_i^{(o)} \qquad (3.11)$$

where the sign on $\tau_i^{(o)}$ is negative so that the fiber pulls out. This equation results from the simplification made in Eq. (3.2). Equation (3.11) and Eq. (3.9) also specify the compressive residual normal stress at the interface, e.g., Eq. (3.1). Then, the conditions (3.7) through (3.11) supply 10 equations for the 10 unknowns.

Solving for the 10 unknowns then yields the stresses, strains and displacements in the fiber and matrix, as well as the exponential constants α.

26

Only the homogeneous case where the fiber and matrix have the same properties can be easily solved by hand. Inhomogeneous cases can be solved numerically in a straightforward manner.

3.2.2 Sticking Region Elasticity Problem Formulation

Related shear lag solutions [42,43] and finite element results [43,44], as well as the current finite element results depicted in Fig. 3.4, indicate that τ_i decays exponentially in the sticking region. Thus, we again begin with Airy stress functions of the form

$$\Phi_2 = \exp[-\gamma(y - L)]g(x) \tag{3.12}$$

and find that $g(x)$ is identical to that of $f(x)$ in Eq. (3.4), except for the change in constant from a to γ. Subsequently, stresses and displacements are then similar to Eqs. (3.5) and (3.6). Additionally, the boundary and continuity conditions are identical except the additional interface continuity condition

$$u_y^{(f)} = u_y^{(m)} \qquad\qquad \text{at } x = 0 \tag{3.13}$$

replaces the frictional slip condition (3.9), decoupling the interfacial normal and shear stresses. The resulting system of 10 equations and 10 unknowns is again easily solved numerically.

3.2.3 Relationship Between the Pullout Force and Crack Opening Displacement

To derive a simple pullout force-relative displacement relation the pullout process and interfacial shear stress are idealized as shown in Fig. 3.6. Figure 3.8 shows a free body diagram of the half cell where v_o is the relative fiber pullout displacement, δ is the average matrix extension and $\tau_i^{(o)}$ is the magnitude of the interfacial shear stress at the sticking point and is given by Eq. (3.1). In the slipping configuration the stresses in the fiber and matrix

27

are

$$\sigma_m A_m = 0$$
$$\sigma_f A_f = F$$
$$\text{at } y = 0 \qquad\qquad (3.14)$$

where A_m and A_f are the area of the fiber and matrix per unit cell and F is the pullout force on the fiber. Similarly, in the slipping region, $0 \leq y \leq L$,

$$\tau_i(y) = \exp[a(y - L)]$$
$$\sigma_m A_m = \{2\tau_i^{(o)}/a\}\{\exp[aL] - \exp[a(L - y)]\} \qquad (3.15a)$$
$$\sigma_f A_f = F - \{2\tau_i^{(o)}/a\}\{\exp[aL] - \exp[a(L - y)]\},$$

and in the sticking region, $L \leq y \leq H$,

$$\tau_i(y) = \exp[-\gamma(y - L)]$$
$$\sigma_m A_m = \{2\tau_i^{(o)}/a\}\{\exp[aL] - 1\} + \{2\tau_i^{(o)}/\gamma\}\{1 - \exp[a(L - y)]\} \quad (3.15b)$$
$$\sigma_f A_f = F - \{2\tau_i^{(o)}/a\}\{\exp[aL] - 1\} - \{2\tau_i^{(o)}/\gamma\}\{1 - \exp[a(L - y)]\},$$

and in the isostrain region, $y \geq H$,

$$\tau_i(y) \approx 0$$
$$\sigma_m^{(o)} A_m = \{2\tau_i^{(o)}/a\}\{\exp[aL] - 1\} + \{2\tau_i^{(o)}/\gamma\} \qquad (3.15c)$$
$$\sigma_f^{(o)} A_f = F - \{2\tau_i^{(o)}/a\}\{\exp[aL] - 1\} - \{2\tau_i^{(o)}/\gamma\},$$

where $\sigma_m^{(o)}$ and $\sigma_f^{(o)}$ are the remote fiber and matrix stresses satisfying the isostrain condition $\sigma_m^{(o)}/E_m = \sigma_f^{(o)}/E_m$ and H is large enough that $\exp[L\gamma - H\gamma] \approx 0$. From the stresses, the displacements at $y = 0$ are (for a large H),

$$\delta\{(A_m E_m)/(2\tau_i^{(o)})\} = (1/\gamma)(H - L - 1/\gamma) - (1/a)(1/a - H)(\exp[aL] - 1)$$
$$\{v_o + \delta\}\{(A_f E_f)/(2\tau_i^{(o)})\} = (FH)/(2\tau_i^{(o)}) - (1/\gamma)(H - L - 1/\gamma) + \qquad (3.16)$$
$$(1/a)(1/a - H)(\exp[aL] - 1)$$

so that the relative fiber pullout is

$$v_o A_f E_f = FH - 2\tau_i^{(o)}\beta\{(1/\gamma)(H - L - 1/\gamma) + (1/a)(1/a - H)(\exp[aL] - 1)\} \quad (3.17)$$

where

$$\beta = 1 + E_f A_f / E_m A_m.$$

Now, at $y = H$, the isostrain condition and Eq. (3.15c) yield the pullout force

$$F = 2\tau_i^{(o)}\beta\{(1/\gamma) + (1/a)(\exp[aL] - 1)\} \quad (3.18)$$

in terms of L or

$$L = (1/a)\log[(aF)/(2\tau_i^{(o)}\beta) - (a/\gamma) + 1]. \quad (3.19)$$

Now, using (3.18) in (3.17) yields

$$v_o = \{(2\tau_i^{(o)}\beta)/(\gamma A_f E_f)\}\{L + 1/\gamma\} +$$
$$\{(2\tau_i^{(o)}\beta)/(a A_f E_f)\}\{(1/a)(\exp[aL] - 1) - L\} \quad (3.20)$$

so that Eqs. (3.19) and (3.20) yield the slipping pullout force-relative displacement relation parameterized by the slip length L. Additionally, Eq. (3.18) yields

$$\sigma_c/\tau_i^{(o)} = 2\beta/\gamma + (2\beta/a)(\exp[aL] - 1) \quad (3.21)$$

as a nondimensional measure of the smeared-out (isostrain) composite stress defined as

$$\sigma_c = FV_f/A_f. \quad (3.22)$$

Sliding, however, does not occur if the magnitude of the maximum

29

interfacial shear stress τ_i is less than $\tau_i^{(o)}$. In this case $L = 0$ and the sticking pullout force-relative displacement relation

$$F = E_f A_f v_o \gamma \qquad (3.23)$$

applies when $|max(\tau_i)| \le \tau_i^{(o)}$. The critical average composite stress to cause slipping is then   .

$$\sigma_c^{(c)} = 2\tau_i^{(o)} V_f \beta / (A_f \gamma). \qquad (3.24)$$

Thus when $\sigma_c \le \sigma_c^{(c)}$ the pullout force-relative crack opening displacement $(F - v_o)$ relationship is linear (Eq. (3.23)) but once slipping starts and $\sigma_c > \sigma_c^{(c)}$ the relation becomes nonlinear (Eqs. (3.19) and (3.20)).

3.3 NUMERICAL RESULTS AND DISCUSSION

Substitution of the stresses and displacements of Eqs. (3.5) and (3.6) into the slipping and sticking boundary and interface conditions yields a system of ten equations for each problem. Careful algebraic manipulation of only a few of the resulting equations yields a single transcendental equation each for the constants a and γ. The values of a and γ which satisfy these equations are found numerically.

3.3.1 Slipping Region

The numerical solutions in the slipping region reveal that a is independent of $\tau_i^{(o)}$ and depends only on the ratio E_f / E_m, not only the actual stiffnesses of the fiber and matrix. Additionally a depends on the fiber and matrix Poisson's ratios ν_f and ν_m, the friction coefficient μ and the width of the unit cell. The constant a can be normalized, however, with respect to μ and the unit cell width $(x_f - x_m)$.

30

Figures 3.9a through 3.9c illustrate the dependence of a on fiber volume fraction, the ratio E_f/E_m and ν when $\nu_f = \nu_m$. Figure 3.10 shows the variation of a with volume fraction when $E_f/E_m = 3$ and $E_f/E_m = 1/3$ and indicates the inversion symmetry of these results about $a = 0$ and $V_f = 50\%$. The effect of different Poisson's ratios on a when $E_f/E_m = 1$ is shown in Fig. 3.11. Note the inversion symmetry also evident in Fig. 3.11.

Figure 3.12 clearly summarizes the dependence of a on material properties for $V_f = 33\%$. For the special case $\nu_f = \nu_m$, a is positive, zero, or negative, and correspondingly, from Eq. (3.5), τ_i in the slipping region either increases exponentially, remains constant, or decrease exponentially when E_f/E_m is less than, equal to, or greater than unity, respectively. Recall, however, τ_i is always equal to $\tau_i^{(o)}$ at the sticking point $y = L$. Then, when a is positive $(E_f > E_m, \nu_f \leq \nu_m)$, τ_i is greater than $\tau_i^{(o)}$ in the slipping region, and, due to the frictional coupling between interfacial shear and normal stresses (expressed in Eq. (3.9)), the interface compression in the slipping region is greater than the initial compressive preload $\sigma_i^{(o)}$. Or, simply, when $E_f > E_m$ and $\nu_f \leq \nu_m$, the compression at the slipping interface <u>increases</u> (relative to $\sigma_i^{(o)}$) during fiber pullout. Similarly, the slipping interface compression either decreases or remains constant during fiber pullout for E_f/E_m less than or equal to unity, respectively (when $\nu_f = \nu_m$). Therefore, Fig. 3.12 also describes the tendency of the slipping interface to open (debond) during pullout depending upon whether a is positive or negative -- for a typical composite where $E_f > E_m$ and $\nu_f \leq \nu_m$, a is positive and the slipping interface remains closed.

Figure 3.13 compares finite element predictions for a with the analytical solution derived above. In all Figs. 3.13a through 3.13c agreement is good

31

except at high and low fiber volume fractions, where the finite element mesh becomes excessively distorted. This distortion is caused by excessive element aspect ratios in the small volume fraction region (i.e., fiber region for small V_f, matrix region for large V_f) and is caused by the current simple mesh definition. The good correlation illustrated in Fig. 3.13 indicates that the finite element analysis accurately models the pullout for reasonable volume fractions.

The stresses and displacement given by Eqs. (3.5) and (3.6) when E_f/E_m = 3, $\nu_f = \nu_m = 0.25$ and $V_f = 33\%$ are shown in Figs. 3.14a through 3.14b. At this relatively low stiffness ratio E_f/E_m, a is small. Subsequently, from Eq. (3.5) the change of τ_i along the slipping interface is small and variation in x of all stresses and strains is nearly linear. Additionally σ_{yy} and u_y are discontinuous across the interface, as expected. Note that the stresses and strains of Fig. 3.14, however, are only representative of the above solution; the complete pullout solution for the slipping region is obtained by adding various constant isostrain stress states to the obtained solution.

3.3.2 Sticking Region

Because in the sticking region the shear and normal stresses at the interface uncouple (Eq. (3.13)), the decay exponent γ depends only on the relative difference $(\nu_f - \nu_m)$ and not on the actual values ν_f and ν_m. Note that γ can be normalized with respect to geometry; additionally, γ is independent of $\tau_i^{(o)}$ and the friction coefficient μ, as expected.

Figure 3.15 illustrates the dependence of γ on volume fraction and E_f/E_m when $\nu_f = \nu_m$. When $E_f/E_m = 1$ and $\nu_f = \nu_m$, the normalized $\gamma = \pi$. Note that γ becomes large for E_f/E_m large and V_f large. Figure 3.16 shows the variation of γ with volume fraction when $E_f/E_m = 3$ and $E_f/E_m = 1/3$ and indicates the

symmetry of these results about V_f = 50%. The effect of the difference $(v_f - v_m)$ when E_f/E_m = 1 is shown in Fig. 3.17. Again note the symmetry exhibited in Fig. 3.17. Figure 3.18 summarizes the dependence of γ on material properties when V_f = 33%. Note that in Fig. 3.18, $\gamma > 0$, indicating that τ_i always decays above the sticking point, i.e., isostrain is always obtained for large y.

Figure 3.19 compares the finite element prediction for γ with the analytical solution. In Figs. 3.19a - 3.19c agreement is good except at high and low volume fractions, indicating the ability of the finite element model to simulate pullout at reasonable volume fractions.

Stresses and displacements in the sticking region when E_f/E_m = 3, $v_f = v_m$ = 0.25 and V_f = 33% are shown in Figs. 3.20a - 3.20c. Only σ_{yy} is discontinuous across the interface, as expected. Comparing Fig. 3.20 to Fig. 3.14 reveals the effect of a higher exponential constant (normalized γ = 1.92 vs. normalized α = 0.29) in Eqs. (3.5) and (3.6); stresses and displacements vary in a more harmonic manner in x when the exponent is higher. Again, this oscillatory behavior in x is given by Eq. (3.4). Additionally, as with the slipping solution, the complete pullout solution in the sticking region is obtained by adding constant isostrain stress states to the solution presented.

3.3.3 Steady-State Fiber Pullout Response

The steady-state fiber pullout force-relative displacement relation derived in §3.2.3 and the interfacial shear stress variation determined in §3.2.1 and §3.2.2 are used in conjunction to predict the fiber pullout response. Figure 3.21 illustrates the predicted fiber pullout response and how it varies with material properties and friction coefficient μ. In Fig. 3.21a the linear sticking response given by Eq. (3.23) can be seen for E_f/E_m = 16 and $\sigma_c/\tau_i^{(o)}$

33

≤ 5.9. Figure 3.21b illustrates the changes in friction coefficient have small effect on the pullout response. Note that in all of these figures the composite stress σ_c is normalized by $\tau_i^{(o)}$. This nondimensionalization is made possible by the assumption of Eq. (3.2) that τ_i is always equal to $\tau_i^{(o)}$ at the sticking point.

Previous pullout models [12-17] have assumed an interfacial shear stress that is constant in the slipping region and zero elsewhere. These models do not predict stick/slip behavior nor do they provide any analytical basis for the assumed τ_i. In Fig. 3.22, the predictions from the constant τ_i model are compared with both the model derived above and the finite element results. The correlation between finite element results and current predictions are good, indicating the accuracy of the mechanics-of-materials approach used in deriving the pullout force-relative displacement relation. The earlier constant τ_i model is reasonably accurate in an average sense, but it does not predict the realistic detailed stick/slip behavior.

Figure 3.23 shows a much coarser mesh used to model the pullout and Fig. 3.24 compares the predictions from this coarse model and the fine model depicted in Fig. 3.3. Note that the coarse model is still able to accurately predict the overall pullout response. These observations lend confidence in the ability of the finite element method to represent the overall pullout behavior. The coarse model, however, does not accurately reveal the variation of τ_i.

3.3.4 Additional Remarks

The above sticking and slipping region solutions are sufficient to derive an approximate pullout force-relative displacement relation. The asymptotic singular solutions at the sticking point and at the free edge are necessary,

however, to completely describe the pullout. Specifically, the asymptotic solution at $y = 0$ is needed to satisfy the boundary conditions there and the asymptotic solution at $y = L$ will allow connection between the different solutions in the slipping and sticking region.

Additionally, the asymptotic solution and the matching conditions at the sticking point should reveal $\tau_i^{(o)}$. Realistically, $\tau_i^{(o)}$ should vary with L. In the numerical calculations made here and in Chapter 4, however, the simplification of Eq. (3.1), i.e., $\tau_i^{(o)} = -\mu\sigma_i^{(o)}$, where $\sigma_i^{(o)}$ is the applied residual compression at the interface (from thermal cooling) is used. The finite element results of Fig. 3.7 and Fig. 3.21 indicate that this is a reasonably accurate simplification for a ceramic fiber reinforced ceramic matrix composite, where E_f/E_m is typically less than 5.

4. COMPOSITE TOUGHENING

The toughening models and fracture mechanics solutions reviewed in Chapter 2 address various aspects of the many toughening mechanisms of fiber-reinforced ceramic composites. To solve the complex problems considered, however, all of the analyses need to include simplifying assumptions -- some of which eliminate important realistic aspects of the composite toughening. For example, the bimaterial fracture mechanics solutions do not represent the periodic fibers in a composite, and the steady-state fiber-bridging models do not consider the fiber/matrix inhomogeneity at the crack tip. Additionally, the bridging models employ very simplified steady-state fiber pullout behavior to represent the bridging fibers along the entire crack face, including the high-gradient crack-tip region.

This chapter presents a finite element analysis employed to more accurately model some of the complex toughening phenomena involved in fiber-reinforced ceramic composites. The present two-dimensional plane strain finite element toughening analysis utilizes the fiber pullout mechanics results derived in Chapter 3 to accurately represent pullout in the steady-state region of the bridged crack and includes discrete fiber and matrix segments near the crack tip to directly model pullout and crack-tip/fiber interactions in the high-gradient crack-tip regions. In order to investigate both crack bridging and crack-tip/fiber interaction toughening mechanisms, the finite element model simulates both fully bridged and fully unbridged crack configurations. The finite element model generation and analysis were performed using the ABAQUS program run on a CONVEX XP-1 computer and SUN 4-280 workstation.

4.1 ANALYTICAL METHOD

The two-dimensional finite element model represents a cracked unidirectional fiber composite plate, with the crack perpendicular to the fibers, as shown in Fig. 4.1. The finite element model of the plate is composed of three primary regions, also illustrated in Fig. 4.1: the remote region at the structural scale, a local region at the discrete micromechanics scale (i.e., the fiber-matrix scale) and a singular region at the scale of the asymptotic crack tip singular field. The relative sizes of the three regions are approximately determined by several factors: the size of the plate relative to the crack length, the approximate size of the K-controlled domain (when the crack is unbridged) relative to the fiber size, and the size of the crack-tip gradient region (when the crack is bridged) relative to the fiber size. The steady-state bridging behavior derived in Chapter 3 is used to model bridging in the global region while the micromechanics region models the bridging directly using frictional interface elements. The fiber volume fraction V_f is 1/3. The entire model is strictly two-dimensional in that three-dimensional fiber packing array dependent effects are not considered. For example, mechanical composite properties are calculated based on simple one-dimensional derivations and residual compression at the interface is implemented in a manner that ignores the three-dimension residual stress field that exists in a real composite. Consistency within the model requires these simplifications.

4.1.1 Finite Element Model — Global Region

Symmetry within a cracked plate allows consideration of one-quarter of the plate. Figure 4.2 shows the global finite element mesh, which models the steady-state region of the bridged crack and represents the majority of the quarter-plate. The crack tip is at the origin $x = y = 0$ and the crack face

37

lies along $y = 0$, $x < 0$. The size of the global mesh is determined by two factors. First, the half crack length a_o is determined such that the size of the K-controlled domain, given roughly by $a_o/20$, is approximately equal to the center-to-center fiber spacing d_o, in order that the local crack-tip/fiber interaction can be observed. Second, the plate size satisfies $a_o/W = 10$, where the total crack length is $2a_o$ and the total plate width is $2W$, so that finite width effects are negligible. The global mesh consists entirely of eight-node and six-node isoparimetric elements. The vacant rectangle around the crack tip in Fig. 4.2 is actually filled by the micromechanics and singular region meshes, as idealized in Fig. 4.1. Boundary conditions on the global mesh are standard symmetry constraints (constant normal displacement) on the sides and bottom (excepting the crack face) and applied stress σ_c along the top of the plate. The displacement boundary conditions are indicated in Fig. 4.2 at only a few nodes for brevity. Orthotropic material properties in the homogeneous global region are calculated from the isotropic fiber ($V_f = 1/3$) and matrix properties using simple one-dimensional rule of mixtures formulas and the Halpin-Tsai equations for transverse properties [45].

Bridging elements reinforce the crack face in the global region. These bridging elements are given appropriate linear/nonlinear effective material properties described by Eq. (3.23) (sticking pullout relation) and Eqs. (3.19 – 3.20) (slipping pullout relation) and are implemented in such a manner that they exhibit the correct steady-state pullout force-relative displacement behavior derived in Chapter 3. Thus, the crack face in the global region "appears" to the crack tip as steady-state bridged. However, the bridging elements can be given small (zero) stiffness, if desired, to model a crack which is unbridged in the global region.

38

4.1.2 Finite Element Model — Micromechanics Region

Figure 4.3 shows the finite element mesh in the discrete micromechanics region around the crack tip. This extensive mesh directly models the fiber pullout and crack-tip/fiber interaction in the high-gradient crack-tip region. In the model, $d_m = 2d_f$, where d_m is the matrix region width and d_f is the fiber width (indicated in Fig. 4.3) such that the fiber volume fraction V_f is 1/3. Additionally, note that $d_o = d_m + d_f$, where d_o is the center-to-center fiber spacing. The crack tip is at the origin $x = y = 0$ and the cracked region is along $y = 0$ for $x < 0$. Following the results of the steady-state crack-bridging models [12-17] reviewed in §2.2.1, the discrete micromechanics mesh extends approximately $10d_f$ on each side of the crack tip in order that it contains the high-gradient crack-tip region of the bridged crack. The mesh of Fig. 4.3 fills the vacant portion of the global mesh depicted in Fig. 4.2. A singular region mesh in turn occupies the empty rectangle of the discrete mesh and defines the exact position of the crack tip. Eight-node and six-node isoparimetric elements are used to define the discrete fiber and matrix · regions. The two-dimensional fiber and matrix elements that have edges on the fiber/matrix interface are connected together by one-dimensional interface elements. These line elements are capable of open/closed contact behavior and stick/Coulombic frictional slip response (when closed), thus allowing relative sliding between the fiber and matrix. The interface edges of the fiber and matrix elements are loaded by identical negative pressures to compress the interface. The applied interface compressive preload, $\sigma_i^{(o)}$, and the friction coefficient μ are related to the nominal interfacial shear stress $\tau_i^{(o)}$ by Eq. (3.1) of Chapter 3. This loading technique produces a line of compression along the interface (necessary for Coulombic friction) without introducing any

39

residual stresses in the fiber and matrix. In this manner the crack tip stress field and the toughening effects can be observed without the complications introduced by residual stress fields. Displacement boundary conditions shown at a few nodes (for brevity) along the bottom of the discrete region of Fig. 4.3 apply at every bottom edge node in the uncracked $(x > 0)$ side and at the bridging fiber bottoms in the cracked $(x < 0)$ side of the mesh. The bottom nodes of the fiber elements in the cracked side of the discrete mesh can be released, if desired, to model a crack which is unbridged in the discrete region.

The many fiber/matrix regions require a consistent terminology to describe locations and phenomena within the micromechanics mesh. In this analysis, "downstream" and "upstream" refer to the cracked $(x < 0)$ and uncracked $(x > 0)$ sides of the crack tip, respectively. The fiber immediately ahead of the crack tip is the "upstream fiber" or "first upstream fiber", and the fiber immediately behind the crack tip is the "downstream fiber" or "first downstream fiber". The next upstream fiber is the "second upstream fiber", etc. The "cracked matrix region" is bounded by the first upstream and downstream fibers, and the "upstream matrix region" or the "first upstream matrix region" is bounded by the first and second upstream fibers. Similarly, the "downstream matrix region" or "first downstream matrix region" is bounded by the first and second downstream fibers. This terminology will be used in later sections to describe the locations of fiber slipping, stresses, etc.

4.1.3 Finite Element Model — Singular Region

Figure 4.4a shows a typical singular region mesh that surrounds the crack tip at $x = y = 0$ and resides in the empty rectangle of the cracked matrix region of the micromechanics mesh of Fig. 4.3. The crack face lies

along y = 0 for x < 0. The size of the singular mesh roughly equals the size of the K-controlled domain, given approximately by $a_o/20$ when the crack is unbridged, i.e, the size of the K-field is on the order of the fiber spacing. In the mesh of Fig. 4.4a, the crack tip is halfway between the two bounding fibers. If d_m is the distance between the upstream and downstream inner fiber edges (in this model the width of the singular mesh) and d_{tip} is the distance from the crack tip to the downstream fiber inner edge, the mesh of Fig. 4.4a has d_{tip}/d_m = 50%. In this manner other meshes with different values of d_{tip}/d_m can be used to investigate the effect of crack-tip position. Specifically, Figs 4.4b through 4.4e illustrate other singular meshes used in the analysis which include d_{tip}/d_m values of 16.7%, 33.3%, 66.7% and 83.3%, respectively. Note the origin lies at the crack tip in all meshes. Displacement boundary conditions are also indicated in Figs. 4.4a through 4.4e at a few of the bottom nodes (for brevity) in the uncracked (x > 0) side of the mesh. All of the singular meshes of Fig. 4.4 are based on eight-node isoparimetric elements arranged so that the "quarter-point" crack tip elements exhibit the $1/\sqrt{r}$ stress singularity [46,47]. The surrounding elements are sized appropriately to imply a singularity at the crack tip.

4.1.4 Toughening Characterization

In order to determine K_{tip} when the cracked composite plate is loaded, J-integral [48] evaluations, using the virtual crack extension method [49,50], are performed along six different concentric paths around the crack tip in the singular mesh. Within the singular region mesh the crack face is traction free and infinitesimal crack growth is self-similar such that, according to theory [48,51,52], the J-integral should be path independent within this regular region. In the model, the numerically determined values of J differ only

slightly depending upon the evaluation path (typically less than a few percent), thus obeying theory within good numerical precision. The recorded value of J is J_{avg}, the average of the six crack-tip J-integrals. Additionally, the crack-tip J-integral (within the singular region) and the crack-growth energy-release rate, G, are equivalent, due to the path independence of J within the singular region mesh. Then, the stress intensity factor at the crack tip in the matrix is determined from the plane strain relation

$$G = J_{avg} = (1 - \nu_m^2)K^2_{tip}/E_m \qquad (4.1)$$

where E_m and ν_m are the matrix modulus and Poisson's ratio, respectively.

As discussed in §2.2.1, the bridging model section of Chapter 2, the crack-tip stress intensity factor K_{tip} of a steady-state bridged crack is independent of the total crack length. This crack-length independence is a result of the force equilibrium in the steady-state bridging region, depicted in Fig. 3.8 of Chapter 3, i.e., the remote applied load is balanced entirely by the fiber load in the steady-state region of a long bridged crack. Effectively, then, the steady-state bridging region of the crack does not induce any crack tip loading. Rather, the K_{tip} is induced by the local, high-gradient (i.e., non-steady-state) region of the crack near the crack tip. The size of the controlling, gradient region is a function of the fiber size, not the total crack length, as shown in the steady-state bridging models [12-17] of §2.2.1. Therefore, it follows that when a crack is steady-state bridged, an appropriate description of toughening should be independent of the total crack length but related to the fiber size. In the analysis, the toughening in the bridged model is described by the steady-state bridged toughening parameter β_{ss}, given by

$$\beta_{ss} = K_{tip}/K_f, \tag{4.2}$$

where K_{tip} is the actual crack-tip stress intensity factor of Eq. (4.1). The reference stress intensity factor, K_f, is appropriately related to the fiber size and is given by

$$K_f = \sigma_c \sqrt{(\pi d_f)}, \tag{4.3}$$

where d_f is the fiber width and σ_c is the remote applied composite stress. Subsequently, the toughening parameter β_{ss} for a steady-state bridged crack is independent of the total crack length and related to the fiber size, as desired.

In an unbridged, cracked fiber composite, however, the crack-tip stress intensity factor K_{tip} is induced by the entire crack length. In this case, an appropriate toughening description should consider the total crack length. Additionally, the toughening should depend, in some complex manner, upon the relative scales of the total crack length (which determines the size of the K-controlled domain) and the fiber size. This second effect can, in this analysis, be neglected since the model has been specifically sized to generate a micromechanics (i.e., fiber-size) K-field. Thus, the unbridged toughening parameter β_{ub} is given by

$$\beta_{ub} = K_{tip}/K_o, \tag{4.4}$$

where again K_{tip} is the actual crack-tip stress intensity factor. The reference stress intensity factor is now appropriately related to the total crack length a_o by

$$K_o = \sigma_c \sqrt{(\pi a_o)}, \tag{4.5}$$

43

where σ_c is the remote applied composite stress. Thus, the unbridged toughening parameter β_{ub} is related to the total crack length, as desired.

4.1.5 Stresses Related to Crack Propagation

The complex mechanisms involved in crack propagation, particularly in a fiber-reinforced composite, generally cannot be fully described by one or two stresses. A conceptual understanding of the propagation process, however, may be aided by investigation of a few characteristic stresses. Specifically, in this investigation, crack propagation in the bridged composite is known to be controlled by successive matrix region fracture and interface slipping/debonding. Of particular concern to the crack propagation is the tendency of the upstream fiber to slip/debond, and the upstream matrix to fracture. Characteristic stresses related to these phenomena are here denoted as $\sigma_i^{(u)}$ and $\sigma_m^{(u)}$, for upstream interface and matrix stresses, respectively. Figure 4.5 indicates specifically where these stresses are determined in the toughening analyses. As shown in Fig. 4.5, $\sigma_i^{(u)}$ is the interface normal stress on the inner side (downstream side) of the upstream fiber and $\sigma_m^{(u)}$ is the principle stress in the upstream matrix region (on the upstream side of the upstream fiber). The matrix stress $\sigma_m^{(u)}$ is always the highest principle stress at its location and is oriented parallel to the fibers (as shown) for the crack configuration and loading considered in this analysis. The upstream interface normal stress, $\sigma_i^{(u)}$, is non-dimensionalized by the initial interface compressive preload, $\sigma_i^{(o)}$, such that if the ratio $\sigma_i^{(u)}/\sigma_i^{(o)}$ decreases during loading then the interface tends to slip/debond. Similarly the non-dimensional ratio $\sigma_m^{(u)}/\sigma_m^{(o)}$ reveals the stress concentration in the upstream matrix region, relative to the far-field (isostrain) matrix stress $\sigma_m^{(o)}$, and thus describes the tendency of the upstream matrix region to fracture. In combination, then, the

stress ratios $\sigma_i^{(u)}/\sigma_i^{(o)}$ and $\sigma_m^{(u)}/\sigma_m^{(o)}$ characterize the crack propagation. For example, for a bridged crack to propagate it may be required that $\sigma_i^{(u)}/\sigma_i^{(o)}$ be small (so the fiber can pullout) and $\sigma_m^{(u)}/\sigma_m^{(o)}$ be large (so the upstream matrix region can fracture).

4.1.6 Model Verification

Manipulation of material properties, boundary conditions and loadings in the fiber toughening modeling (Figs. 4.2 through 4.4) can yield various simple test cases to verify and check the accuracy of the model. For the toughening problems considered here, primarily the model must be able to accurately reveal K_{tip} under remote and crack face loading, including the effects of local material heterogeneity. In Table 4.1 the results of several test cases are summarized and the finite element predictions are compared with available analytical solutions. External loading refers to the standard configuration of a remote tensile nominal stress σ_c applied to the top boundary of the plate. Internal loading is accomplished by applying either an opening pressure $(-\sigma_c)$ or a point load P to the crack face. The edge cracked plate is modeled by removing the symmetry conditions along the left edge of the model. The bimaterial plate configuration is obtained by retaining the symmetry conditions and suitably defining element material properties such that the model represents a crack of length $2a_o$ lying symmetrically between and normal to two bounding bimaterial interfaces a distance of 2D apart (i.e., a cracked ply in a laminate). Agreement between the model and analytical solutions is good for all tests cases, indicating the ability of the model to accurately represent the crack-tip stress intensity factor K_{tip}.

Additionally, the finite element model must accurately represent the steady-state bridged behavior of the crack. Recall that the crack bridging is

45

modeled directly in the discrete micromechanics mesh and indirectly, using the results of Chapter 3, in the steady-state (global) region. Since crack bridging is modeled as a steady-state pullout in the global mesh region, the extent of the crack-tip gradient region should be within the discretely modeled region (i.e. within the micromechanics mesh). Also, the crack opening displacements in the two regions should join consistently across the global/discrete boundary. Recall, from Chapter 3, the steady-state fiber pullout response consists of linear (sticking) and nonlinear (sliding) load-displacement behavior. Figure 4.6 shows typical crack face profiles for a linear (no-slip) case when $\sigma_c/\tau_i^{(o)} = 0.5$ for both $E_f/E_m = 1$ and $E_f/E_m = 4$. Similarly, Fig. 4.7 shows typical crack profiles during nonlinear, large slip/pullout behavior when $\sigma_c/\tau_i^{(o)} = 10.0$ for both $E_f/E_m = 1$ and $E_f/E_m = 4$. The crack tip is at $x/d_f = 0$ and the micromechanics (i.e., discrete fiber/matrix) region extends to approximately $10d_f$ downstream from the crack tip in Figs. 4.6 and 4.7. In Figs. 4.6 and 4.7 the crack opening displacement appears excessive due to the vertical axis scaling, which has been expanded to clearly illustrate the global/local transition region. Note that the matrix crack opening displacement at the fiber/matrix interface is zero in the sticking cases and non-zero in the slipping cases. In all of these figures the transition of crack opening displacement between global and local discrete meshes is consistent and the crack opening displacement approaches the steady-state value v_o quickly within the discrete micromechanics region. These observations indicate both the appropriate extent of the discrete micromechanics mesh and the proper transition between the smeared-out steady-state global region and the directly modeled discrete region. These results, combined with the test case results above, lend confidence in the

ability of the current model and analysis to accurately represent the bridging and fiber/crack-tip interaction of toughening mechanisms under investigation here.

4.2 NUMERICAL RESULTS AND DISCUSSION

The toughening analyses performed with the above described finite element model include two configurations: unidirectional ceramic composite plates with an unbridged and a bridged crack. The unbridged model reveals the inhomogeneity (or crack-tip/fiber interaction) toughening effects only and is achieved by removing certain boundary conditions, as described in §4.1.1 and §4.1.2. The bridged model includes the fiber bridging mechanisms. The unbridged model is perfectly bonded and all constituents are linear-elastic so that the toughening is load independent. The toughening in the unbridged model, which includes linear/nonlinear fiber pullout response, conversely, is strongly load dependent. However, under low loads when the bridging fibers are sticking (i.e., linear fiber-pullout response) toughening in the bridged model is also independent of load.

In the next sections the toughening effects of various composite parameters, as well as the remote applied stress σ_c level, are investigated for both the bridged and unbridged models. The material and microstructural parameters include the stiffness ratio E_f/E_m, crack tip position d_{tip}/d_m and friction coefficient μ. The toughening is characterized by the parameters β_{ss} and β_{ub}, as described in §4.1.4, and stresses relevant to crack propagation are described by the ratios $\sigma_m^{(u)}/\sigma_m^{(o)}$ and $\sigma_i^{(u)}/\sigma_i^{(o)}$, as presented in §4.1.5.

4.2.1 Unbridged Model

In the unbridged analyses, the composite toughening is solely due to

47

the crack-tip/fiber interactions. Additionally, the toughening is load independent since the fiber and matrix are perfectly bonded (i.e., nonlinear fiber/matrix sliding cannot occur) and linear-elastic. The toughening results are presented in terms of the toughening parameter β_{ub}, as described in §4.1.4. Recall that $\beta_{ub} = K_{tip}/K_o$, where $K_o = \sqrt{(\pi a_o)}$ is the crack tip stress intensity factor that would result if the material were homogeneous. Then, if β_{ub} is less than unity, K_{tip} is less than it would be in a homogeneous material, and the composite is toughened. Also, the interface normal stress $\sigma_i^{(u)}$ and the upstream matrix stress $\sigma_m^{(u)}$ are reported, as described in §4.1.5.

4.2.1.1 Toughening

Figure 4.7 summarizes the toughening results of the unbridged analyses and indicates the variation of β_{ub} with the stiffness ratio E_f/E_m and crack tip position d_{tip}/d_m. Recall that d_{tip} is the distance of the crack tip from the inner edge of the downstream fiber and d_m is the inner edge-to-edge distance between the upstream and downstream fibers, as shown in Fig. 4.4. Figure 4.7 indicates that the composite is always toughened (i.e., $\beta_{ub} < 1$) for E_f greater than E_m. As expected, toughening in the unbridged configuration increases with higher ratios of E_f/E_m and d_{tip}/d_m, i.e., as the nearest inhomogeneity becomes stronger and closer to the crack tip. These results indicate that a tougher unbridged composite may be obtained by increasing fiber stiffness and reducing fiber diameter (i.e., fiber spacing).

4.2.1.2 Stresses

The mode I crack loading creates a severe tensile stress field in the vicinity of the crack tip. This tensile field should both reduce the compression at the fiber/matrix interface and increase the tension in the matrix near the crack tip. Figures 4.8 and 4.9 support these assertions and

48

also indicate how the interface and matrix stresses, given by $\sigma_i^{(u)}/\sigma_i^{(o)}$ and $\sigma_m^{(u)}/\sigma_m^{(o)}$, respectively, depend on the crack tip position d_{tip}/d_m and stiffness ratio E_f/E_m. These figures show that the highest principle stress in the upstream matrix region, $\sigma_m^{(u)}$, increases and the upstream interfacial compression, $\sigma_i^{(u)}$, decreases as the crack approaches the upstream fiber and as the stiffness ratio decreases. Note that the upstream matrix stress concentration $\sigma_m^{(u)}/\sigma_m^{(o)}$ is typically high (in the range 3 to 5) while the reduction in upstream interface compression $\sigma_i^{(u)}/\sigma_i^{(o)}$ is generally less than 5%. The dependence on stiffness ratio is expected from §4.2.1.1 where K_{tip} is found to increase as E_f/E_m decreases. The observed effect of crack-tip position, however, is in contrast to the above toughening results (β_{ub} decreases as d_{tip}/d_m increases). The stresses $\sigma_i^{(u)}$ and $\sigma_m^{(u)}$, rather, rise with d_{tip}/d_m as the trend in decreasing K_{tip} is outweighed by the increasing proximity of the crack tip to the location of the stresses.

These unbridged model stress results indicate that upstream interface slipping/debonding is unlikely, since $\sigma_i^{(u)}$ only decreases slightly from the initial interface compression $\sigma_i^{(o)}$. The lack of upstream fiber debonding subsequently perpetuates the unbridged configuration by restraining fiber pullout. Additionally, the stress results illustrate a high stress concentration in the upstream matrix region, indicating likely fracture there. Typically, the crack in an unbridged composite is understood to propagate by successive matrix/fiber/matrix fracture. The generally high toughness of reinforcing fibers and the high stress concentration in the upstream matrix region, however, could cause a more complex crack propagation process in an unbridged composite. For instance, the upstream matrix region may fail before the tough upstream fiber, which, in turn, could then cause the fiber to fail,

due to the lack of debonding. This failure process would proceed as matrix/upstream matrix/fiber, rather than the simple process described above. In either case, however, the unbridged crack is self perpetuating, i.e., it creates upstream conditions (no debonding, high matrix stress concentration) conducive to further fiber failure.

4.2.2 Bridged Model

In the bridged analyses, toughening is due to both inhomogeneity and fiber bridging effects. As described in §4.1.4, the steady-state portion of the bridged crack does not contribute to the K_{tip}, and the resulting toughening is independent of the total crack length a_0. Rather, the bridged toughening parameter β_{ss} relates the toughening to the fiber size, which controls the size of the high-gradient, crack-tip bridging region. For the cases examined here, β_{ss} is $O(1)$, indicating that the effective size of the crack is on the order of the fiber size. The upstream interface and matrix region stresses are described by the ratios $\sigma_i^{(u)}/\sigma_i^{(o)}$ and $\sigma_m^{(u)}/\sigma_m^{(o)}$, respectively. Note that these stress ratios and the bridged toughening parameter β_{ss}, due to the fiber pullout load-displacement behavior, are dependent on load level $\sigma_c/\tau_i^{(o)}$, friction coefficient μ and stiffness ratio E_f/E_m in addition to crack tip position d_{tip}/d_m. The effect of friction coefficient, however, is found to be small in the toughening results and thus the dependence of $\sigma_i^{(u)}$ and $\sigma_m^{(u)}$ on μ are not reported here.

4.2.2.1 Toughening

Figure 4.11a illustrates typical load dependence of the toughening parameter β_{ss} when $E_f/E_m = 1$ and $d_{tip}/d_m = 50.0\%$. Note that $\beta_{ss} \approx 1$ and subsequently $K_{tip} \approx \sigma_c\sqrt{(\pi d_f)}$, indicating the small effective crack length. The toughening is directly controlled by the steady-state fiber pullout behavior --

β_{ss} is smallest (and the toughening maximum) when the bridging load-displacement behavior is stiffest (when the fibers are sticking). At higher loads, the bridging fibers slip and the pullout response softens (as shown in Fig. 3.21) causing β_{ss} to increase and the toughening to decrease.

Figures 4.11a through 4.11c show the dependence of β_{ss} on interfacial friction coefficient μ for stiffness ratios E_f/E_m of 1, 2 and 4 when $d_{tip}/d_m =$ 50.0%. Note that in Fig. 4.11a, when $E_f/E_m = 1$, β_{ss} is independent of the friction coefficient. Additionally, in all Figs. 4.11a through 4.11c, the toughening during sticking (small $\sigma_c/\tau_i^{(o)}$) does not depend on μ. The results of Chapter 3 predict this behavior; the linear sticking steady-state fiber pullout response (and the nonlinear slipping response when $E_f/E_m = 1$) is independent of μ. In Figs. 4.11b and 4.11c, where $E_f/E_m = 2$ and 4, respectively, the toughening increases subtly with μ as slipping increases; this is predicted in Fig. 3.21b, which shows steady-state fiber pullout response stiffening slightly with increasing friction coefficient.

The effect of stiffness ratio E_f/E_m on the toughening parameter β_{ss} when $\mu = 0.45$ and $d_{tip}/d_m = 16.7\%$, 50.0% and 83.3% is shown in Figs. 4.12a through 4.12c, respectively. Note that at all crack tip positions the toughening is strongly dependent on E_f/E_m and increases as this ratio increases. This behavior is again predicted in Fig. 3.21a, which shows fiber pullout stiffening strongly with increasing E_f/E_m, and by the unbridged analyses of §4.2.1.1 which indicate fiber/crack-tip toughening effects increasing with E_f/E_m.

Figures 4.13a through 4.13c show the variation of the toughening parameter β_{ss} with crack tip position d_{tip}/d_m when $\mu = 0.45$ and $E_f/E_m = 1$, 2 and 4, respectively. These figures indicate a reduction in the toughening as the crack tip departs from the downstream fiber and its bridging effects

51

decrease. These toughening results are in contrast to the trends observed in the unbridged model and indicate the dominance of the fiber bridging among the various toughening mechanisms.

The above numerical toughening results compare favorably with the limited experimental values obtained in the literature. The experimental results of Ref. [5] are used here as an illustration because of the superior test methodology employed by Bhatt and Phillips, i.e., tensile testing instead of flexure testing is used. Bhatt and Phillips report a matrix microcracking stress of 33 - 40 ksi for the $\approx$30% volume fraction SCS-6/RBSN composite. The stiffness of the fibers and matrix are 16 and 60 Msi, respectively, while the fiber diameter is 0.0056 inches, and a typical toughness K_{Ic} of the low density RBSN matrix is 3 ksi$\sqrt{}$in. The nominal interfacial shear stress $\tau_i^{(o)}$ is estimated to be near 2.5 ksi in [5], giving $\sigma_c/\tau_i^{(o)} \approx 14$ at microcracking. The friction coefficient is not reported in [5], but its effect is small, as seen in Fig. 4.11. From Fig. 4.12, the least toughening (i.e., largest β_{ss}) for $\sigma c/\tau_i^{(o)} \approx 14$ and $E_f/E_m \approx 3.8$ occurs at $d_{tip}/d_m = 83.3\%$ and yields the toughening parameter $\beta_{ss} \approx 0.6$. These values of β_{ss}, d_f and $K_{Ic}^{(m)}$, and the definition of Eq. (4.2) yield a predicted composite matrix microcracking stress of approximately 37 ksi, very near the experimentally measured values.

To obtain a tougher bridged composite, the trends revealed by the bridged analysis indicate that friction coefficient μ and stiffness ratio E_f/E_m should be large while fiber diameter should be small. A large friction coefficient and stiffness ratio reduce K_{tip} by decreasing the toughening parameter β_{ss}. A decreasing fiber diameter, however, lessens Ktip not by reducing β_{ss}, but by lowering the reference stress intensity factor $K_f = \sigma_c\sqrt{(\pi d_f)}$.

In the Figs. 4.11 through 4.13, the highest toughening occurs when the fibers are sticking. Thus, these figures indicate that the maximum composite toughness occurs when the nominal slipping shear stress $\tau_i^{(o)}$ is large enough to prevent fiber slipping. Realistically, however, if $\tau_i^{(o)}$ is too large the fibers may fail before the composite microcracks, thus eliminating the fiber bridging. The critical condition, i.e. when the fibers fail as the matrix microcracks, is given from Eqs. (4.2) and (4.3) when $K_{tip} = K_{Ic}^{(m)}$ and $\sigma_c = V_f * \sigma_{ult}^{(f)}$,

$$\beta_{ss}^{crit} = K_{Ic}^{(m)}/[V_f \sigma_{ult}^{(f)} \sqrt{(\pi d_f)}]. \tag{4.6}$$

As an illustration, in the experimental example above where $K_{Ic}^{(m)} \approx 3$ ksi$\sqrt{\text{in}}$, $\sigma_{ult}^{(f)} \approx 550$ ksi, $d_f \approx 0.0056$, and $V_f \approx 30\%$, the critical bridging toughening parameter β_{ss}^{crit} is approximately 0.14. Thus, for $\beta_{ss} < 0.14$, the SCS-6/RBSN composite will fail in a catastrophic manner -- composite failure will occur before microcracking. The toughening Figs. 4.11 - 4.13, however, indicate that for $E_f/E_m \approx 3.8$, the toughening parameter β_{ss} is always greater than β_{ss}^{crit}. Thus, ideally, the SCS-6/RBSN composite should always fail non-catastrophically. In-situ degradation of fiber and matrix properties, and other realistic effects, however, could limit the actual performance of the composite.

4.2.2.2 Stresses

Similar to the unbridged model, the loading of the bridged crack causes a reduction in the compression at the fiber/matrix interface ahead of the crack tip. This effect, and its dependence on load σ_c and stiffness ratio E_f/E_m when $d_{tip}/d_m = 50.0\%$ is shown in Fig. 4.14. For relatively small loads ($\sigma_c/\tau_i^{(o)} > 2$) the decrease in $\sigma_i^{(u)}$ is larger than that observed in the unbridged model. Note that at higher loads the stress $\sigma_i^{(u)}$ is zero for $E_f/E_m = 1$ and

$E_f/E_m = 2$, indicating interface opening ahead of the crack tip. At higher

loads than those investigated, the interface may also open for $E_f/E_m = 4$. Note

that in Fig. 4.12b, however, the load dependence of the toughening for $E_f/E_m =$

2 (interface opens) and $E_f/E_m = 4$ (interface remains closed) is similar,

indicating that the toughening is not significantly affected by the interface

opening ahead of the crack tip. In agreement with the bridged model

toughening results, the loss of interface compression is less severe as the

stiffness ratio increases, due to an accompanying decrease in K_{tip}.

Figure 4.15 illustrates the effect of crack tip position d_{tip}/d_m and

applied load σ_c on the interface compression immediately ahead of the crack

when $E_f/E_m = 4$. As expected from the toughening results, as the crack

approaches the upstream interface (d_{tip}/d_m increases) the interface

compression is reduced. When the crack tip is at the closest position (d_{tip}/d_m

= 83.3%) the interface opens at medium loads ($\sigma_c/\tau_i^{(o)} > 5$) ahead of the crack

tip. The interface opening, however, does not adversely affect the load-

dependent behavior of the toughening, as shown in Fig. 4.13c.

In contrast to the unbridged model results, the stress concentration in

the first uncracked upstream matrix region of the bridged model is typically

small (near unity), due to the strong restraining effect of the bridging fibers.

Figures 4.16 and 4.17 illustrate the variation of the upstream matrix stress

concentration $\sigma_m^{(u)}/\sigma_m^{(o)}$ with remote applied load σ_c, stiffness ratio E_f/E_m, and

crack tip position d_{tip}/d_m. The effects of σ_c, E_f/E_m and d_{tip}/d_m are similar to

the trends seen in toughening. As σ_c and d_{tip}/d_m increase and as E_f/E_m

decreases the stress concentration $\sigma_m^{(u)}/\sigma_m^{(o)}$ rises along with K_{tip}.

Thus, in the bridged analysis, the stress results exhibit trends similar

to the toughening results. The observed stresses also indicate that interface

opening ahead of the crack tip is likely, although this opening does not adversely affect toughening. Interfacial opening, however, does promote easier fiber pullout and thus serves to perpetuate the bridging. Also, the stress concentration in the upstream matrix is small, indicating the very local nature of the crack-tip singular stress field. Thus, the crack propagation is controlled by localized fracture at the crack tip -- the low values of $\sigma_m^{(u)}/\sigma_m^{(o)}$ indicate a low likelihood of "premature" matrix failure (i.e. failure ahead of the crack tip) in the upstream matrix region. Subsequently, some three-dimensional propagation mechanism (crack front bowing for instance) must be active for the crack to pass the upstream fibers. Regardless of the fiber-passing mechanism, however, the stress results indicate that the bridged crack is self perpetuating -- it creates upstream conditions (interface debonding and controlled, local matrix fracture) conducive to sustained bridging during crack propagation.

5. CONCLUSIONS

Toughening mechanisms of fiber-reinforced ceramic composites have been investigated, specifically including the dominant and controlling two-dimensional mechanisms of crack bridging and crack-tip/fiber interaction. To better understand the crack bridging process, fiber pullout mechanics were investigated and dominant two-dimensional elasticity solutions governing the pullout mechanisms were obtained. A two-dimensional finite element analysis employing the pullout results modeled both crack bridging and crack-tip/fiber interaction phenomena in an investigation of toughening mechanics. Additionally, specific stresses related to the crack propagation were reported. The results of the steady-state fiber pullout and composite toughening analyses can now be summarized.

5.1 STEADY-STATE FIBER PULLOUT

1. The interfacial shear stress varies exponentially in the sticking and slipping regions of two-dimensional steady-state fiber pullout. The governing exponential constants and the overall fiber and matrix stress fields (in the nonsingular regions) have been obtained for various geometries and material properties.

2. In the sticking region the interfacial shear stress always decays such that isostrain is obtained away from the free edge.

3. In the slipping region for most typical composite configurations (E_f/E_m > 1, $\nu_f \leq \nu_m$) the fiber/matrix interface compression increases during pullout, tending to increase slipping friction and decrease the likelihood of debonding.

4. The stick/slip, pullout force-crack opening displacement response of steady-state fiber pullout is dominated by the interfacial shear stress variation in the sticking and slipping regions. Although earlier analyses reasonably predict the overall pullout response, they neglect the realistic stick/slip, linear/nonlinear behavior modeled by the current analysis.

5. Comparison with the current analytical results indicate the straight-forward finite element methods that were employed in the composite toughening model accurately simulate the overall two-dimensional fiber pullout response.

5.2 COMPOSITE TOUGHENING

5.2.1 Unbridged Model

1. Crack-tip/fiber interaction toughening in the unbridged configuration follows expected trends, increasing with stiffness ratio and proximity of the crack tip to the stiff upstream fiber.

2. In the range of parameters investigated here, the reduction of K_{tip} due to the inhomogeneity is typically within 0 - 30%, indicating substantial toughening.

3. The crack loading reduces the compression at the immediate upstream interface only slightly, typically by less than 5%. This small reduction in interface compression diminishes the potential for fiber pullout.

4. The crack loading causes a high stress concentration in the upstream (uncracked) matrix region, indicating likely matrix failure there.

5. The lack of fiber/matrix debonding and high stress concentration in the uncracked upstream matrix are not conducive to crack bridging, thus serving to sustain the unbridged crack propagation.

57

5.2.2 Bridged Model

1. The composite toughening in the bridged configuration is independent of the total crack length a_o. The bridged toughening parameter β_{ss} is typically $O(1)$, indicating that the effective length of the crack is of the order of the fiber size, due to the steady-state bridging.

2. The composite toughening increases with fiber/matrix stiffness ratio and interfacial friction coefficient, but decreases with increased remote loading. This toughening behavior is a direct result of the steady-state bridging load-displacement behavior which stiffens with increasing fiber/matrix stiffness ratio, increasing friction coefficient, and decreasing remote applied load. For a given composite configuration, the highest toughening occurs when the fibers are sticking.

3. The toughening decreases as the crack tip departs the downstream fiber and approaches the upstream fiber, illustrating the dominance of the crack bridging over the crack-tip/fiber toughening mechanism.

4. The crack loading greatly reduces the interface compression at the immediate upstream interface, promoting fiber debonding. In some of the bridged composite models analyzed, the interface opens. The interface opening, however, does not adversely affect the composite toughening.

5. The crack-tip K-field is very localized within the cracked matrix region. Subsequently, the stress concentration in the upstream (uncracked) matrix region is small, typically near unity, indicating unlikely matrix failure there.

6. The promotion of fiber debonding and the controlled, local nature of the matrix fracture are conducive to crack bridging, thus serving to sustain the bridged crack propagation.

6. ACKNOWLEDGEMENTS

REFERENCES

1. DiCarlo, J. A., "Fibers for Structurally Reliable Metal and Ceramic Composites," Journal of Metals, Vol. 37, No. 6, pp. 44-49, 1985.

2. Clark, T. J. et. al., "Thermal Degradation of Nicalon SiC Fibers," Ceramic Engineering Science Proceedings, Vol. 6, No. 7-8, pp. 576-588, 1985.

3. Rice, R. W. et. al., "Thermal Structural Ceramic Composites," Ceramic Engineering Science Proceedings, Vol. 1, No. 7-8(A), pp. 424-443, 1980.

4. Shetty, D. K. et. al., "SiC Monofilament-Reinforced Si_3N_4 Matrix Composites," Ceramic Engineering Science Proceedings, Vol. 6, No. 7-8, pp. 632-645, 1985.

5. Bhatt, R. T. and Phillips, R. E., "Laminate Behavior for SiC Fiber-Reinforced Reaction-Bonded Silicon Nitride Matrix Composites," NASA Technical Report 88-C-30, 1985.

6. Corbin, N. D., Rossetti, G. A. and Hartline, S. D., "Microstructure/Property Relationships for SiC Filament-Reinforced RBSN," Ceramic Engineering Science Proceedings, Vol. 7, No. 7-8, pp. 958-968, 1985.

7. Corbin, N. D., Willkens, C. A. and Hartline, S. D., "The Influence of Interfacial Modifiers on RBSN Matrix Composite Properties," in Metal Matrix, Carbon, and Ceramic Matrix Composites, NASA Conference Publication 2482, ed. J. D. Buckley, pp. 365-379, 1987.

8. Stinton, D. P., Caputo, A. J. and Lowden, R. A., "Synthesis of Fiber-Reinforced SiC Composites by Chemical Vapor Infiltration," American Ceramic Society Bulletin, Vol. 65, No. 2, pp. 347-350, 1986.

9. Lamicq, P. J. et. al., "SiC/SiC Composite Ceramics," American Ceramic Society Bulletin, Vol. 65, No. 2, pp. 336-338, 1986.

10. Moeller, H. H. et. al., "Fiber-Reinforced Ceramic Composites," Ceramic Engineering Science Proceedings, Vol. 8, No. 7-8, pp. 977-984, 1987.

11. Fitzer, E. and Ranier, G., "Fiber-Reinforced Silicon Carbide," American Ceramic Society Bulletin, Vol. 65, No. 2, pp. 326-335, 1986.

12. Aveston, J., Cooper, G. A. and Kelly, A., in The Properties of Fibre Composites, pp.15-26. Conference Proceedings, National Physical Laboratory, Guildford, IPC Science and Technology Press Ltd, 1971.

13. Marshall, D. B., Cox, B. N. and Evans, A. G., "The Mechanics of Matrix Cracking in Brittle-Matrix Fiber Composites," Acta Metallurgy, Vol. 33, No. 11, pp. 2013-2021, 1985.

14. Budiansky, B., Hutchinson J. W. and Evans A. G., "Matrix Fracture in Fiber-Reinforced Ceramics," Journal of Mechanics and Physics of Solids, Vol. 34, No. 2, pp. 167-189, 1986.

15. Budiansky, B. and Amazigo, J. C., "Toughening by Aligned, Frictionally Constrained Fibers," Journal of Mechanics and Physics of Solids, Vol. 37, No. 1, pp. 93-109, 1989.

16. Rose, L. R. F., "Crack Reinforcement by Distributed Springs," Journal of Mechanics and Physics of Solids, Vol. 35, No. 4, pp. 383-405, 1987.

17. Majumdar, B. S., Newz, G. M. and Rosenfield, A. R., "Yielding Behavior of Ceramic Matrix Composites," to be published in the Proceedings of the Seventh International Conference on Fracture - ICF7, Houston, 1989.

18. Faber, K. T. and Evans, A. G., "Crack Deflection Processes - I. Theory," Acta Mettalurgy, Vol. 31, No. 4, pp. 565-576, 1983.

19. Cotterell, B. and Rice, J. R., "Slightly Curved or Kinked Cracks," International Journal of Fracture, Vol. 16, No. 2, pp. 155-169, 1980.

20. Seshadri, S. G., Srinivasan, M. and Keeler, K. M., "Numerical Computation of the Toughening Increments Due to Crack Deflection in Particulate Composites," Ceramic Engineering Science Proceedings, Vol. 8, No. 7-8, pp. 671-684, 1987.

21. Tamate, O., "The Effect of a Circular Inclusion on the Stresses Around a Line Crack in a Sheet Under Tension," International Journal of Fracture Mechanics, Vol. 4, No. 3, pp. 257-265, 1968.

22. Tirosh, J. and Tetelman, A. S., "Fracture Conditions of a Crack Approaching a Disturbance," International Journal of Fracture, Vol. 12, No. 2, pp. 187-199, 1976.

23. Khaund, K. A., Kristic, V. D. and Nicholson, P. S., "Influence of Elastic Thermal Mismatch on the Local Crack-Driving Force in Brittle Composites," Journal of Material Science, Vol. 12, pp. 2269-2273, 1977.

24. Zak, A. R. and Williams, M. L., "Crack Point Stress Singularities at a Bi-Material Interface," Journal of Applied Mechanics, Vol. 30, pp. 142-143, 1963.

25. Krapkov, A. A., "First Fundamental Problem for a Piecewise-Homogeneous Plane with a Slit Perpendicular to the Line of Seperation," Journal of Applied Math and Mechanics, Vol. 32, No. 4, pp. 666-678, 1968.

26. Cook, T. S. and Erdogan, F., "Stresses in Bonded Materials with a Crack Perpendicular to the Interface," International Journal of Engineering Science, Vol. 10, pp. 677-697, 1972.

27. Hilton, P. D. and Sih, G. C., "A Laminate Composite with a Crack Normal to the Interfaces," International Journal of Solids and Structures, Vol. 7, pp. 913-930, 1971.

28. Lange, F. F., "The Interaction of a Crack Front with a Second-Phase Dispersion," Philosophical Magazine, Vol. 22, pp. 983-992, 1970.

29. Evans, A. G., "The Strength of Brittle Materials Containing Second Phase Dispersions," Philosophical Magazine, Vol. 26, pp. 1327-1344, 1972.

30. Green, D. J., Nicholson, P. S. and Embury, J. D., "Fracture of a Brittle Particulate Composite," Journal of Material Science, Vol. 14, pp. 1657-1661, 1979.

31. Rose, L. R. F., "Toughening Due to Crack-Front Interaction with a Second-Phase Dispersion," Mechanics of Materials, Vol. 6, pp. 11-15, 1987.

32. Lange, F. F. and Radford, K. C., "Fracture Energy of an Epoxy," Journal of Material Science, Vol. 6, pp. 1197-1210, 1971.

33. Pipes, R. B. and Pagano, N. J., "Interlaminar Stresses in Composite Laminates Under Uniform Axial Extension," Journal of Composite Materials, Vol. 4, pp. 538-548, 1970.

34. Wang, S. S. and Choi, I., "Boundary-Layer Effects in Composite Laminates," Journal of Applied Mechanics, Vol. 49, pp. 541-560, 1982.

35. Comninou, M., "The Interface Crack," Journal of Applied Mechanics, Vol. 44, pp. 631-636, 1977.

36. Comninou, M., "Interface Crack With Friction in the Contact Zone," Journal of Applied Mechanics, Vol. 44, pp. 780-781, 1977.

37. Comninou, M., "The Interface Crack in a Shea   ," Journal of Applied Mechanics, Vol. 45, pp. 287-290, 1978.

38. Comninou, M. and Schmueser, D., "The Interface Crack in a Combined Tension-Compression and Shear Field," Journal of Applied Mechanics, Vol. 46, pp. 345-358, 1979.

39. Bogey, D. B., "Two Edge-Bonded Elastic Wedges of Different Materials and Wedge Angles Under Surface Tractions," Journal of Applied Mechanics, Vol. 38, pp. 377-386, 1971.

40. Timoshenko, S. P. and Goodier, J. N., Theory of Elasticity, Third Edition, McGraw Hill Book Co., Inc., New York, 1970.

41. Rosen, B. W., "Mechanics of Composite Strengthening," in Fiber Composite Materials, American Society for Metals, Ohio, 1964, Chapter 3.

42. Cox, H. L., "The Elastic and Strength of Paper and other Fibrous Materials," <u>British Journal of Applied Physics</u>, Vol. 3, pp. 72-79, 1952.

43. Carrara, A. S. and McGarthy, F. J., "Matrix and Interface Stresses in a Discontinuous Fiber Composite Model," <u>Journal of Composite Materials</u>, Vol. 2, No. 2, pp. 222-243, 1968.

44. MacLaughlin, T. F. and Barker, R. M., "Effect of Modulus Ratio on Stress Near a Discontinuous Fiber," <u>Experimental Mechanics</u>, Vol. 4, No. 2, pp. 178-183, 1972.

45. Agarwal, B. D. and Broutman, L. J., <u>Analysis and Performance of Fiber Composites</u>, John Wiley and Sons, Inc., New York, 1980.

46. Cook, R. D., <u>Concepts and Applications and Applications of Finite Element Analysis</u>, Second Edition, John Wiley and Sons, Inc., New York, 1981.

47. Bathe, K. J., <u>Finite Element Procedures in Engineering Analysis</u>, Prentice-Hall, Englewood Cliffs, 1982.

48. Rice, J. R., "A Path Independent Integral and the Approximate Analysis of Strain Concentration by Notches and Cracks," <u>Journal of Applied Mechanics</u>, Vol. 35, pp. 379-385, 1968.

49. Parks, D. M., "A Stiffness-Derivative Finite Element Technique for Determination of Elastic Crack Tip Stress Intensity Factors," <u>International Journal of Fracture</u>, Vol. 10, pp. 487-502, 1974.

50. Parks, D. M., "The Virtual Crack Extension Method for Nonlinear Material Behavior," <u>Computer Methods in Applied Mechanics and Engineering</u>, Vol. 12, pp. 353-364, 1977.

51. Broek, D., <u>Elementary Engineering Fracture Mechanics</u>, Third Edition, Matrinus Nijhoff Publishers, Boston, 1982.

52. Kanninen, M. F. and Popelar, C. H., <u>Advanced Fracture Mechanics</u>, Oxford University Press, New York, 1985.

Configuration	Loading	Error(%)
Isotropic, Homogeneous Griffith-Cracked Plate	External Remote Tension σ_c	0.2 [a]
Isotropic, Homogeneous Griffith-Cracked Plate	Internal Crack Face Pressure $(-\sigma_c)$	0.2 [a]
Isotropic, Homogeneous Griffith-Cracked Plate	Internal Crack Face Point Load P	0.5 [a]
Isotropic, Homogeneous Edge Cracked Plate	External Remote Tension σ_c	0.2 [a]
Bimaterial Plate $a_o/D = 0.85$ [d]	Internal Crack Face Pressure $(-\sigma_c)$	≈ 4 [b]
Bimaterial Plate $a_o/D = 0.99$	Internal Crack Face Pressure $(-\sigma_c)$	< 10 [b,c]

[a] See Ref. [51] for analytical solution.

[b] See Ref. [27] for analytical solution.

[c] This error is only an estimate. The results of Ref. [27] are given only for $a_o/D < 0.95$.

[d] Crack length is $2a_o$ and 2D is the distance between bimaterial interfaces.

Table 4.1. Comparison of finite element predictions and the analytical solutions for various test cases.

COMPOSITE BEHAVIOR

FIBER AND
COMPOSITE
FAILURE

MATRIX MICROCRACKING

MONOLITHIC MATRIX
BEHAVIOR

TENSILE STRESS
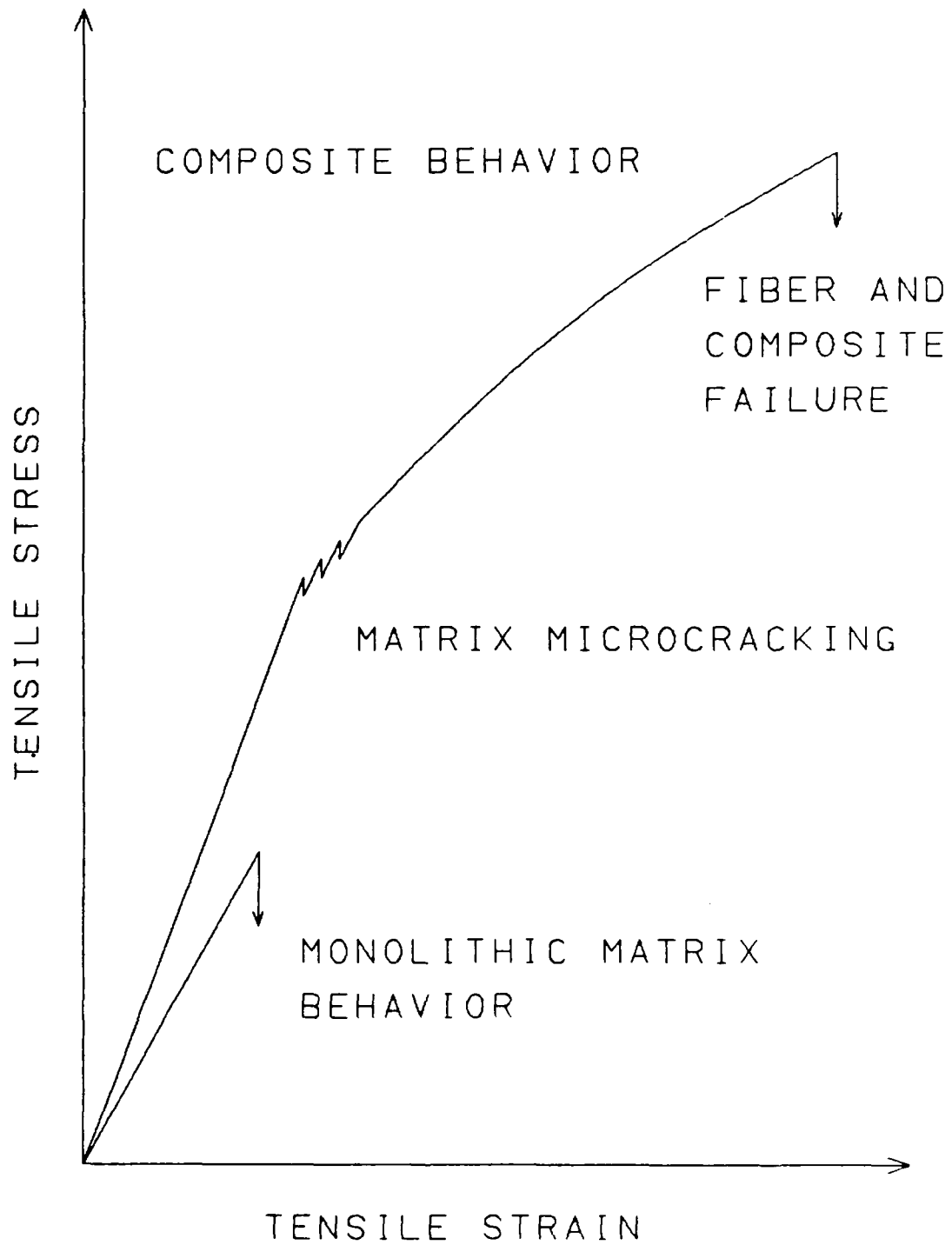
TENSILE STRAIN

Figure 1.1. Idealized longitudinal tensile stress–strain response of a unidirectional fiber reinforced ceramic composite.
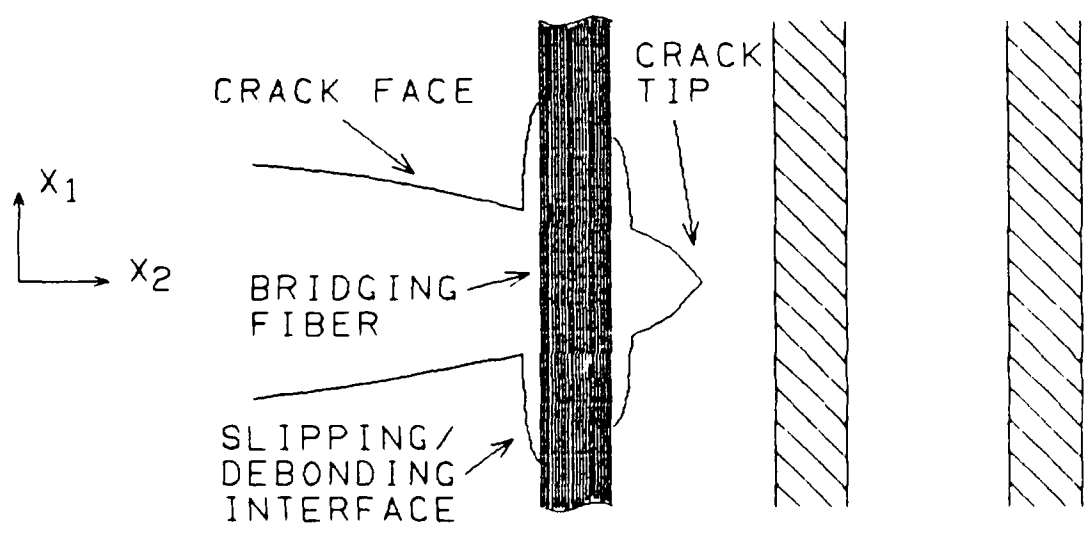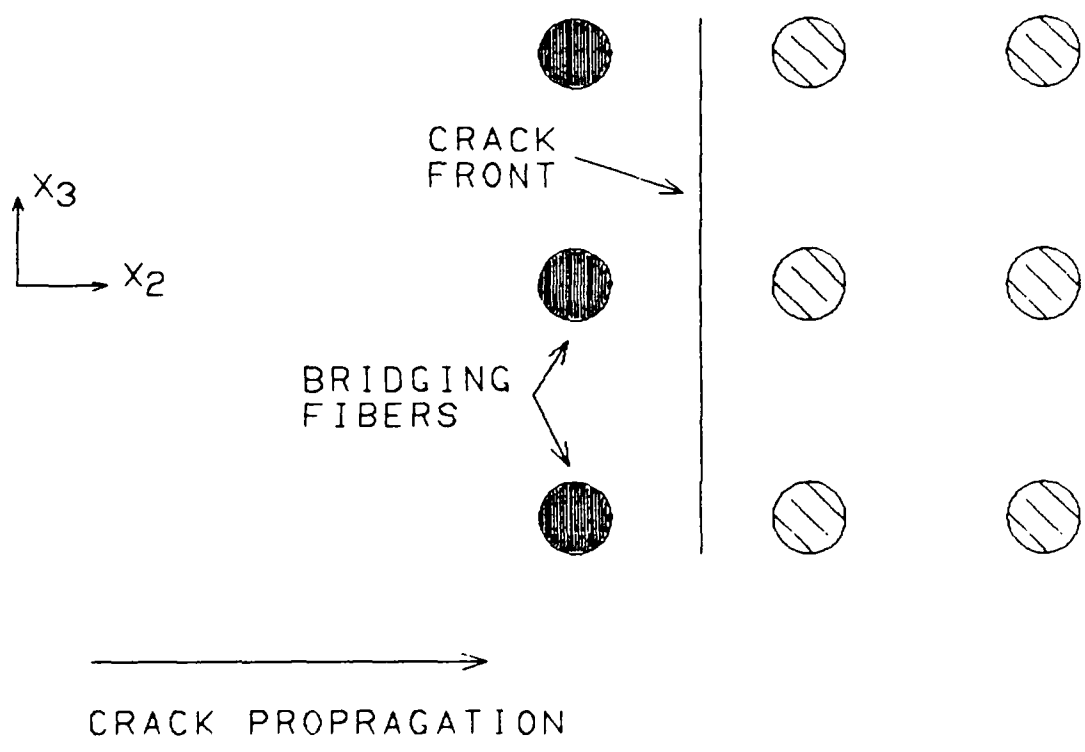
Figure 1.2a. Idealized initial configuration of a propagating crack in a unidirectional fiber reinforced ceramic. The crack front is straight and lies between bridged and approached fibers.
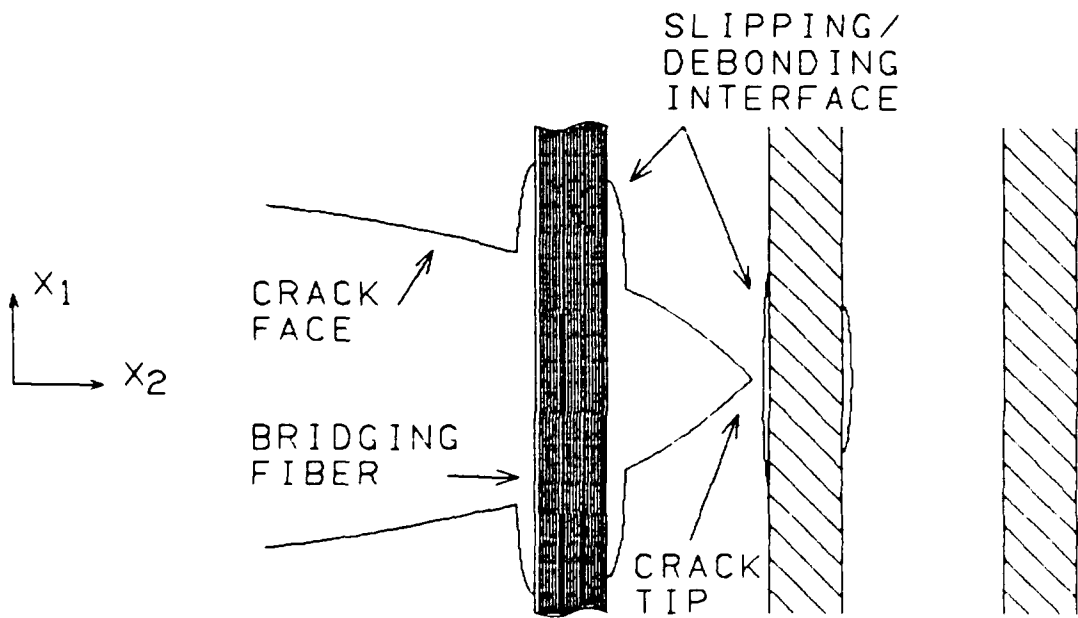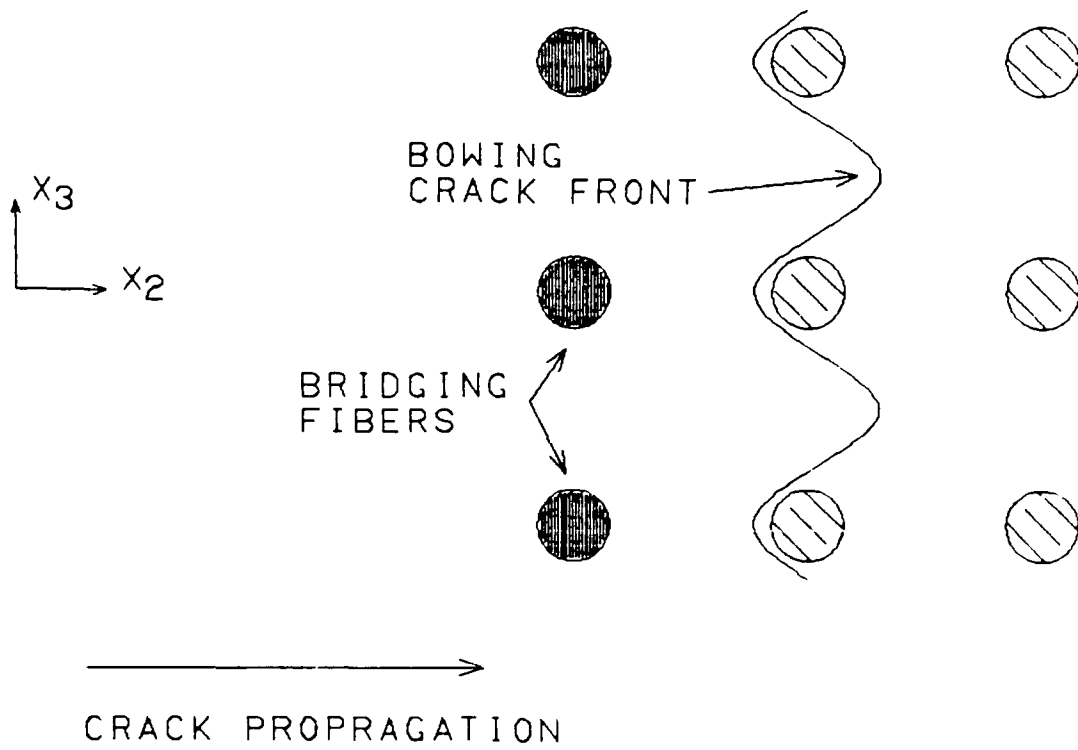
Figure 1.2b. Idealized bowing configuration of a propagating crack in a unidirectional fiber reinforced ceramic. The crack front bows out as it approaches the constraining fibers.

X3

X2

BOWING CRACKS
AT BREAKAWAY

SLIPPING/DEBONDING
FIBERS ENTERING CRACK

BRIDGING
FIBERS

CRACK PROPRAGATION

SLIPPING/
DEBONDING
INTERFACE

FIBER
ENTERING
CRACK

X1

X2

CRACK
FACE

BRIDGING
FIBER
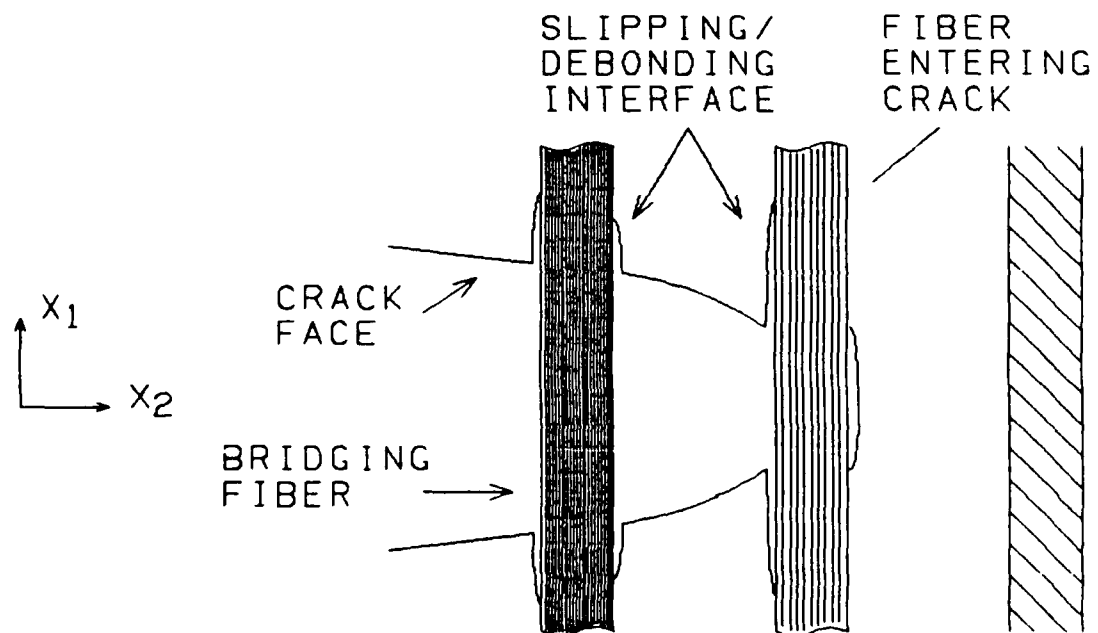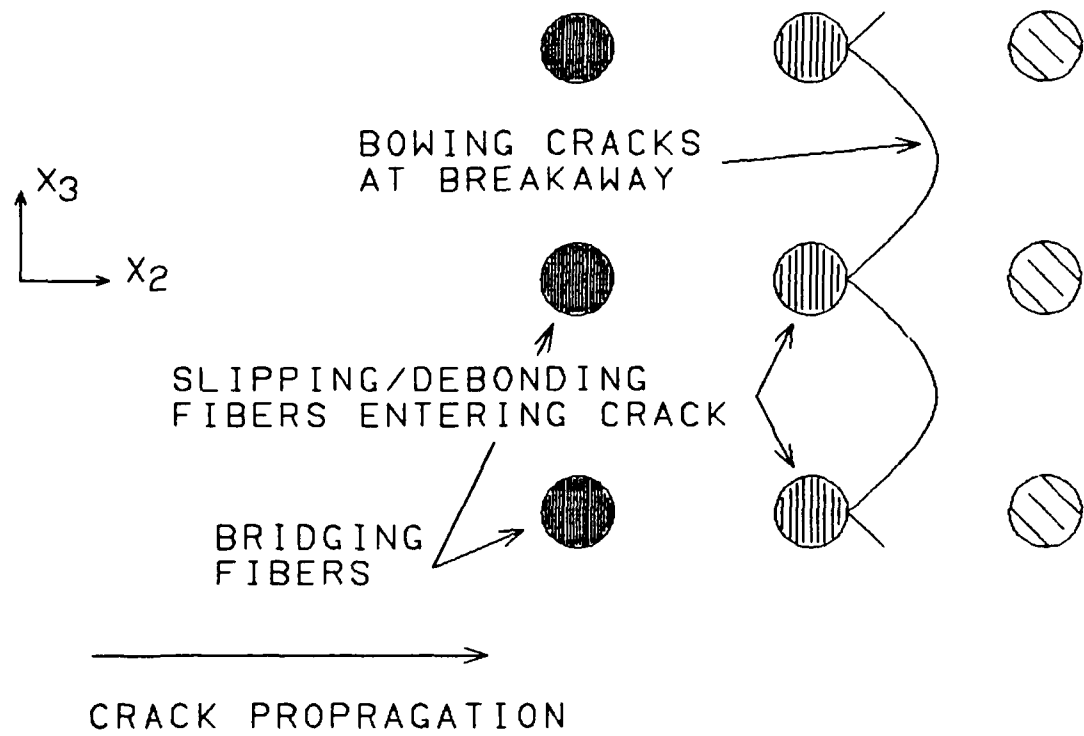
Figure 1.2c. Idealized breakaway configuration of a propagating crack in a unidirectional fiber reinforced ceramic. The seperate crack fronts between fibers join and breakaway as the fibers enter the crack.

BRIDGING
FIBERS

CRACK TIP REGION

$2V_o$

STEADY-STATE BRIDGING REGION
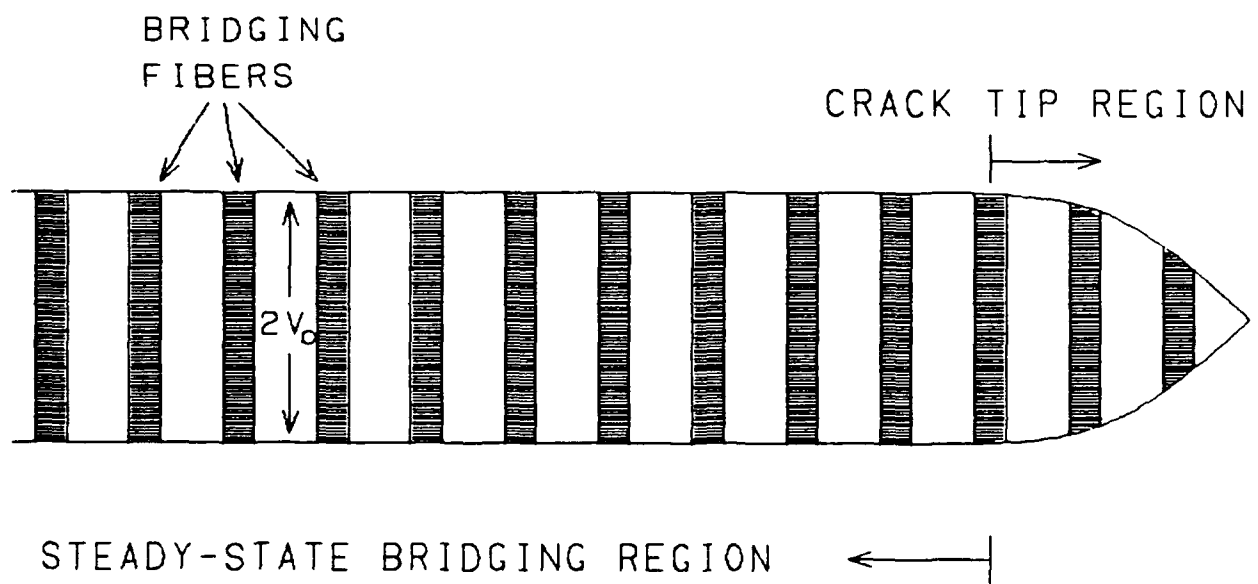
Figure 3.1a. Idealized steady-state bridging of a long crack.
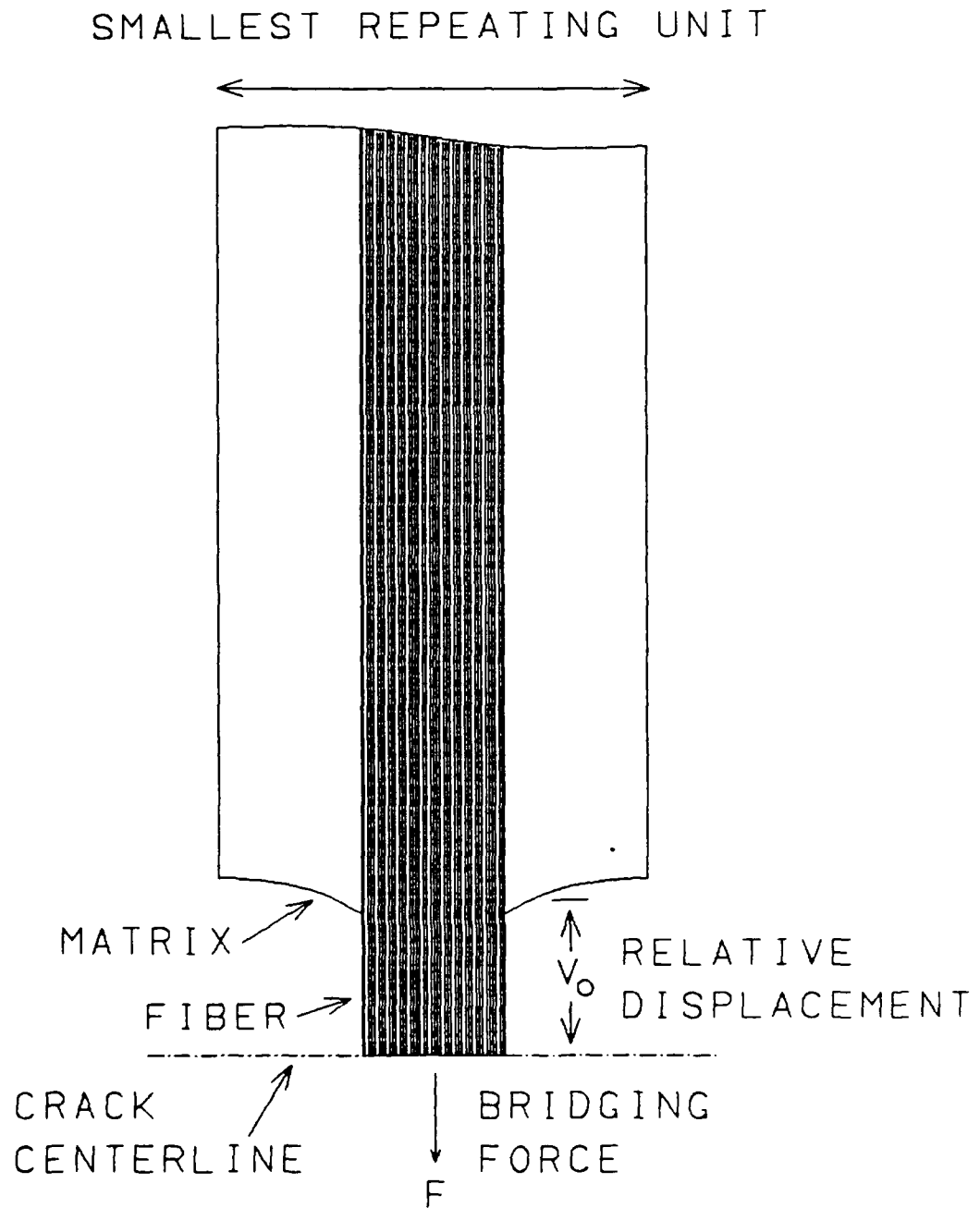
Figure 3.1b. A single pullout "unit cell" -- smallest repeating element around a fiber in the steady-state bridging region.

70
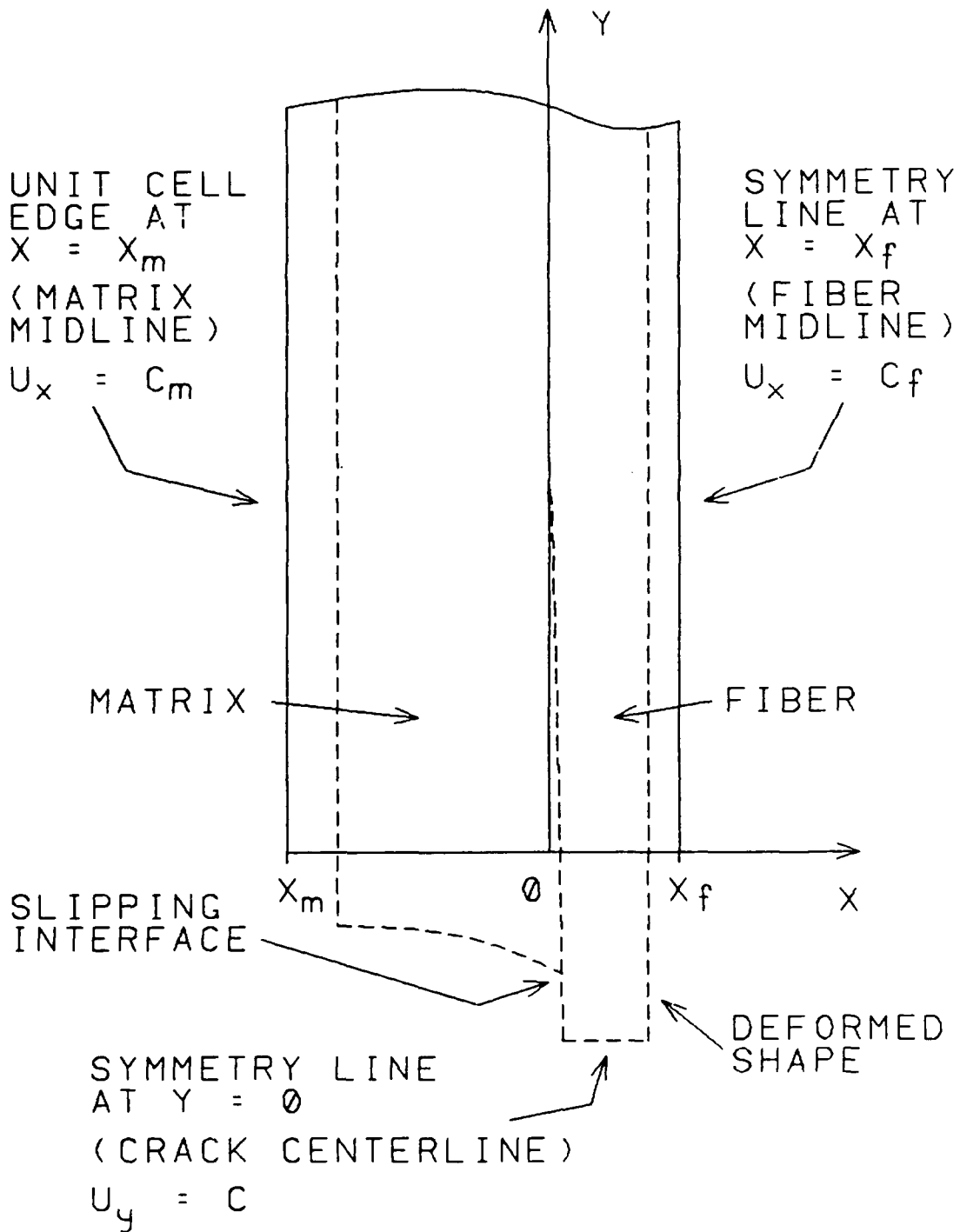
Figure 3.2. One symmetric half of the pullout unit cell and appropriate symmetry and periodicity boundary conditions. The interface along x = 0 is closed but frictionally slipping over some region.

71
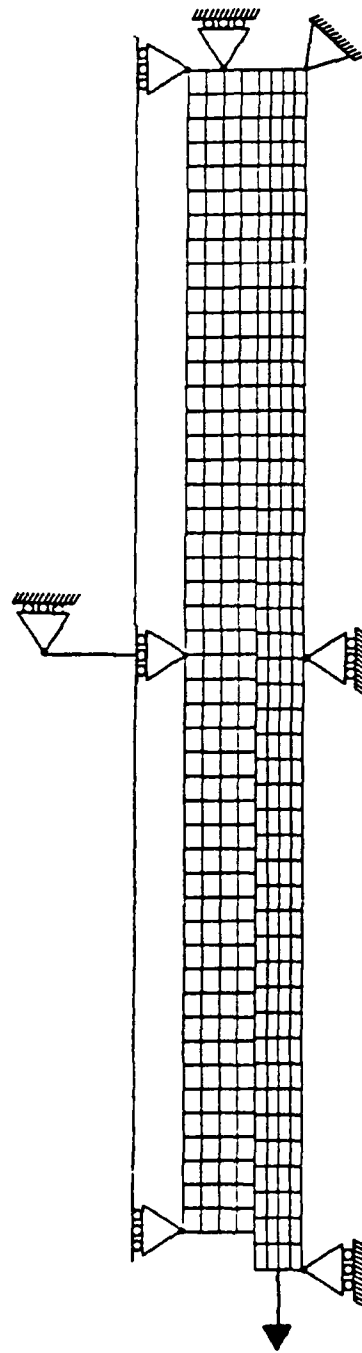
Figure 3.3. The finite element pullout model in a deformed configuration.
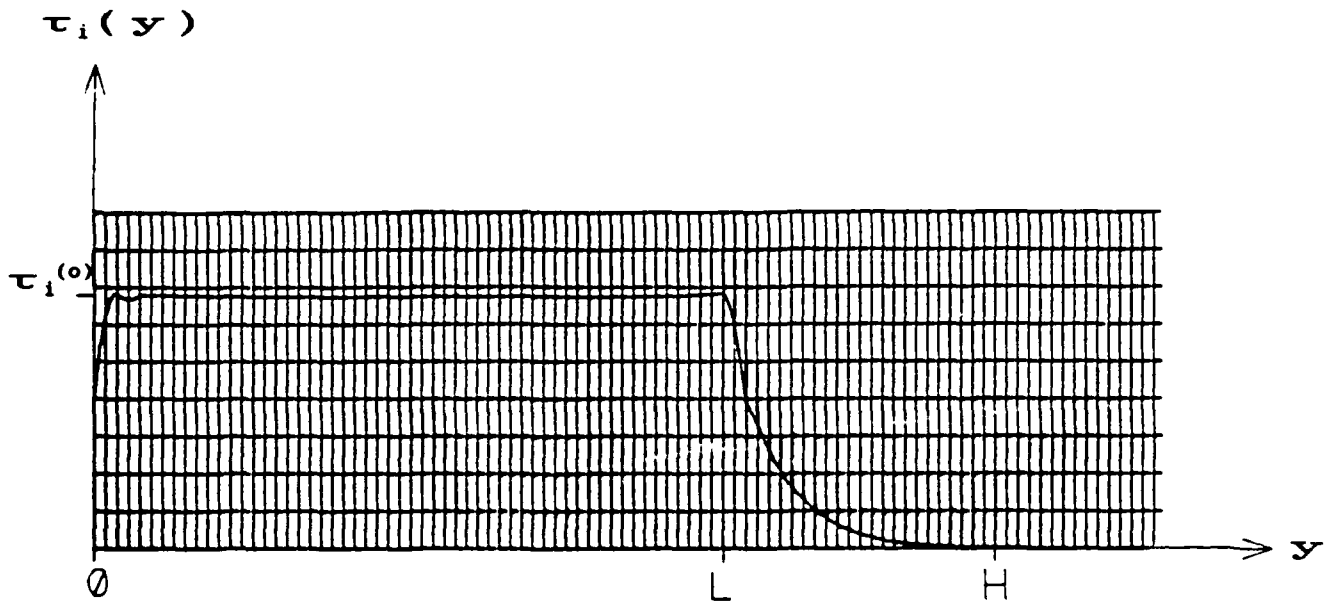
Figure 3.4a. Results of the finite element pullout model showing the interfacial shear stress τ_i when $E_f/E_m = 1$ and $\nu_f = \nu_m = 0.25$. The sticking point is at $y = L$.
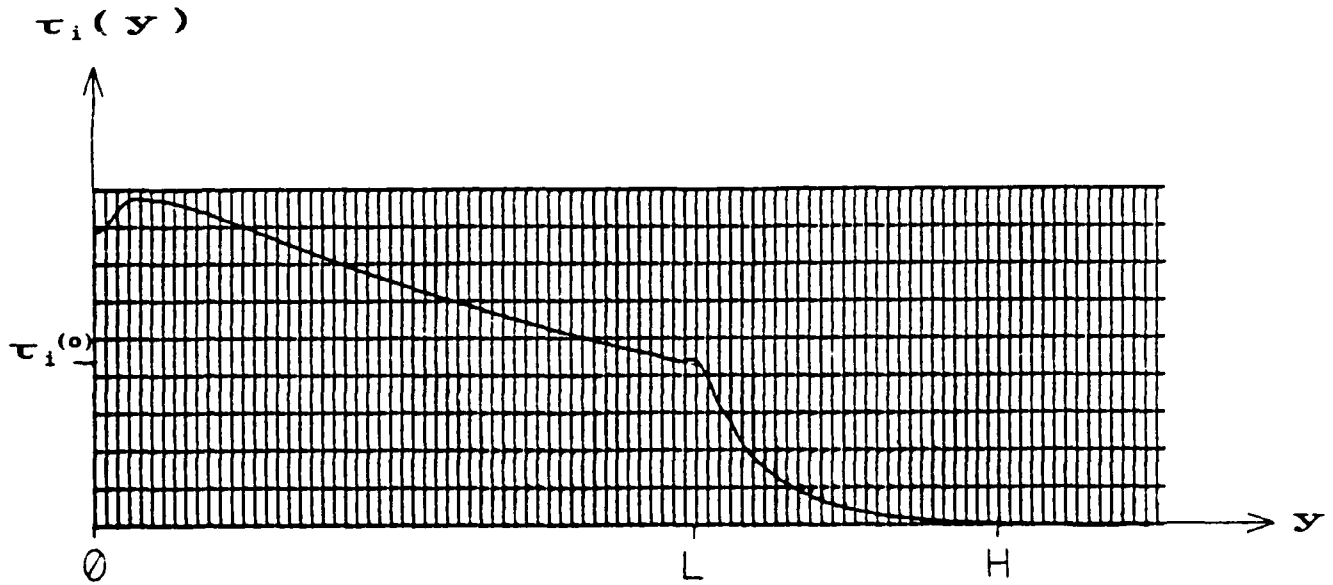
Figure 3.4b. Results of the finite element pullout model showing the interfacial shear stress τ_i when $E_f/E_m = 16$ and $\nu_f = \nu_m = 0.25$. The sticking point is at $y = L$.
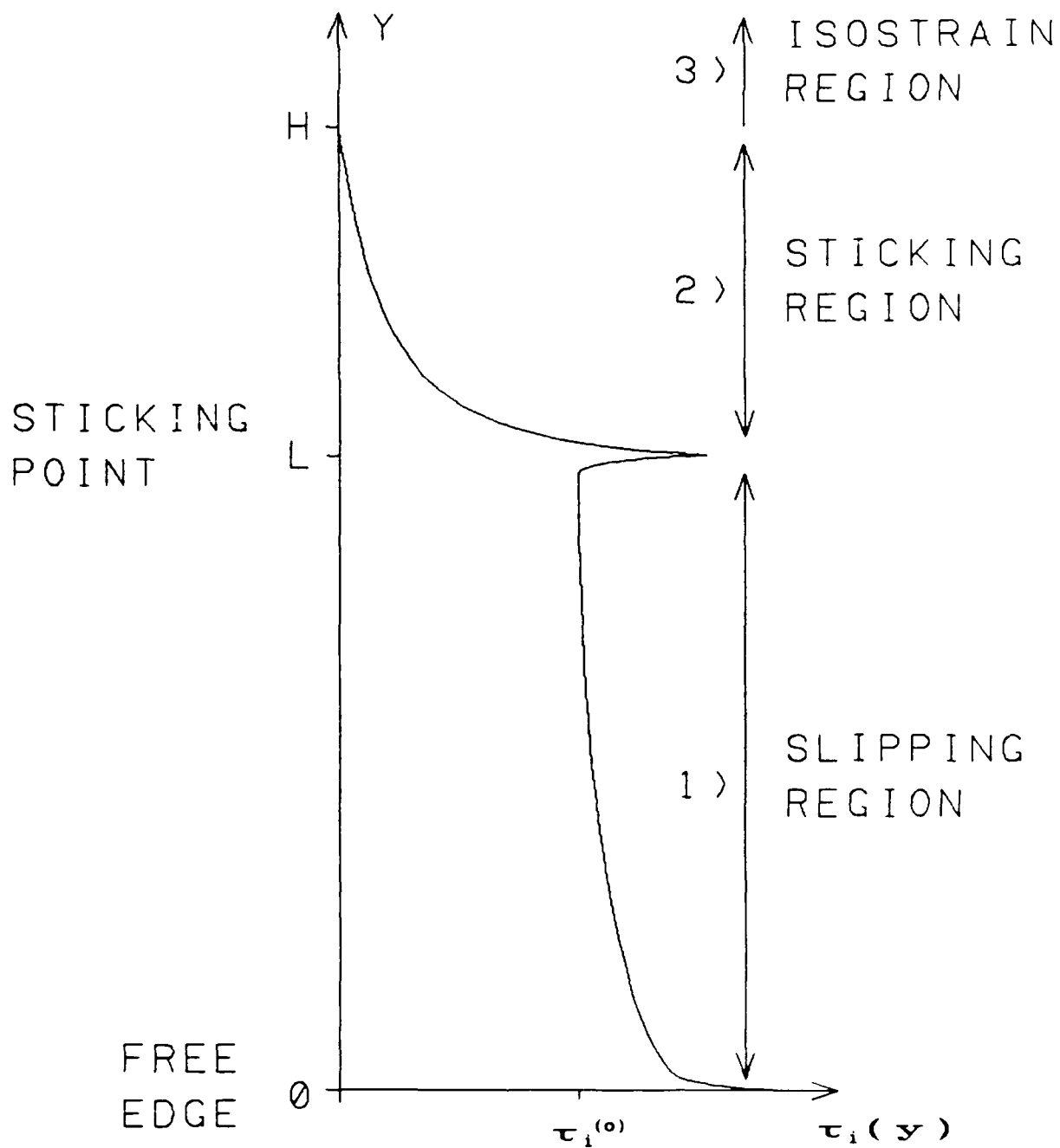
Figure 3.5. Idealized variation of the interfacial shear stress τ_i: slipping region (1), sticking region (2), sticking isostrain region (3), free edge singularity ($y = 0$) and mode II crack tip singularity ($y = L$).
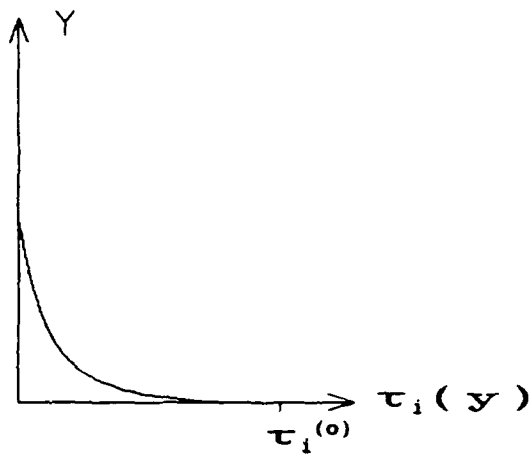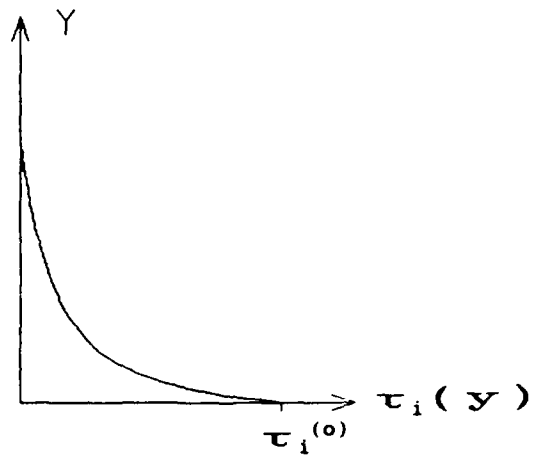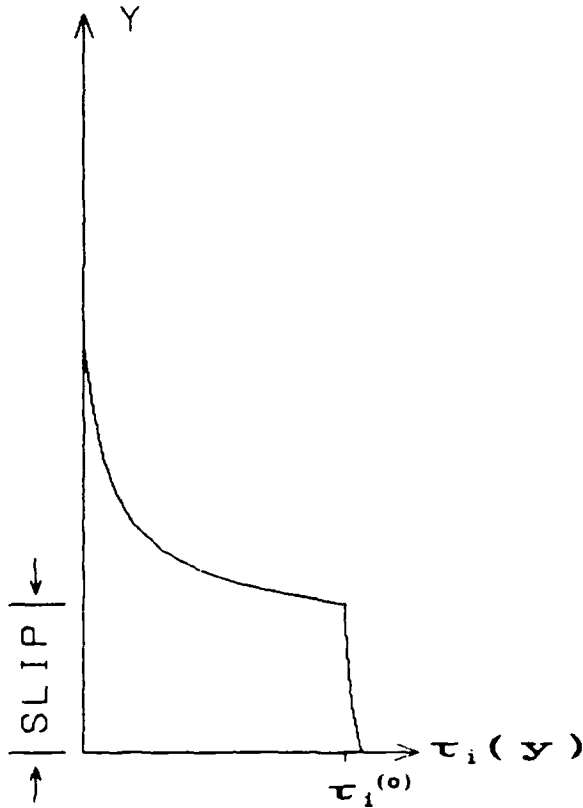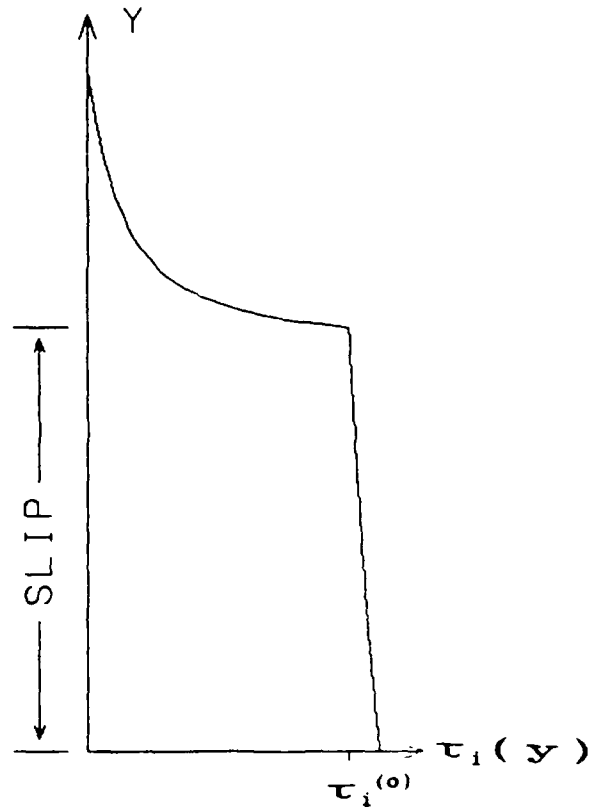
Figure 3.6. Interfacial shear stress τ_i variation during the idealized pullout process. As the pullout force is increased, the fiber sticks (a), critically sticks (b), and eventually slips (c).
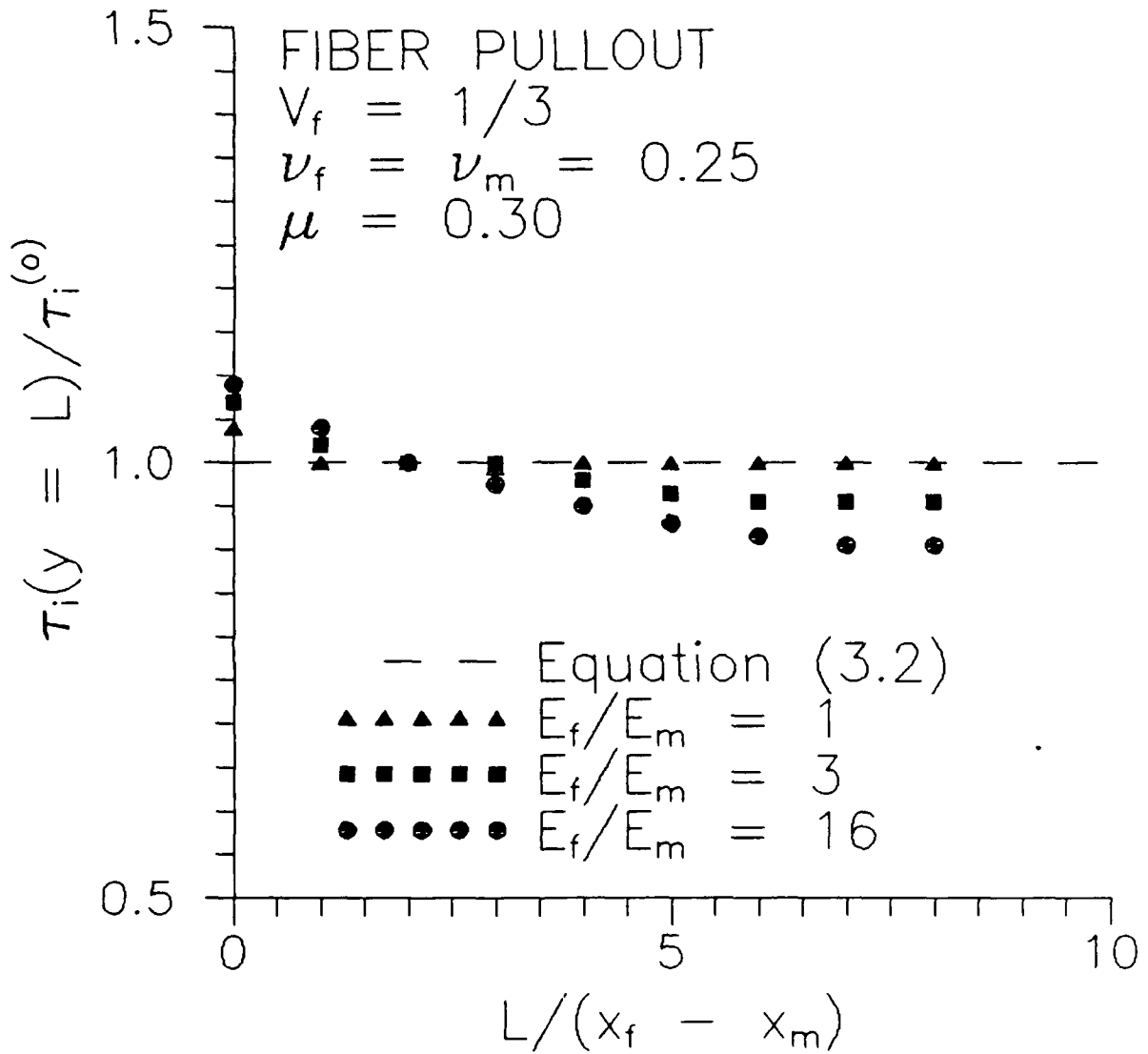
Figure 3.7. Comparison between the finite element pullout model results and Eq. (3.2). The interfacial shear stress at the sticking point $\tau_i(y = L)$ is approximately equal to the nominal interfacial shear stress $\tau_i^{(o)}$.
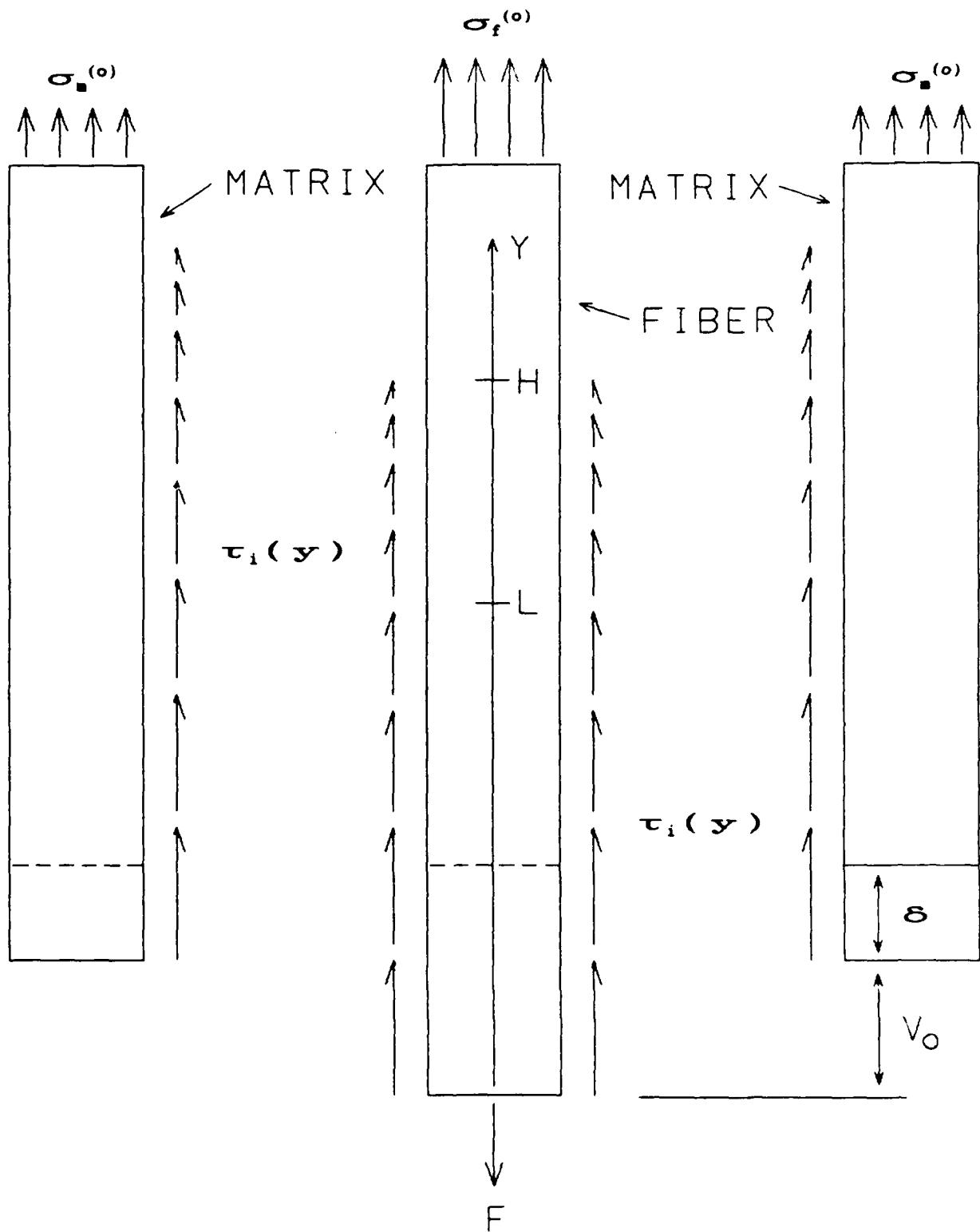
Figure 3.8. Idealized free body diagram of the steady-state pullout unit cell.
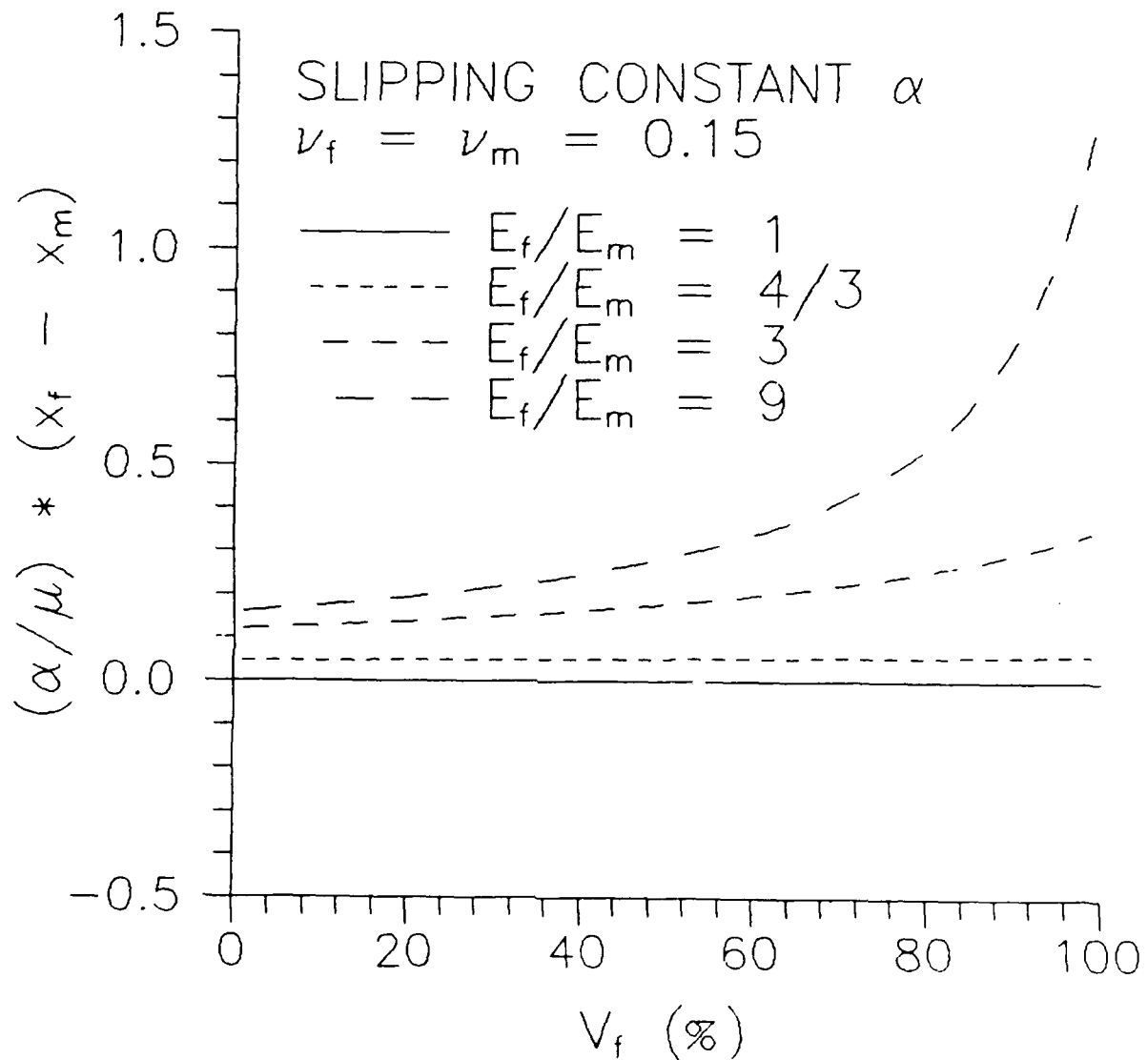
Figure 3.9a. Variation of slipping constant α with volume fraction and relative fiber/matrix stiffness when $\nu_f = \nu_m = 0.15$.
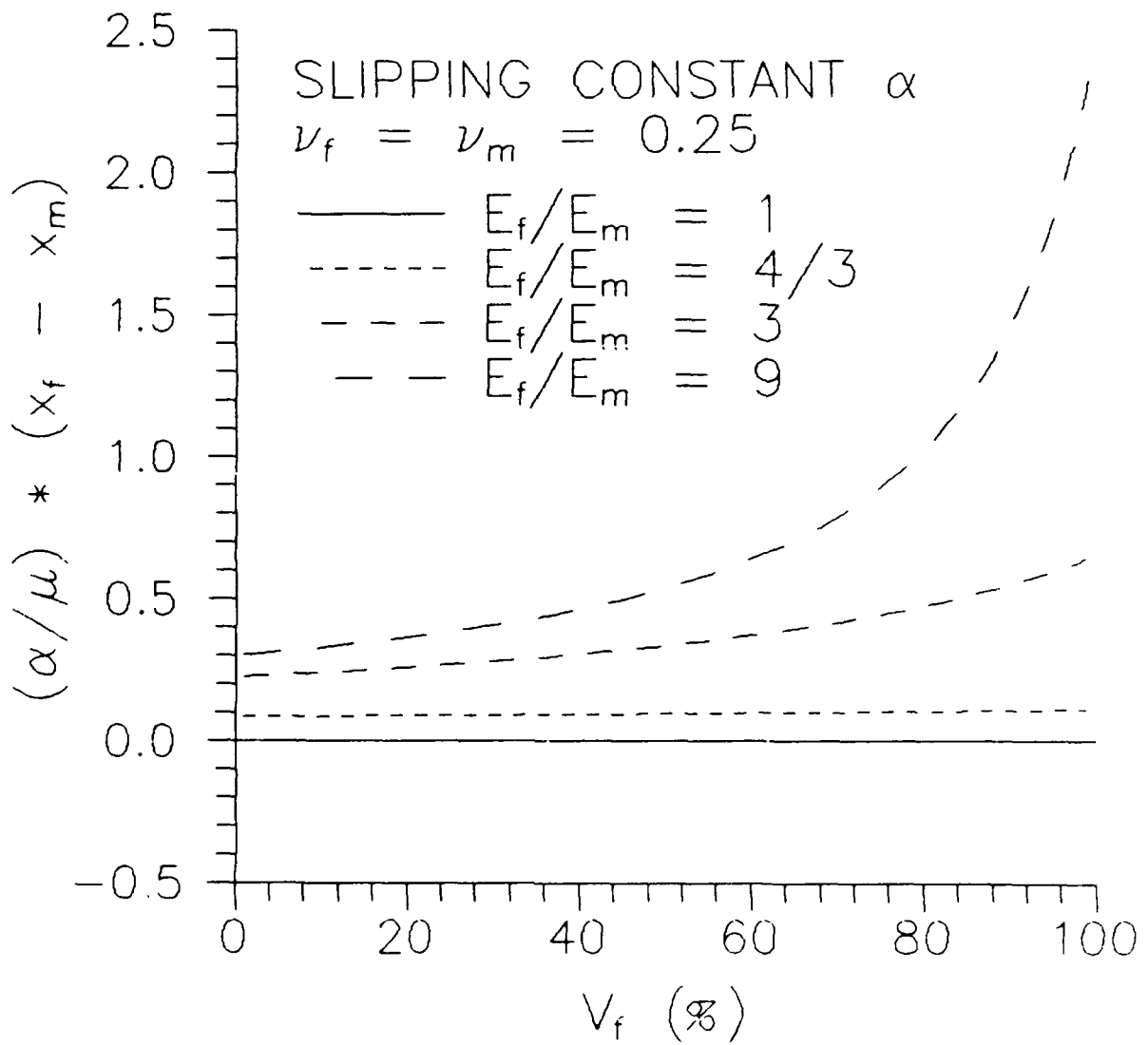
Figure 3.9b. Variation of slipping constant a with volume fraction and relative fiber/matrix stiffness when $\nu_f = \nu_m = 0.25$.
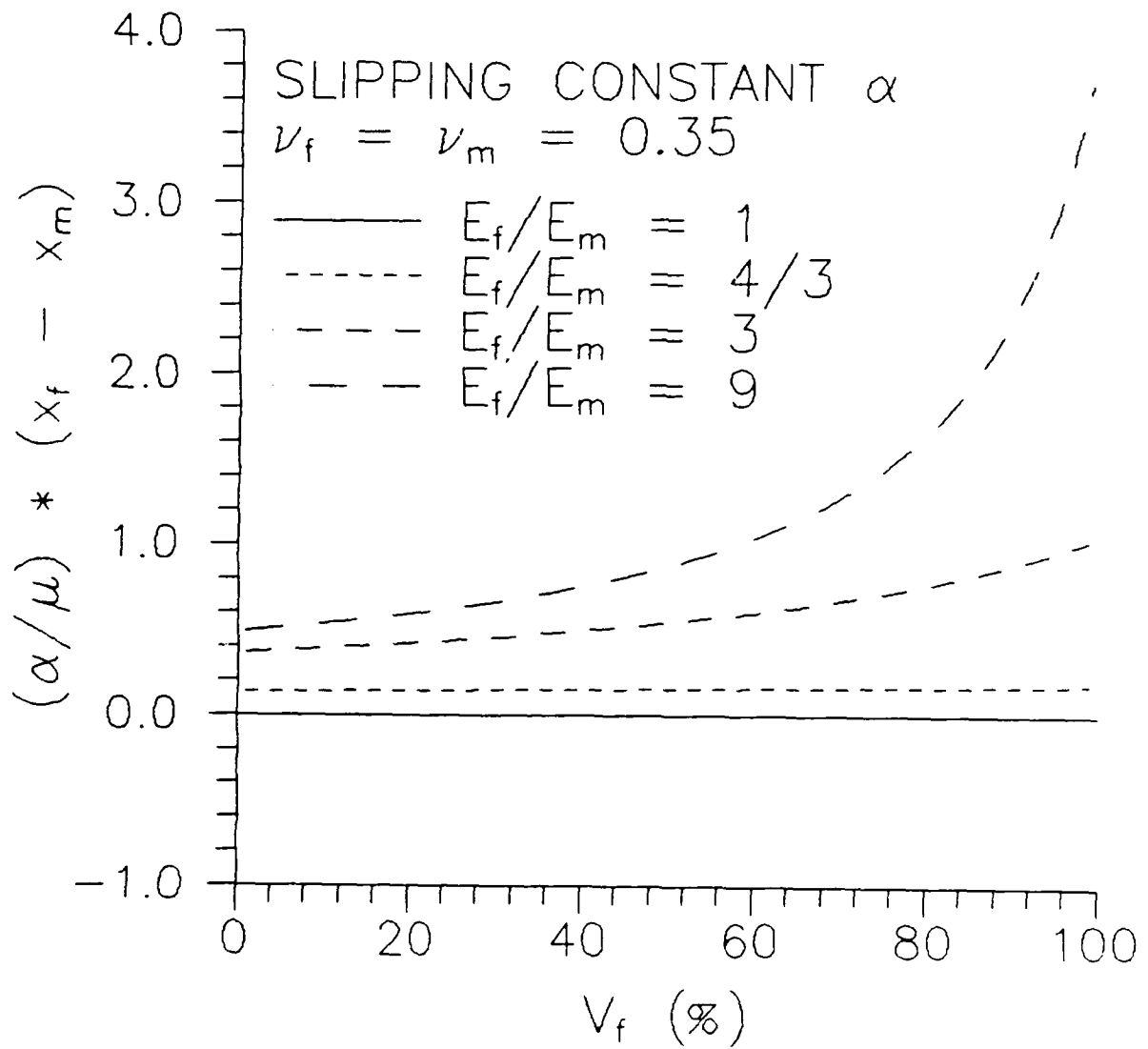
Figure 3.9c. Variation of slipping constant α with volume fraction and relative fiber/matrix stiffness when $\nu_f = \nu_m = 0.35$.
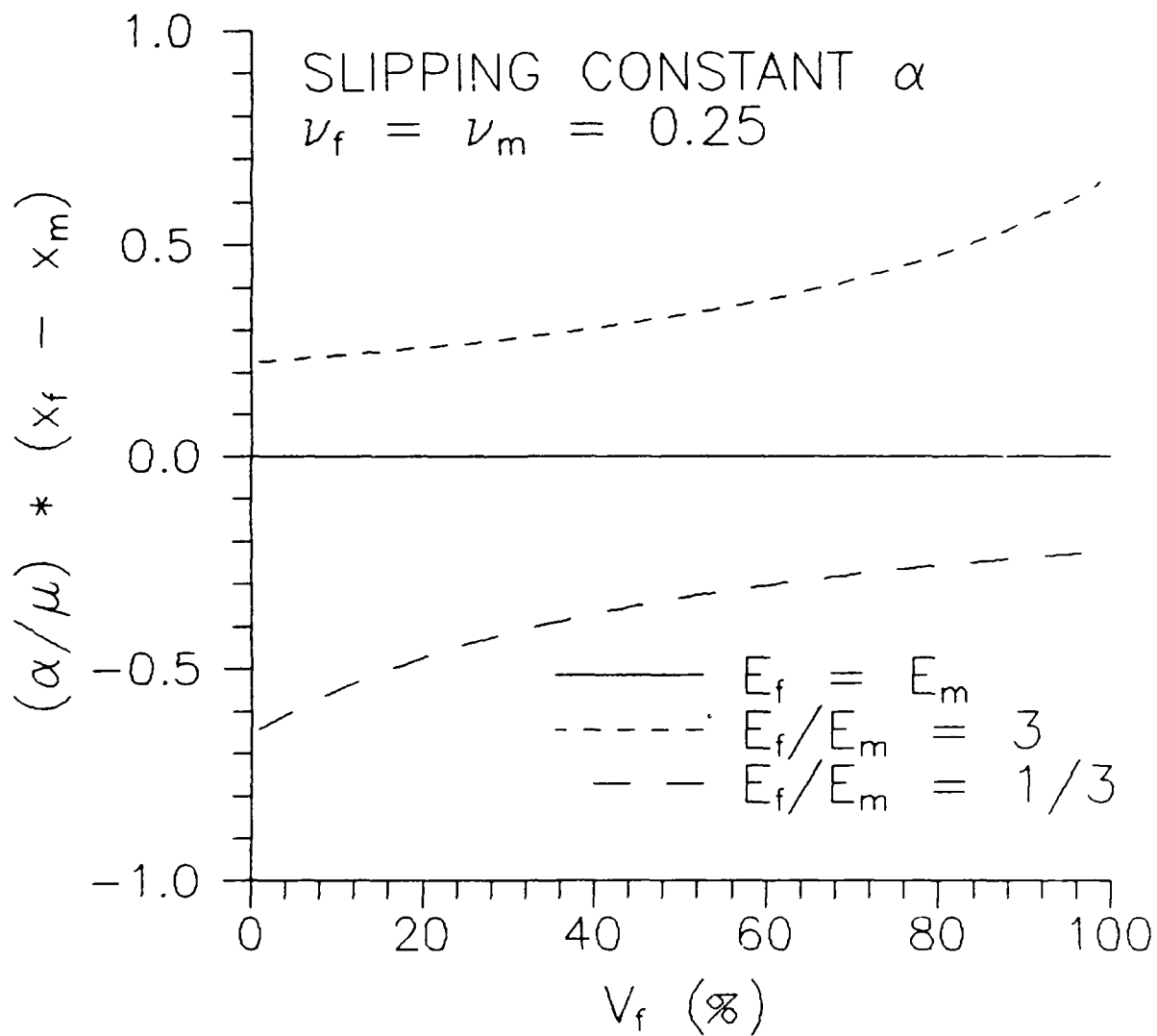
Figure 3.10. Variation of slipping constant α with volume fraction for $E_f/E_m = 3$ and $E_f/E_m = 1/3$ showing the antisymmetry of α with respect to $E_f/E_m = 1$ and $V_f = 50\%$.
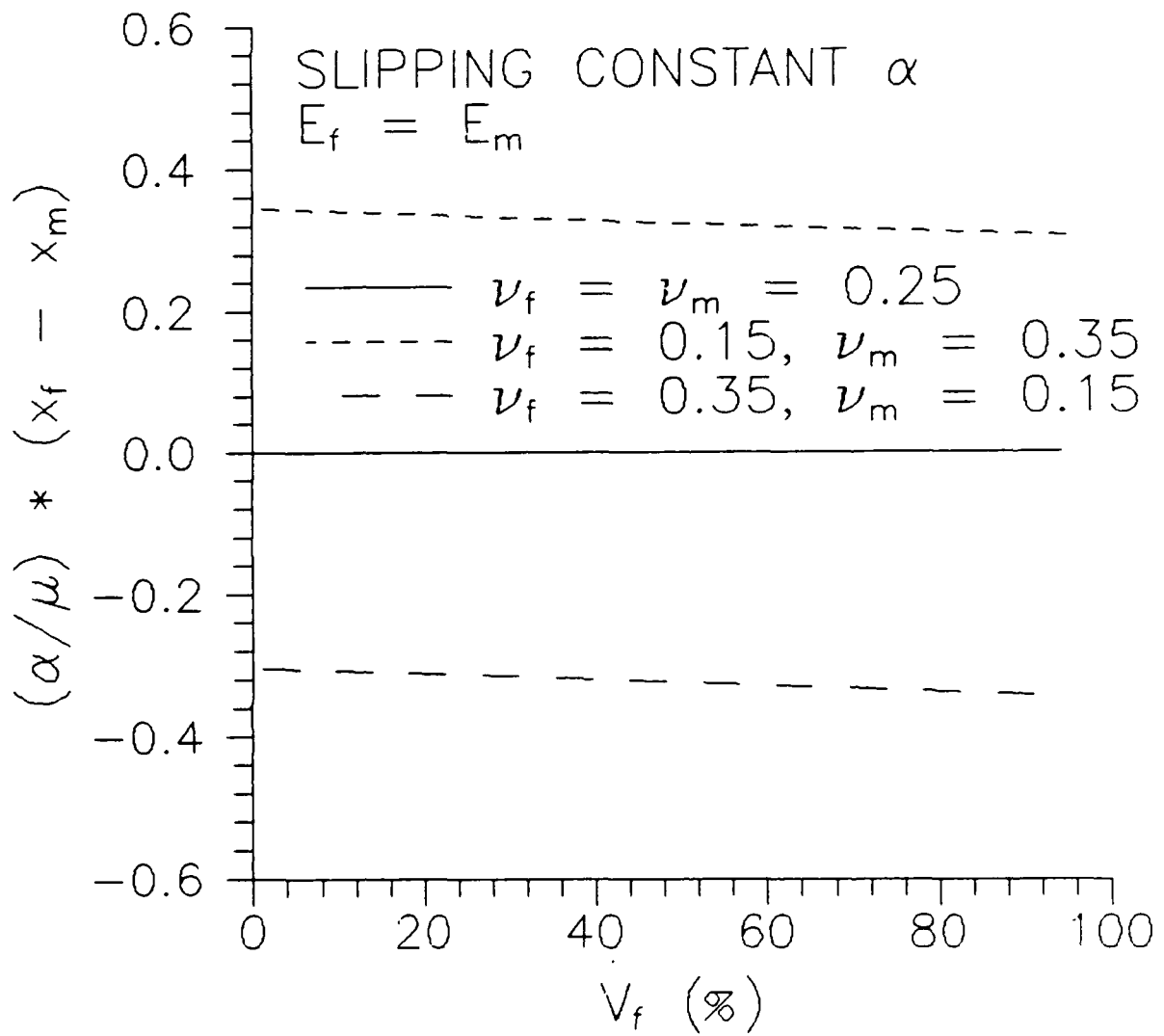
Figure 3.11. Variation of slipping constant a with volume fraction and ν when E_f/E_m = 1.
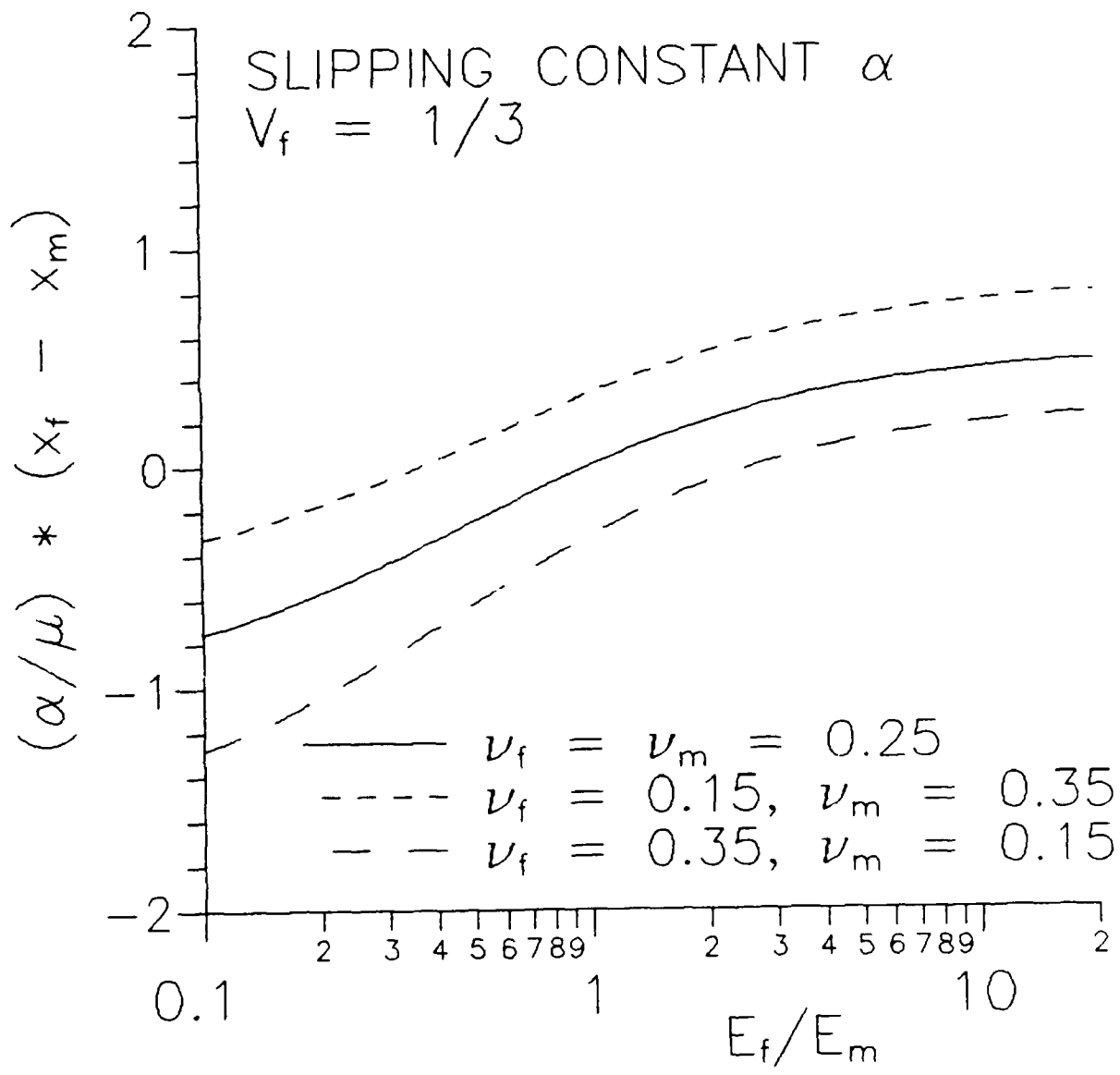
Figure 3.12. Variation of slipping constant a with material properties when V_f = 1/3.
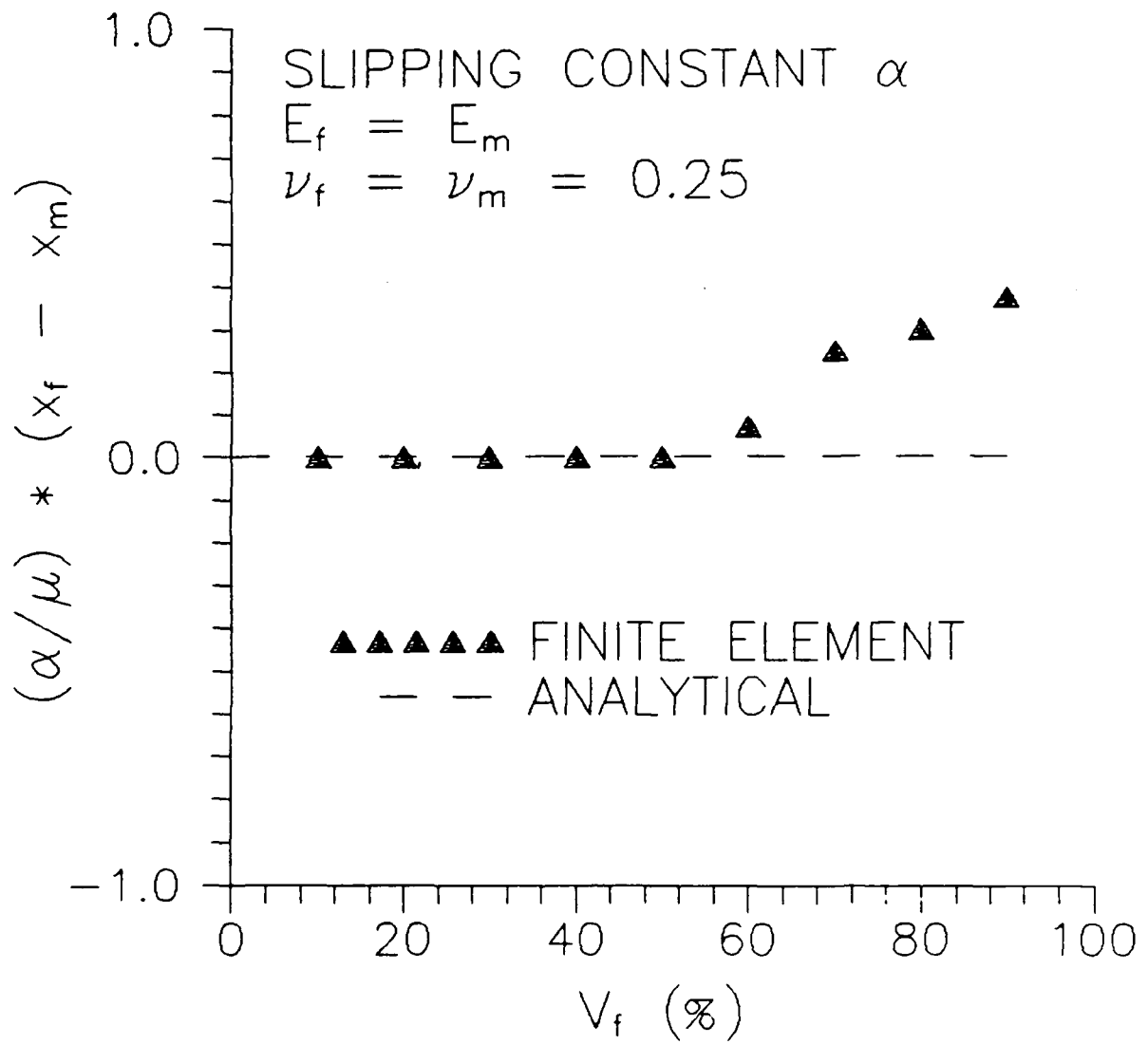
Figure 3.13a. Comparison of finite element predictions for α with the analytical solution when $E_f/E_m = 1$ and $\nu_f = \nu_m = 0.25$.
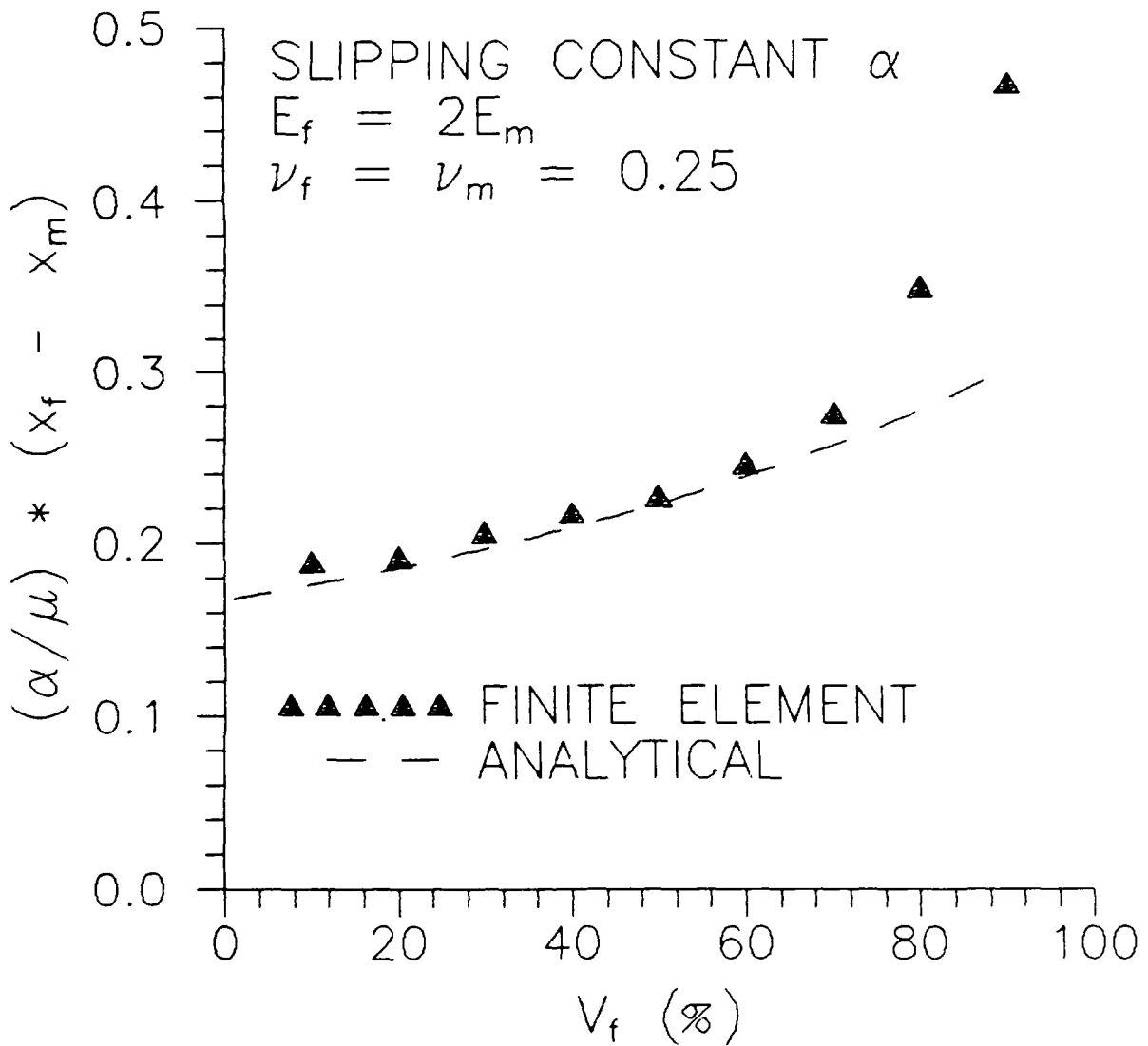
Figure 3.13b. Comparison of finite element predictions for α with the analytical solution when $E_f/E_m = 2$ and $\nu_f = \nu_m = 0.25$.

86
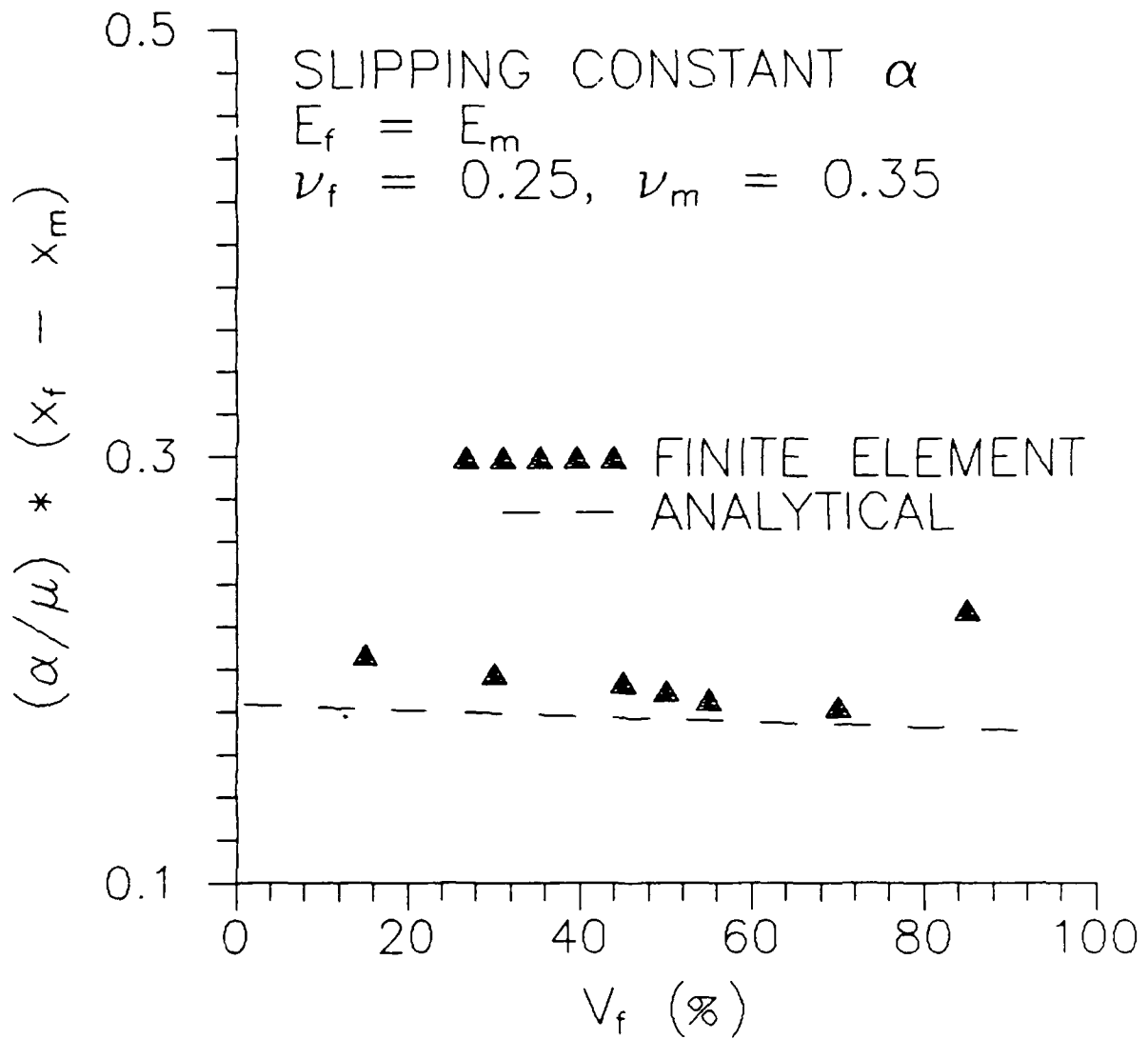
Figure 3.13c. Comparison of finite element predictions for α with the analytical solution for $E_f/E_m = 1$ and $\nu_f - \nu_m = -0.10$.
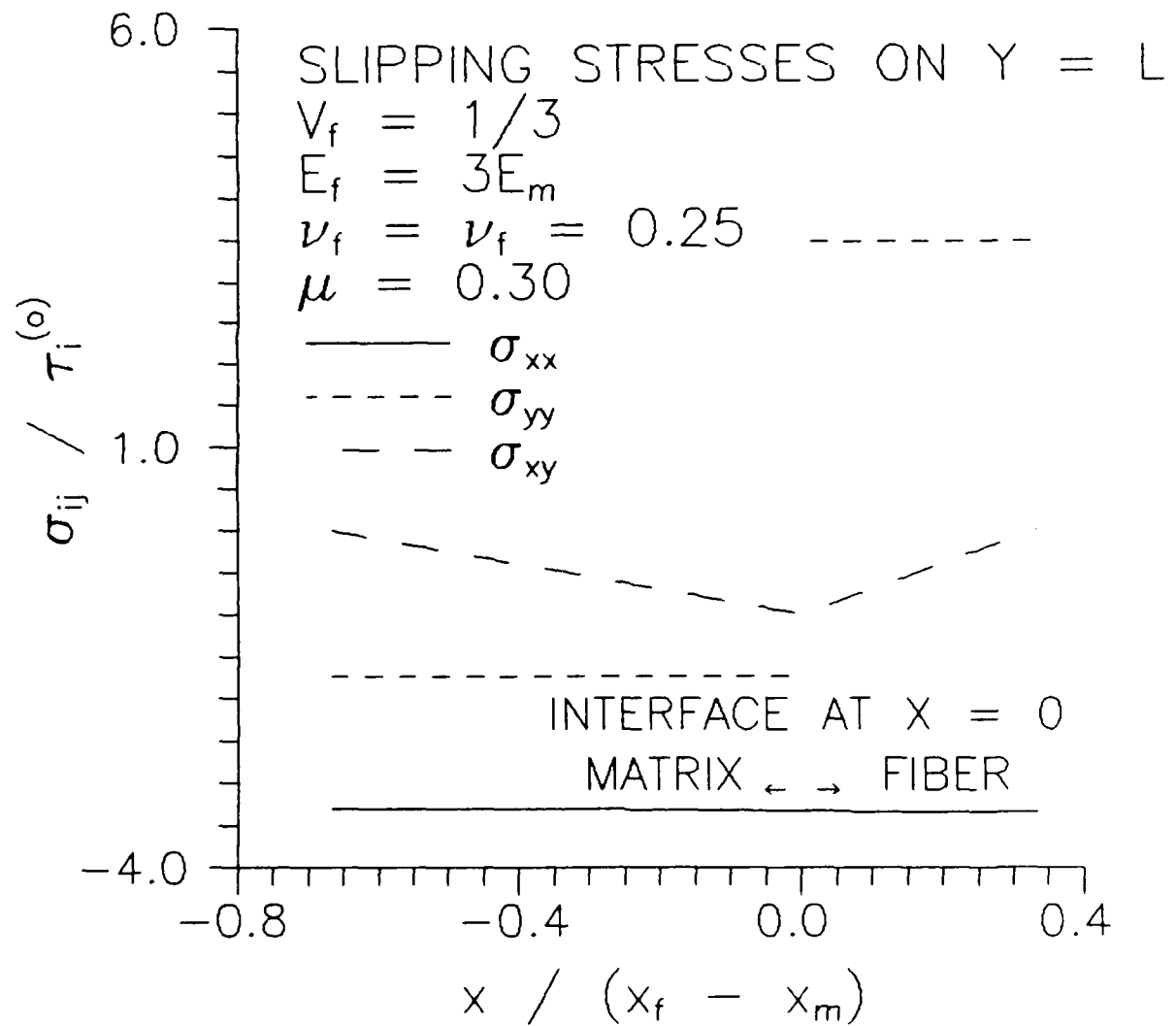
Figure 3.14a. Variation of stresses with x in the slipping region along y = L.
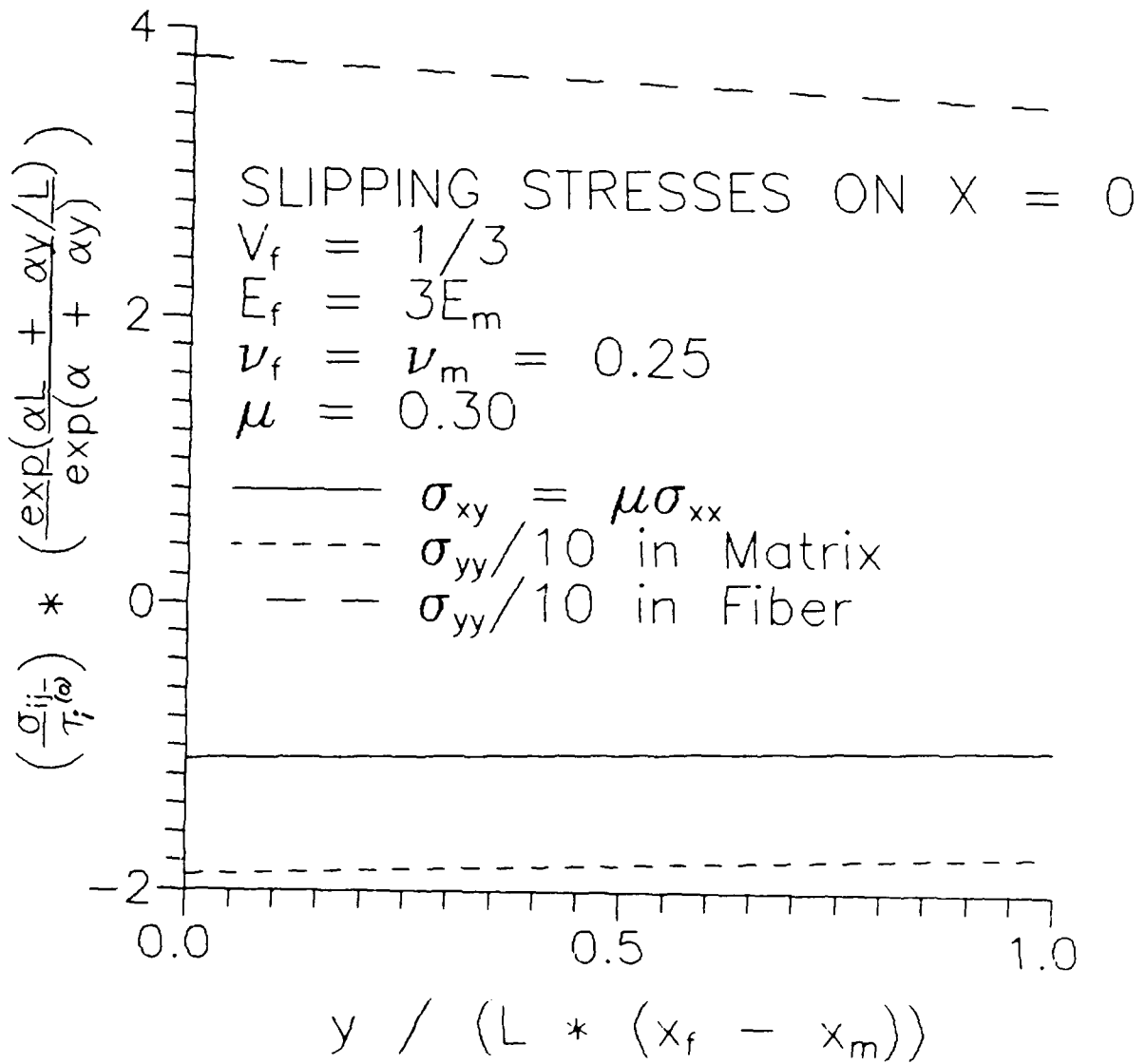
Figure 3.14b. Variation of stresses with y in the slipping region along the interface x = 0.
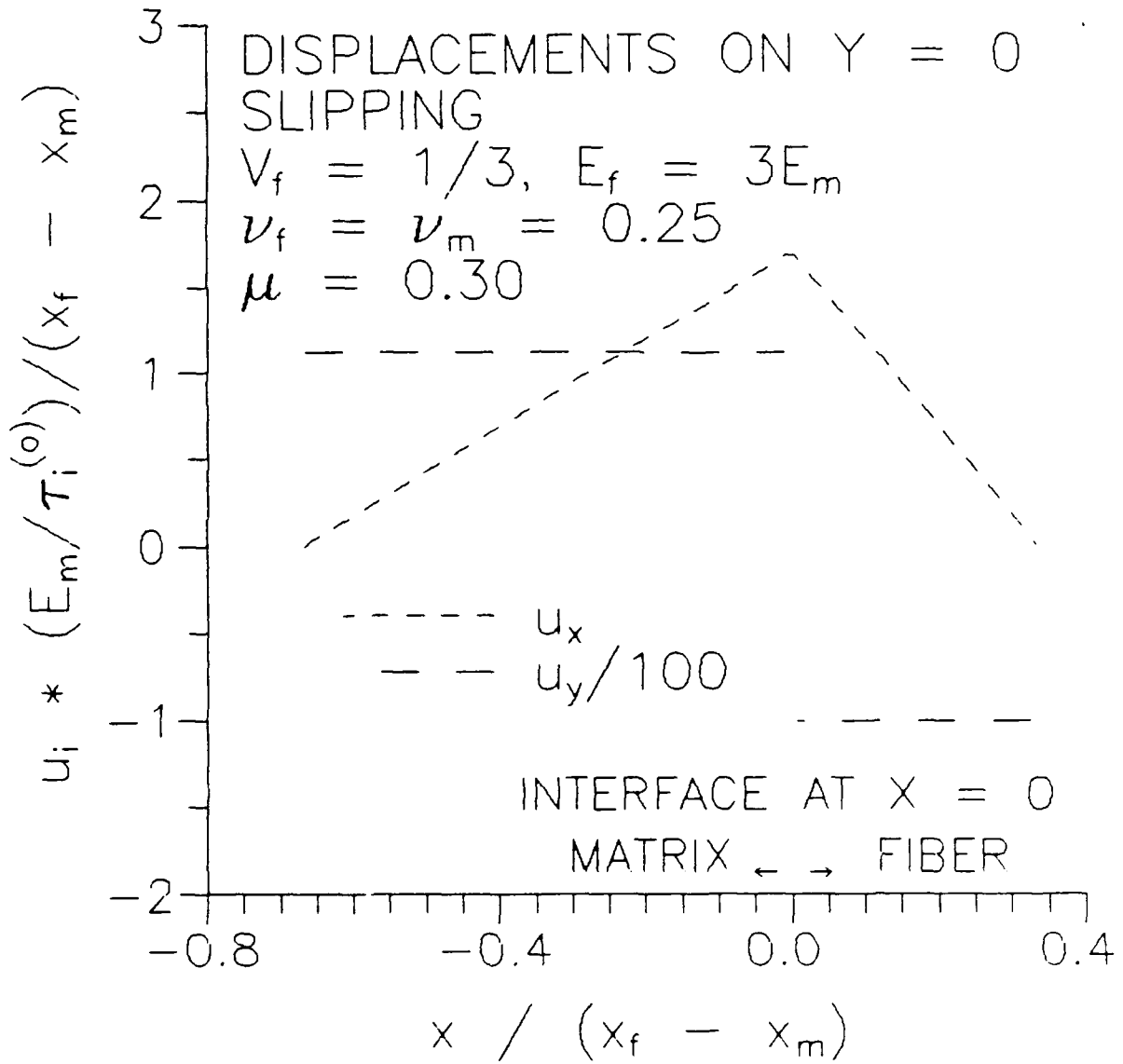
Figure 3.14c. Variation of displacements with x in the slipping region along y = 0.

90
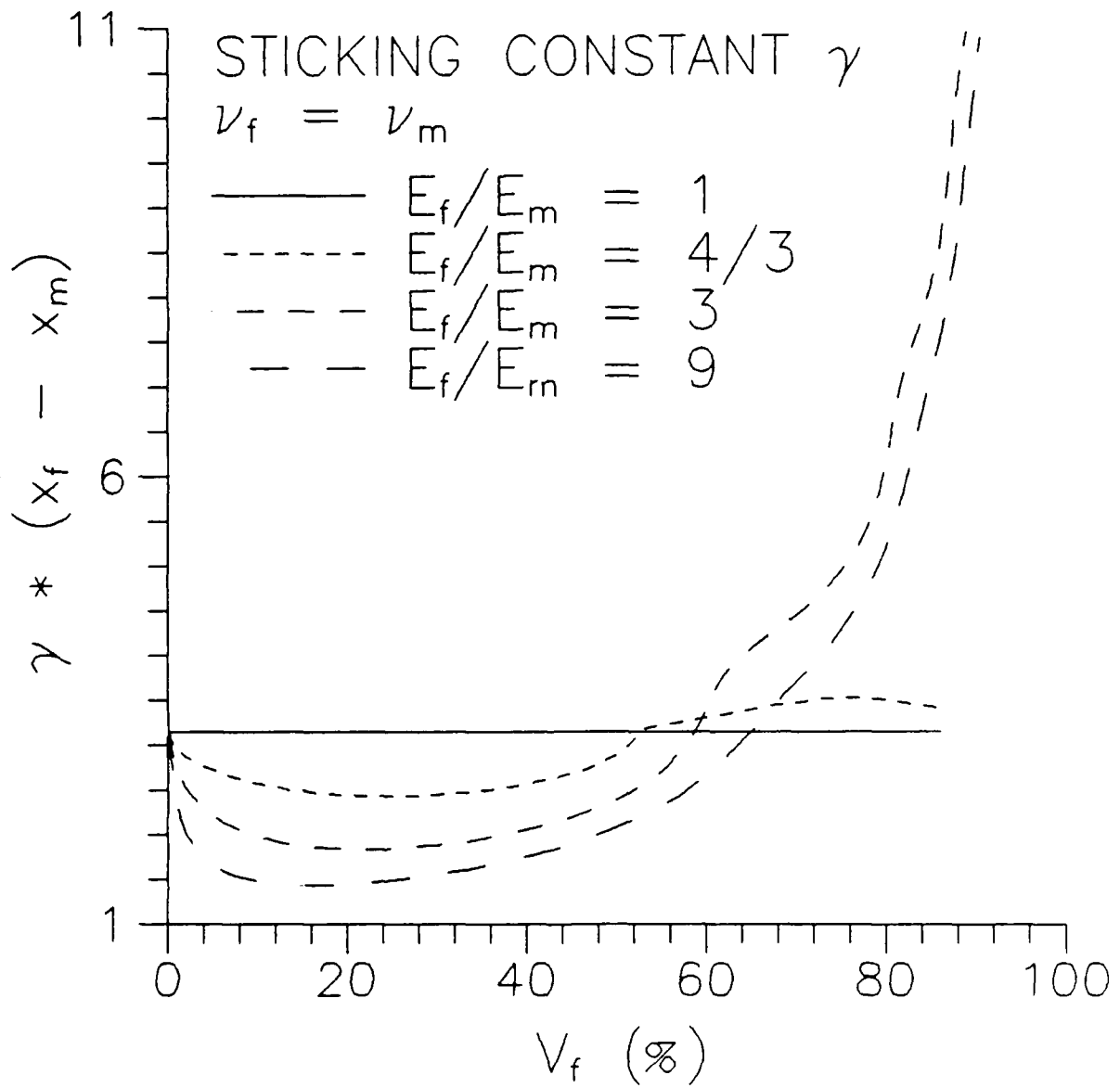
Figure 3.15. Variation of sticking constant γ with volume fraction and relative fiber/matrix stiffness when $\nu_f = \nu_m$.
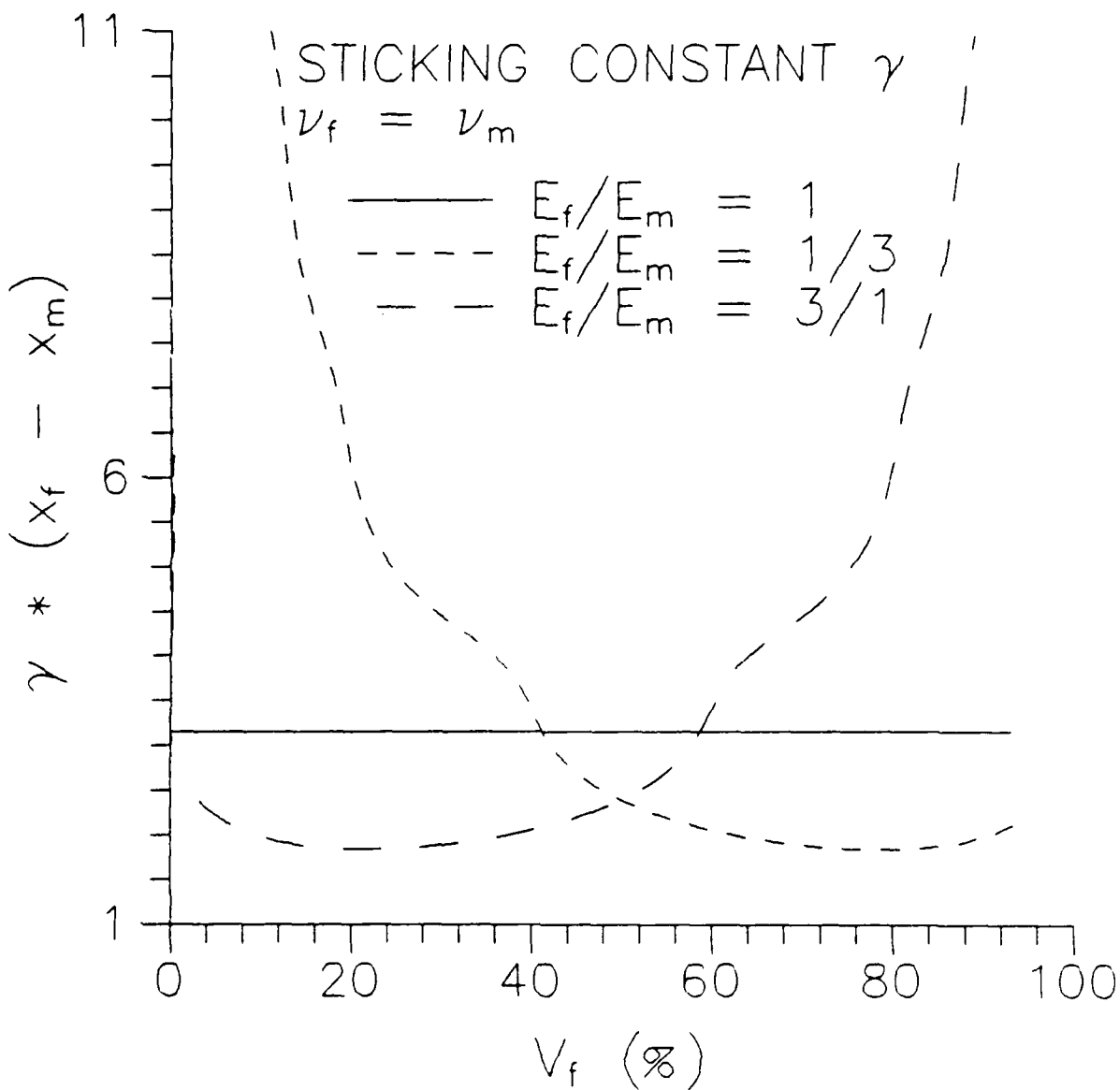
Figure 3.16. Variation of sticking constant γ with volume fraction for $E_f/E_m = 3$ and 1/3 showing the symmetry of γ with respect to $E_f/E_m = 1$ and $V_f = 50\%$.
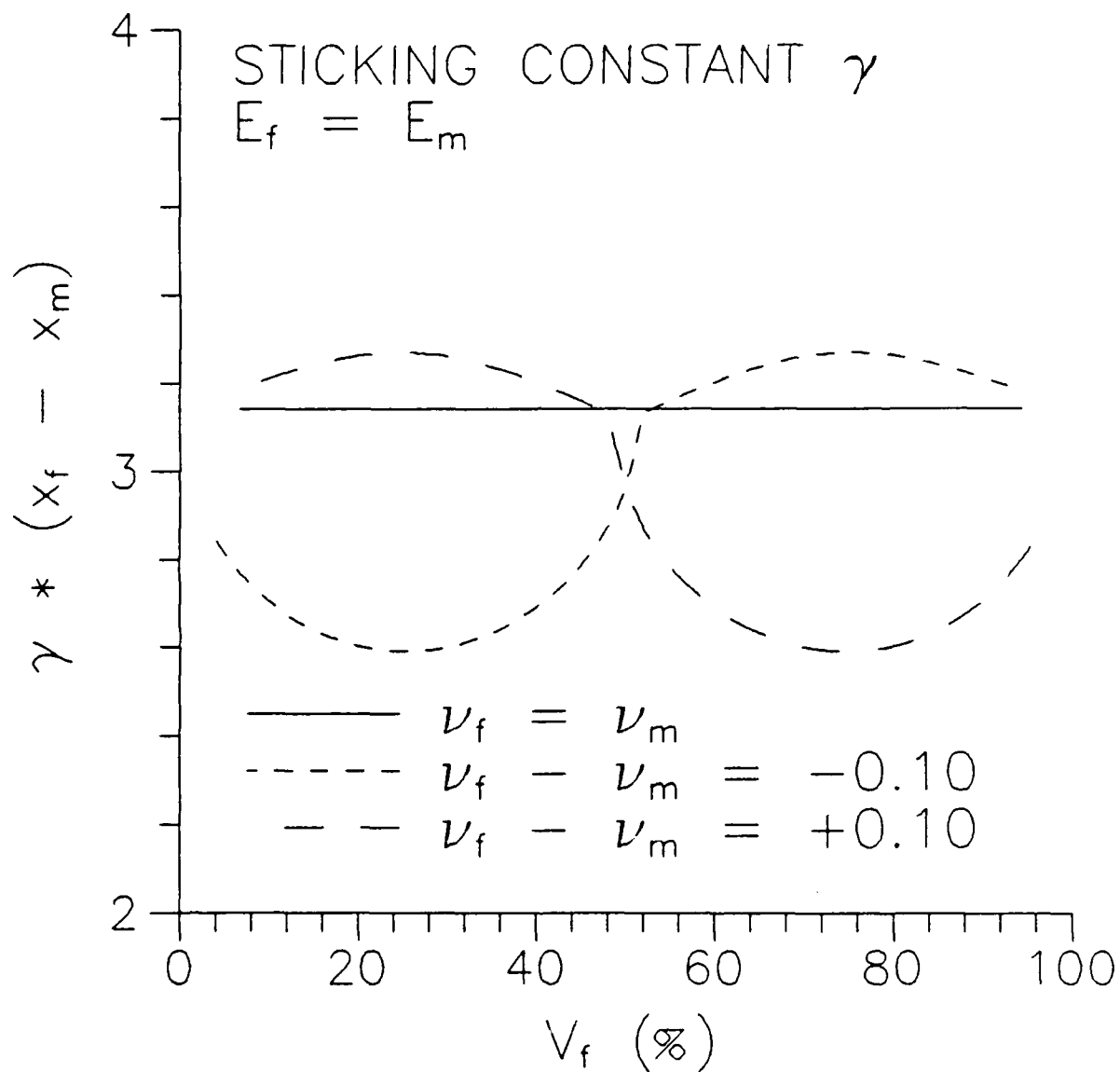
Figure 3.17. Variation of sticking constant γ with volume fraction and γ when $E_f/E_m = 1$.
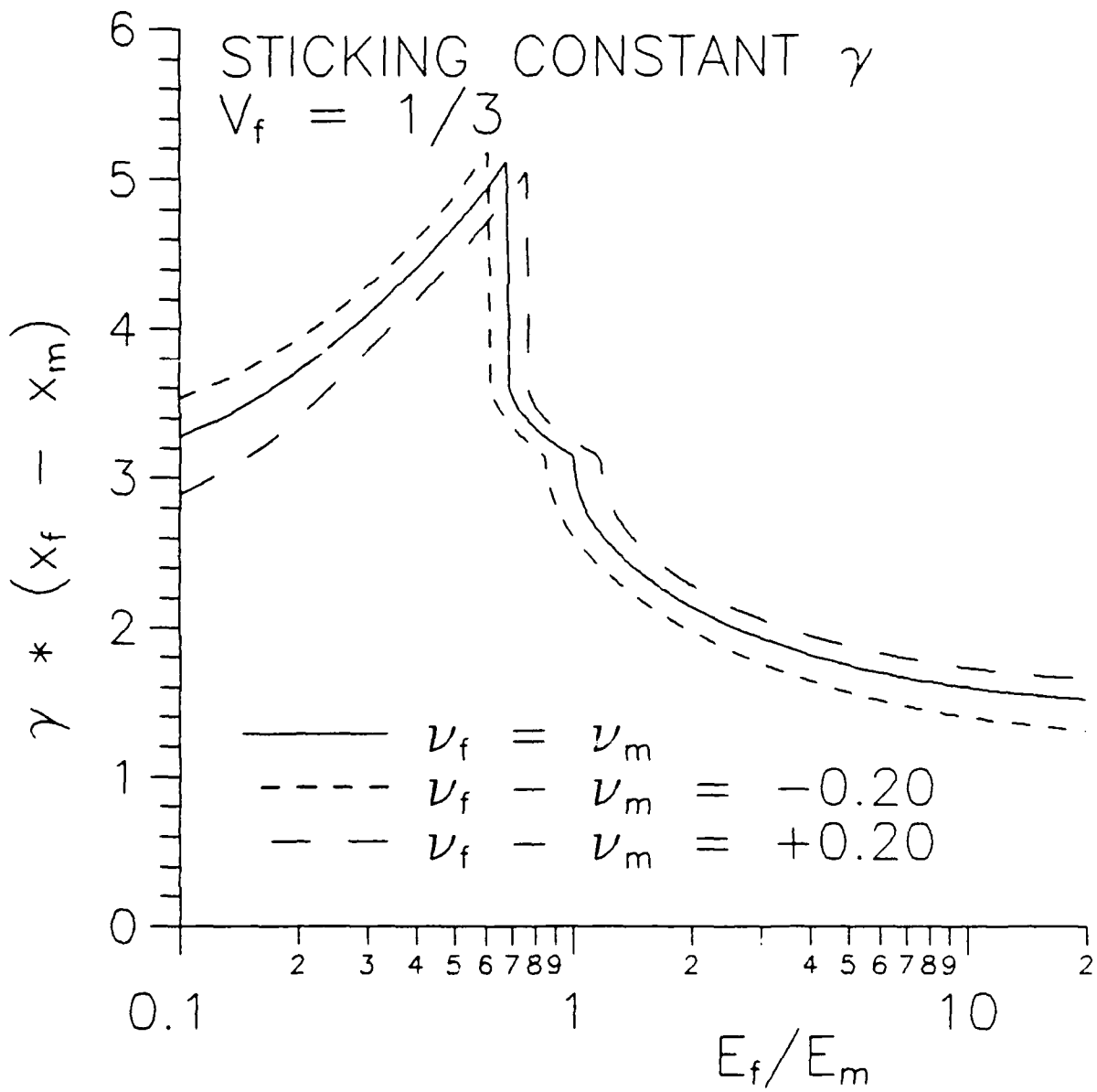
Figure 3.18. Variation of sticking constant γ with material properties when $V_f = 1/3$.
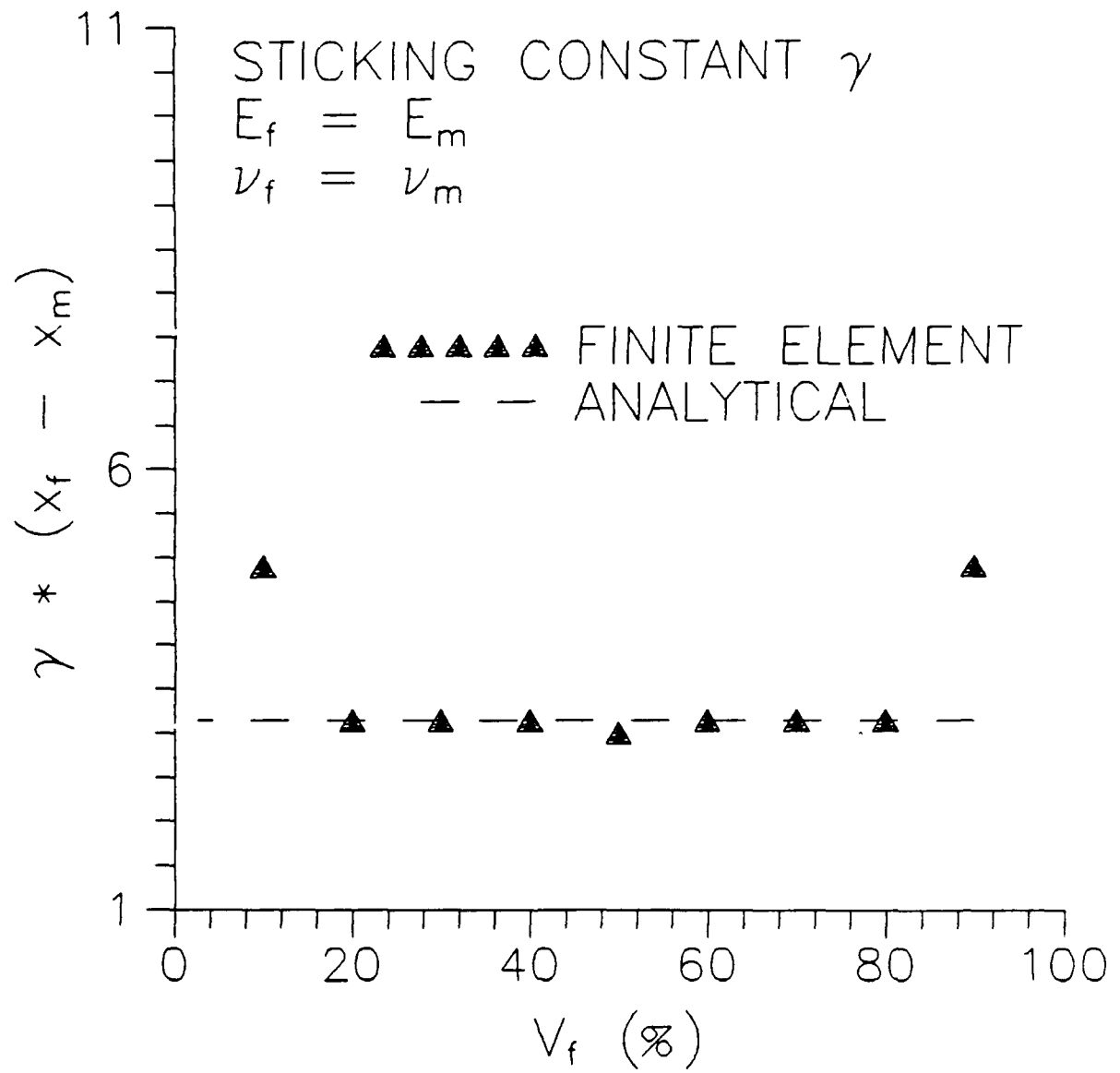
Figure 3.19a. Comparison of finite element predictions for γ with the analytical solution when $E_f/E_m = 1$ and $\nu_f = \nu_m$.
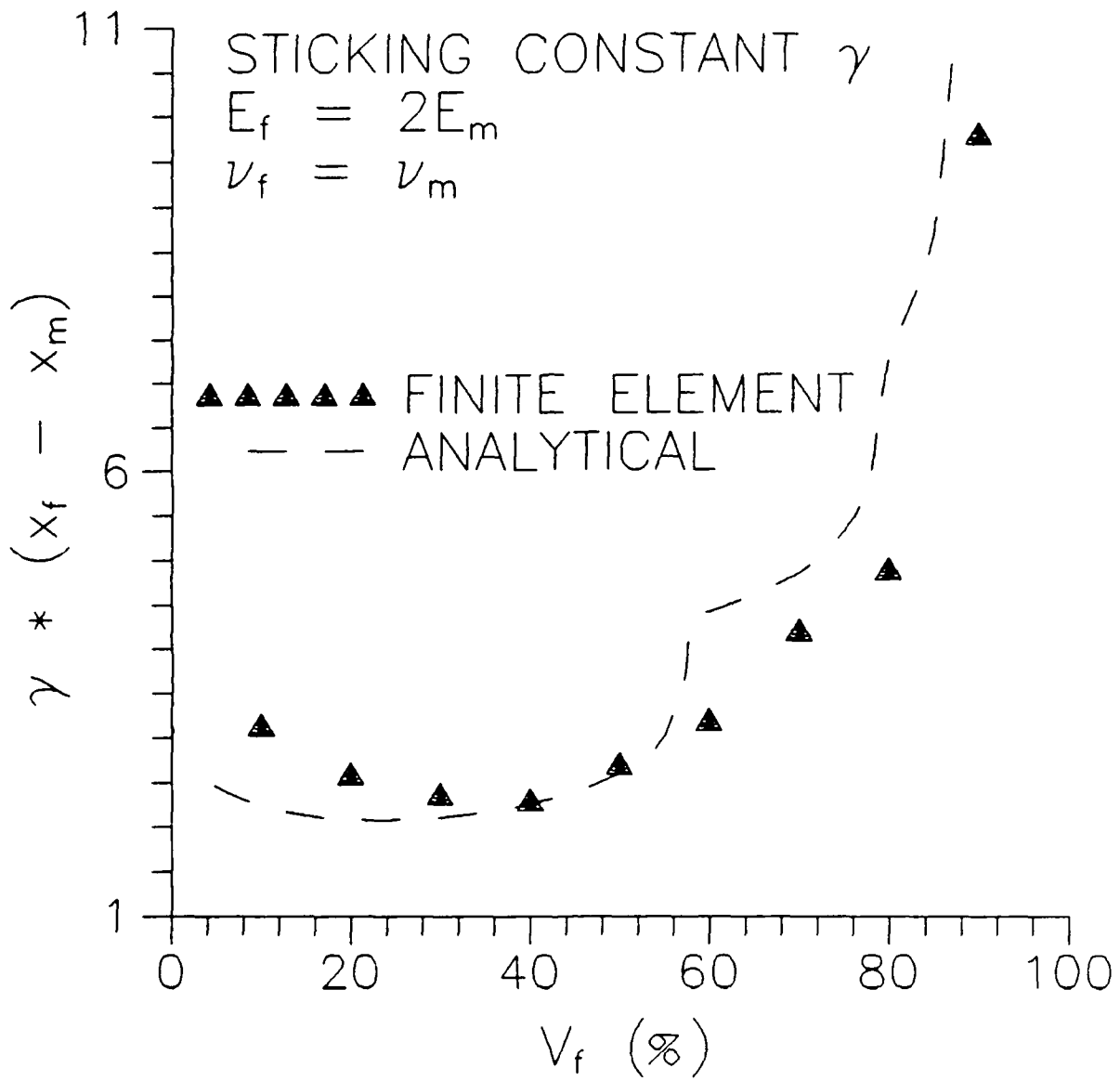
Figure 3.19b. Comparison of finite element predictions for γ with the analytical solution when $E_f/E_m = 2$ and $\nu_f = \nu_m$.
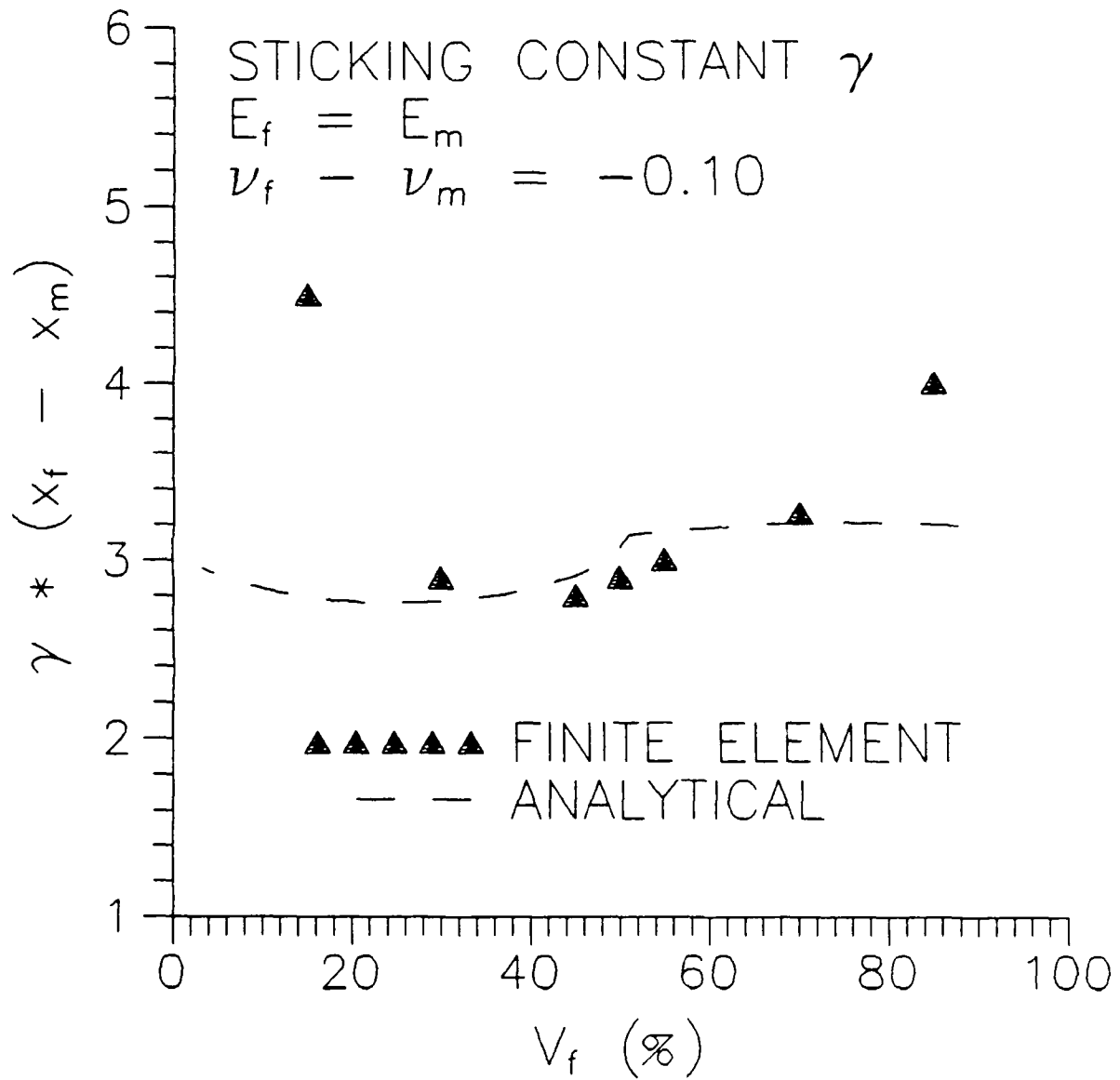
Figure 3.19c. Comparison of finite element predictions for γ with the analytical solution when $E_f/E_m = 1$ and $\nu_f - \nu_m = -0.10$.
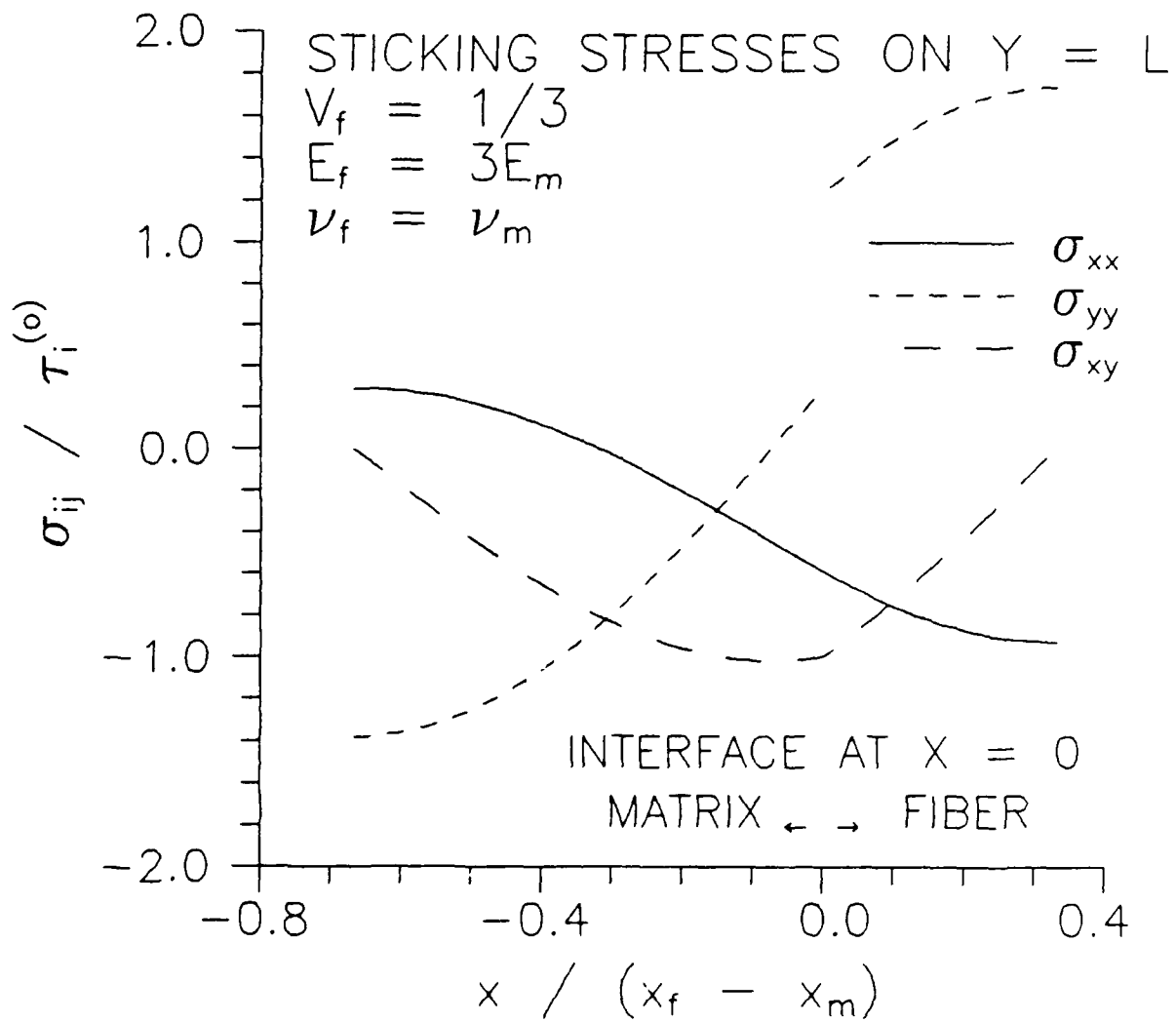
Figure 3.20a. Variation of stresses with x in the sticking region along y = L.
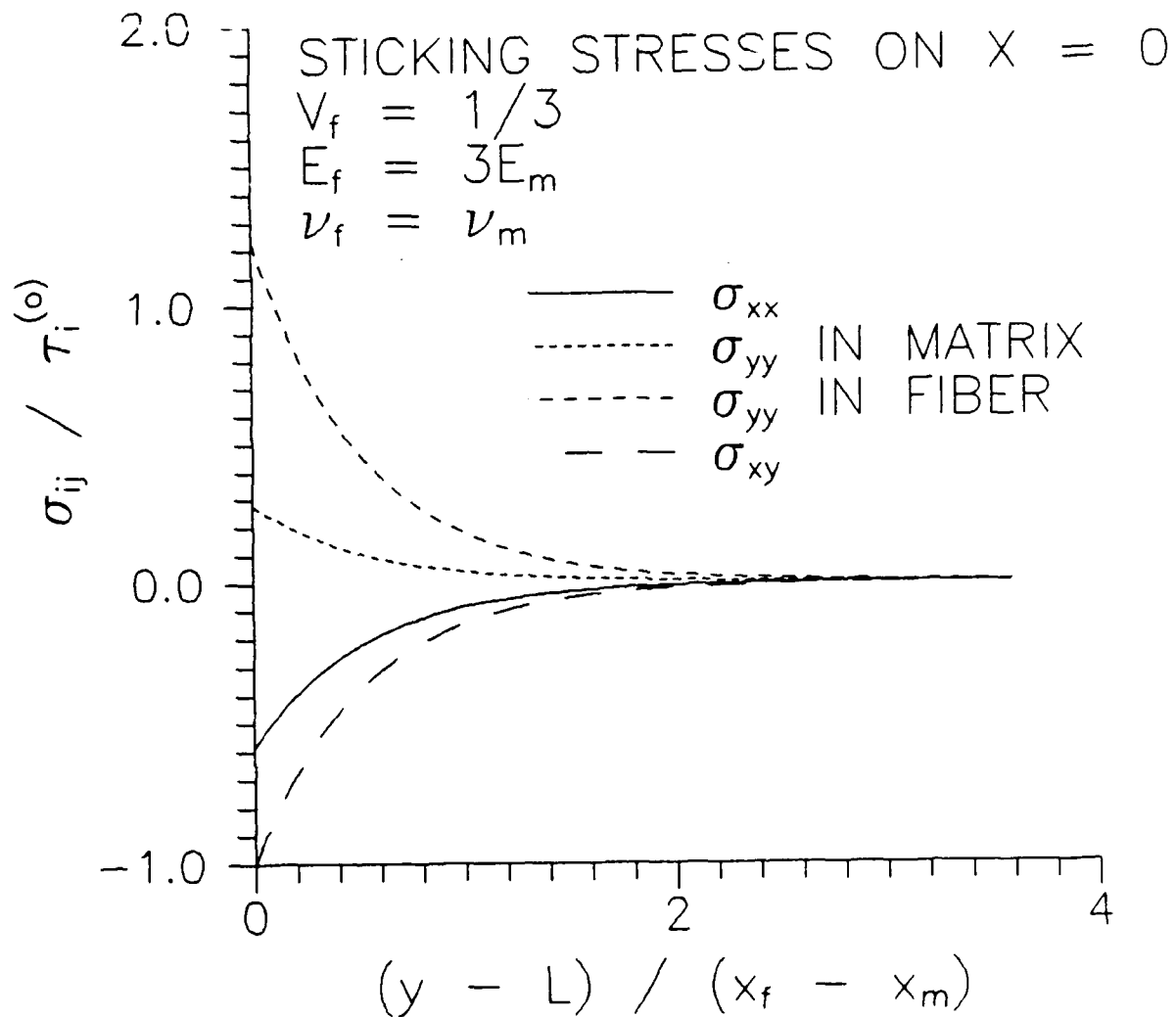
Figure 3.20b. Variation of stresses with y in the sticking region along the interface x = 0.
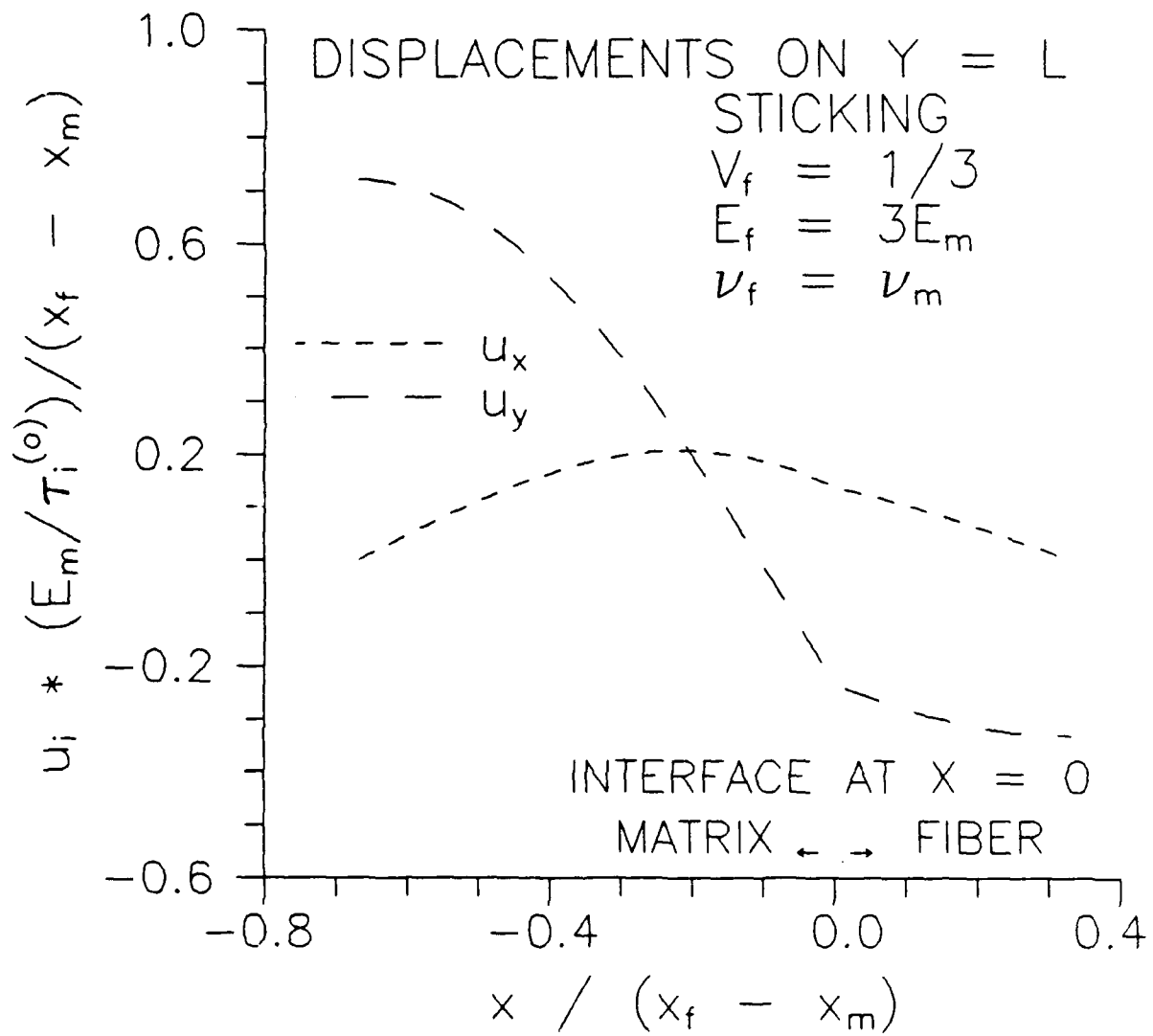
Figure 3.20c. Variation of displacements with x in the sticking region along y = L.
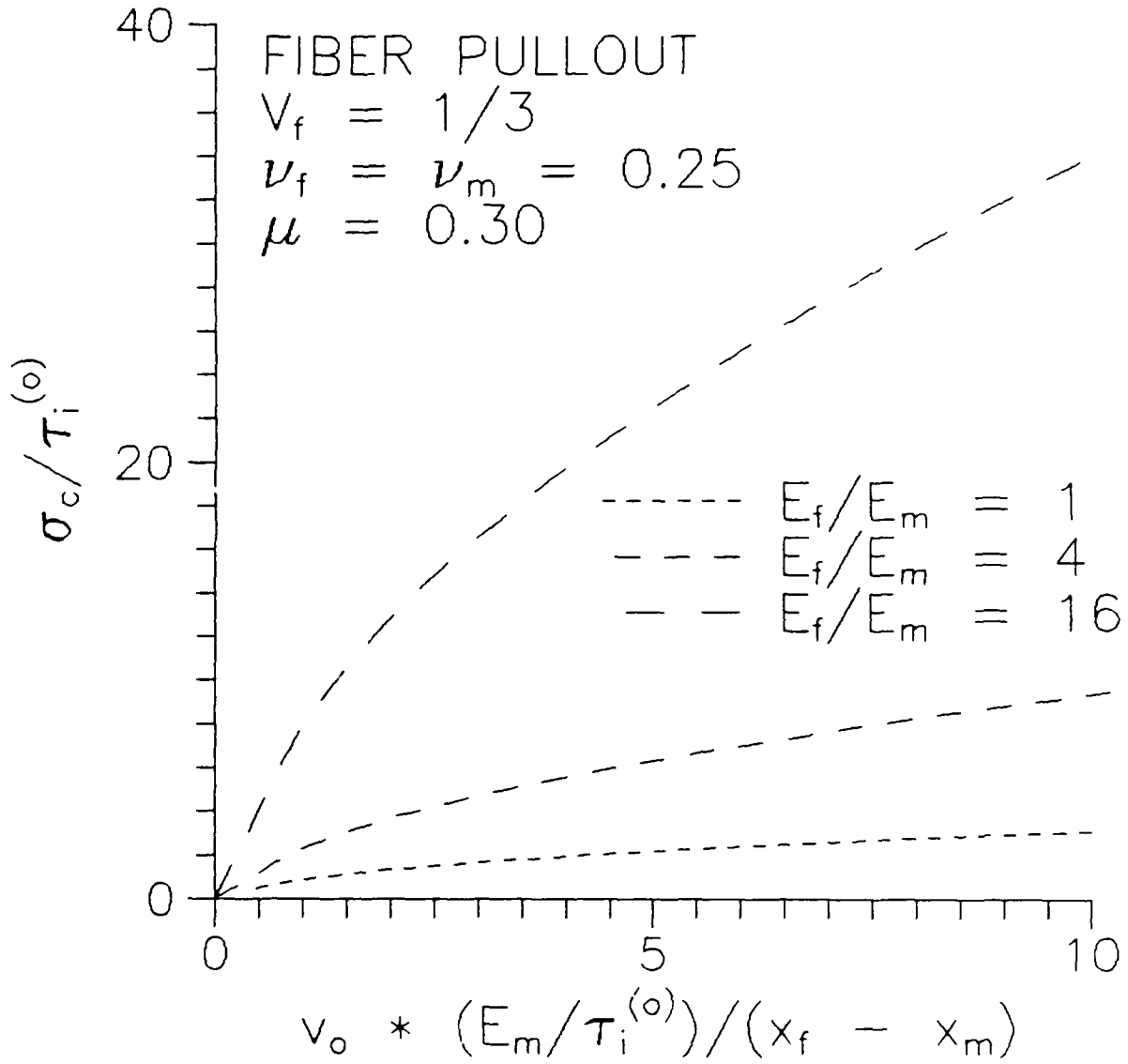
Figure 3.21a. Effect of stiffness ratio E_f/E_m on predicted fiber pullout response.
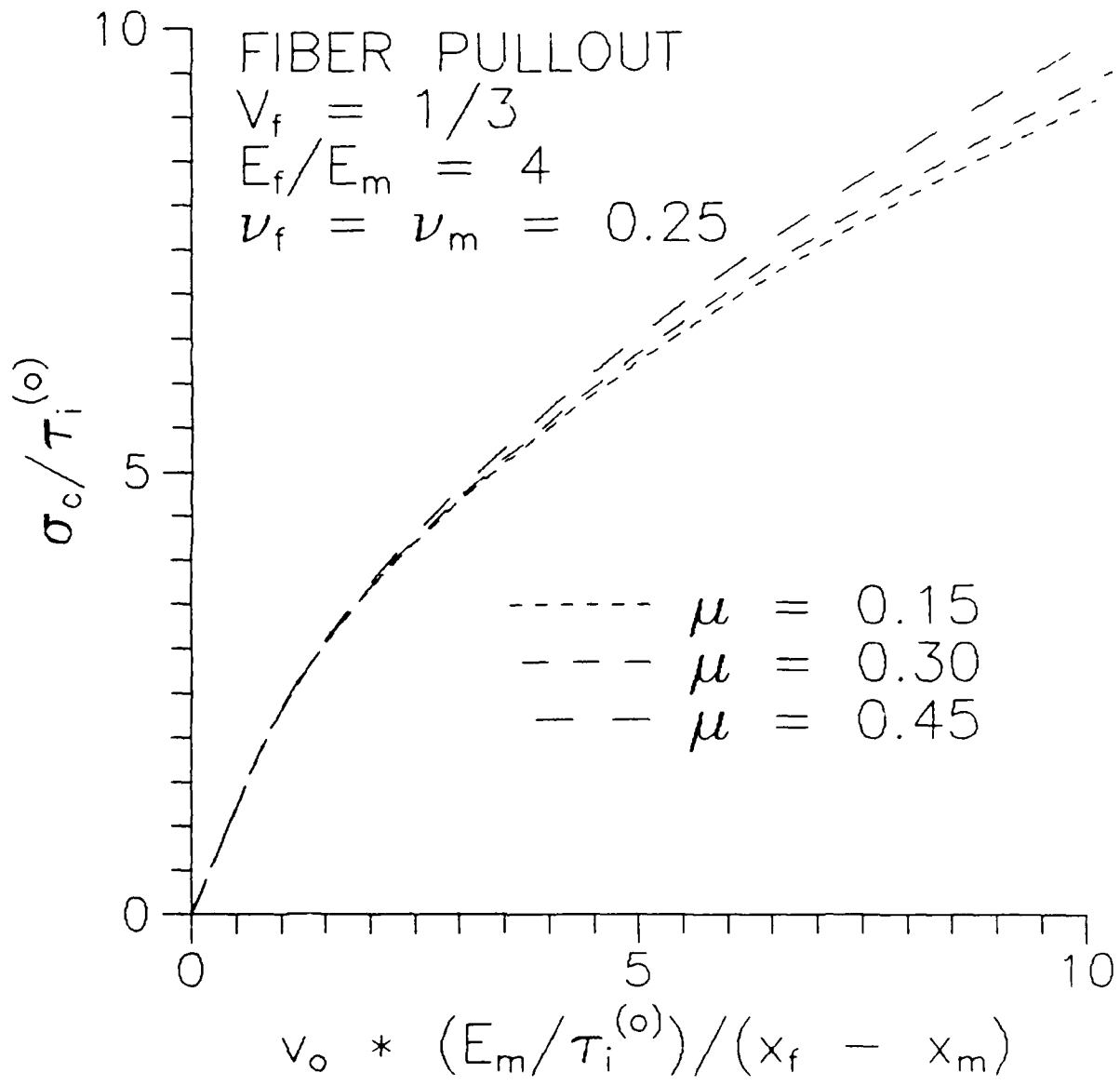
Figure 3.21b. Effect of friction coefficient μ on predicted fiber pullout response.
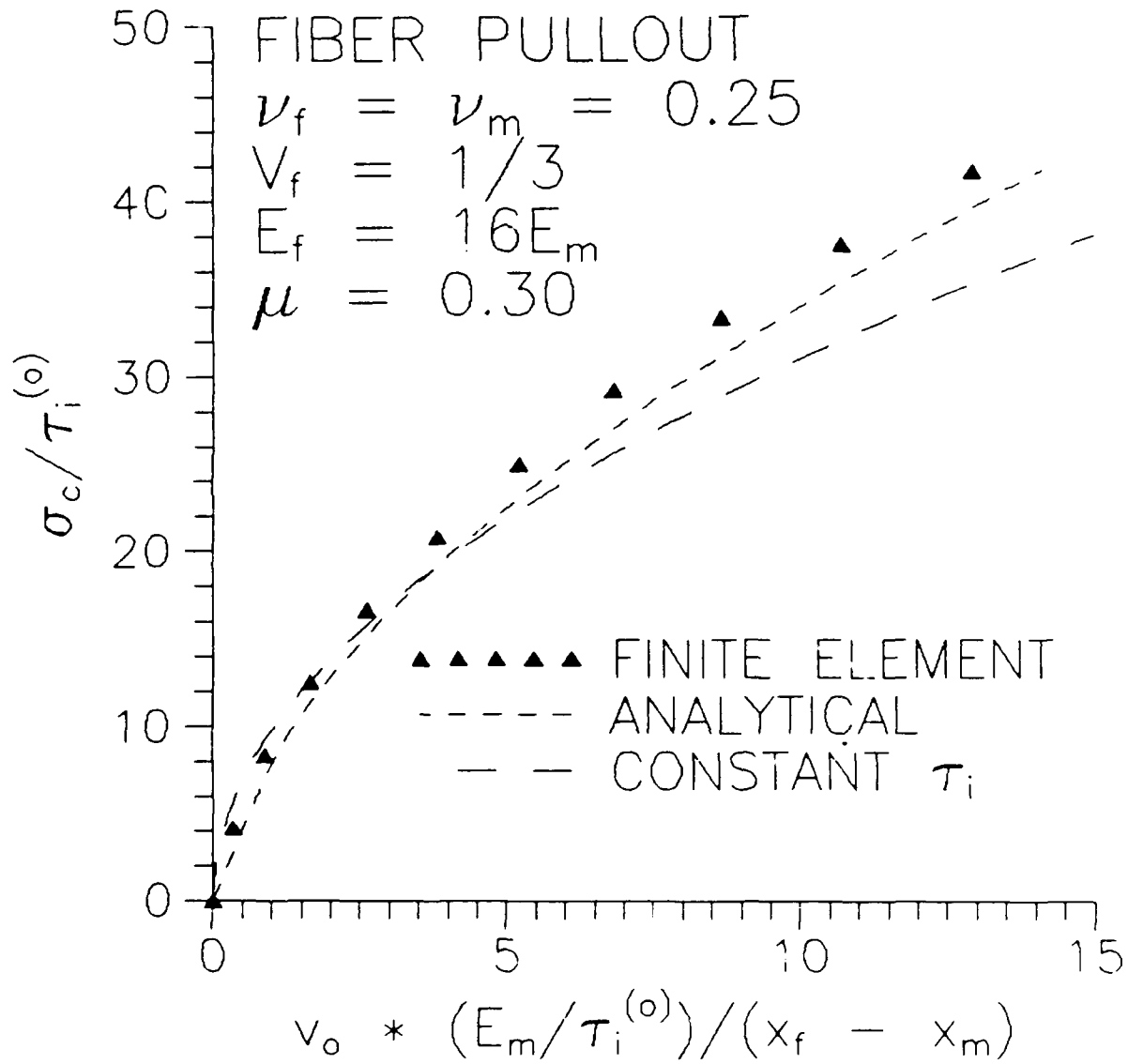
Figure 3.22. Comparison of finite element predictions, present analytical predictions, and the constant τ_i predictions of Marshall, Cox and Evans [13] for fiber pullout response.
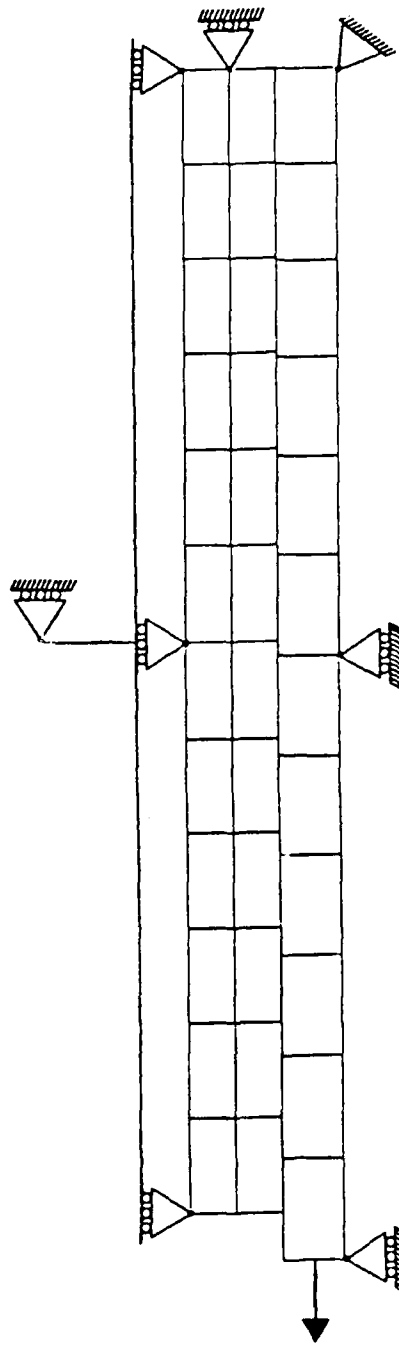
Figure 3.23. The coarse finite element pullout model in a deformed configuration.
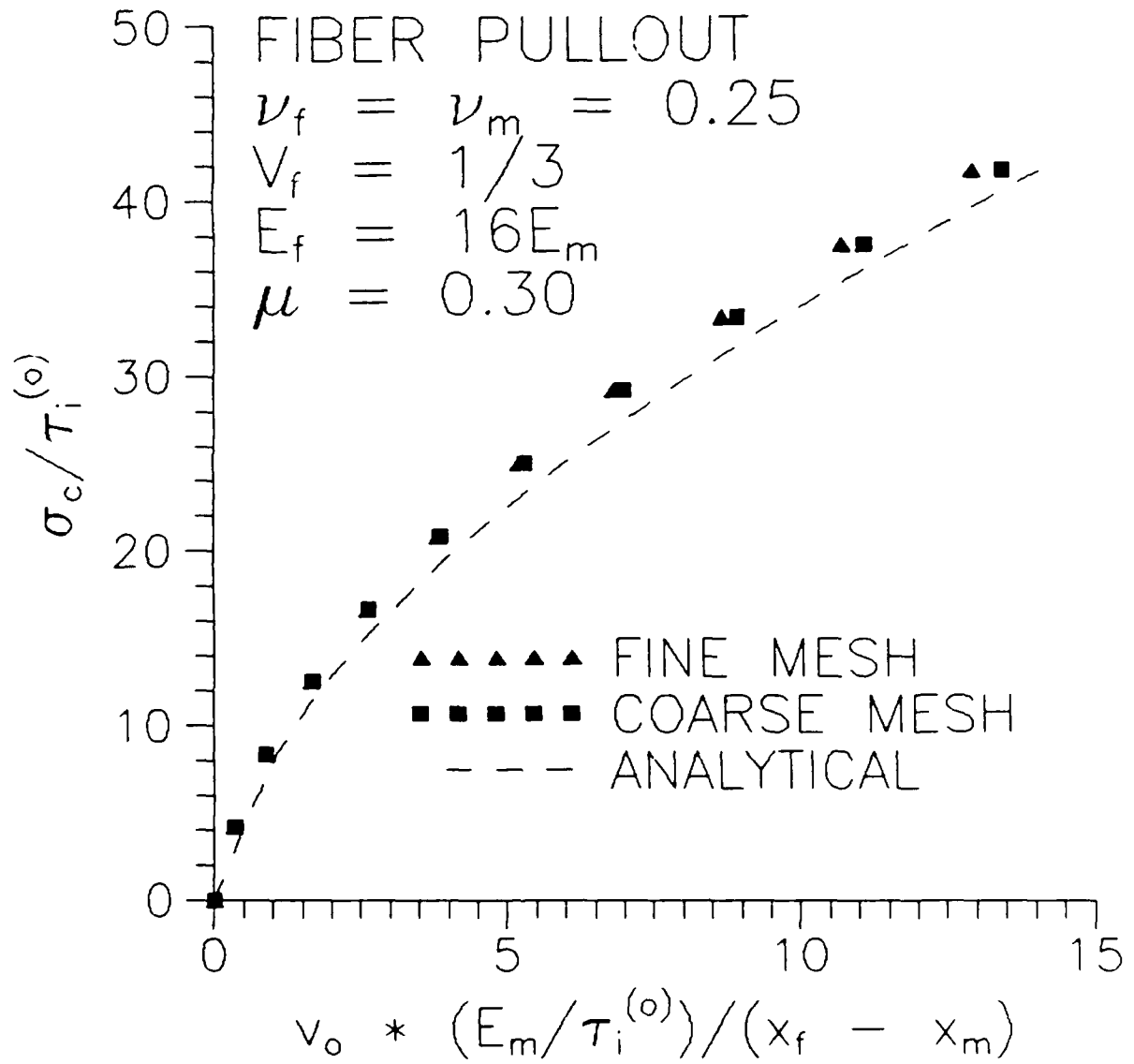
Figure 3.24. Comparison of predicted pullout response from coarse and fine finite element models with the current analytical solution.
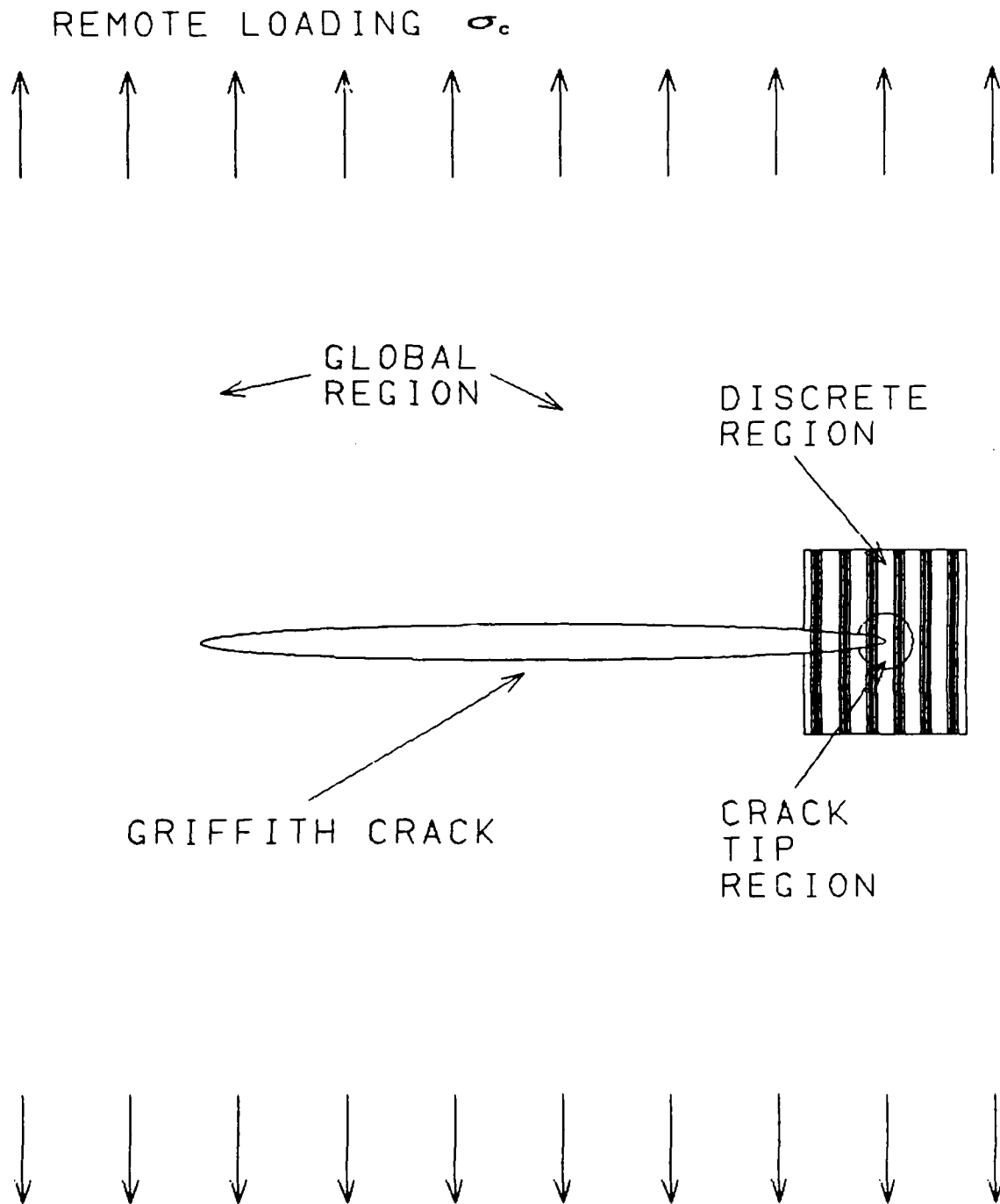
Figure 4.1. A cracked unidirectional composite plate and the three modeling scales: the smeared-out global region, the discrete fiber/matrix micromechanics region and the singular crack tip region.
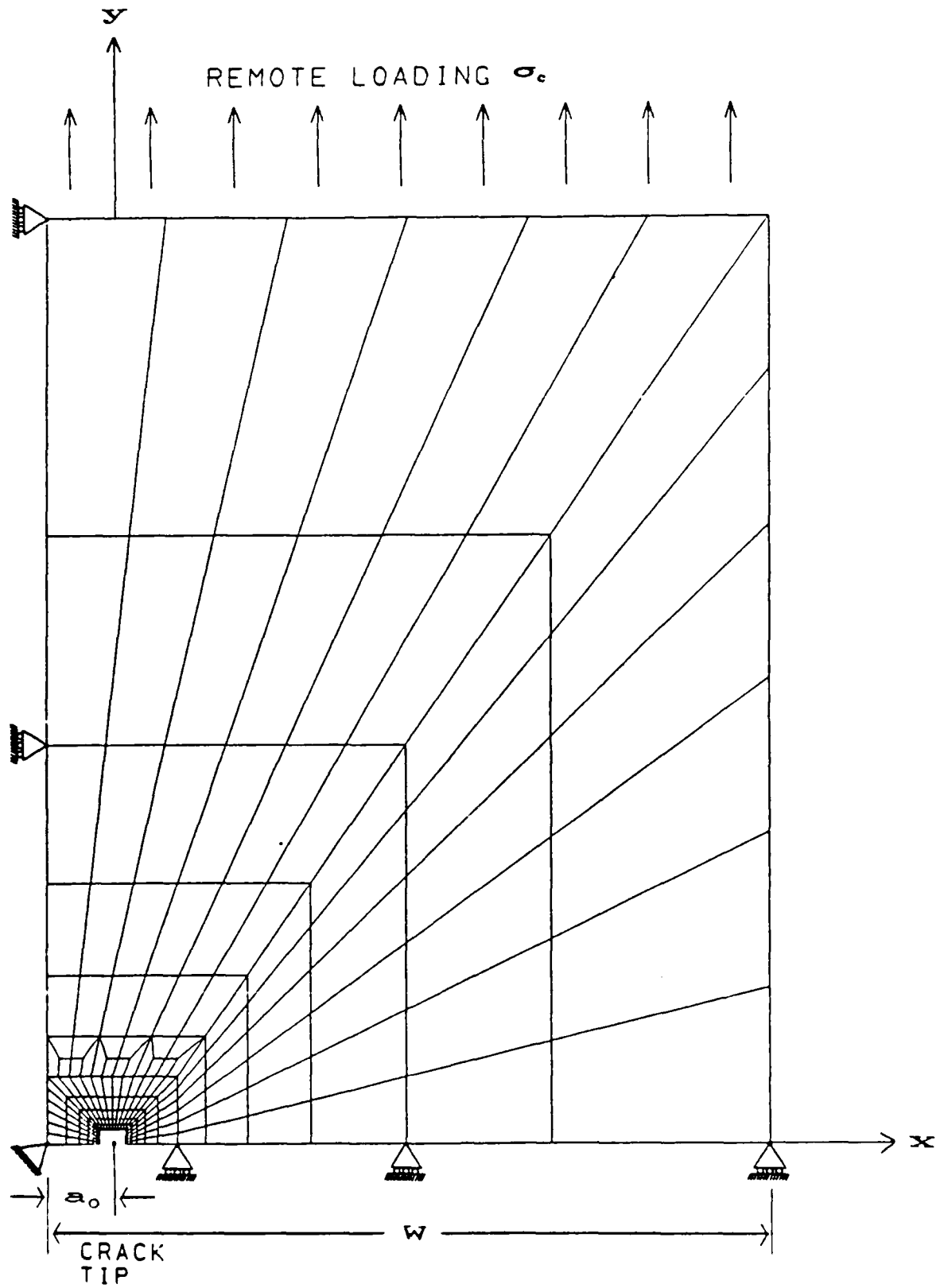
Figure 4.2. The global finite element mesh representing one-quarter of the cracked plate of Fig. 4.1.
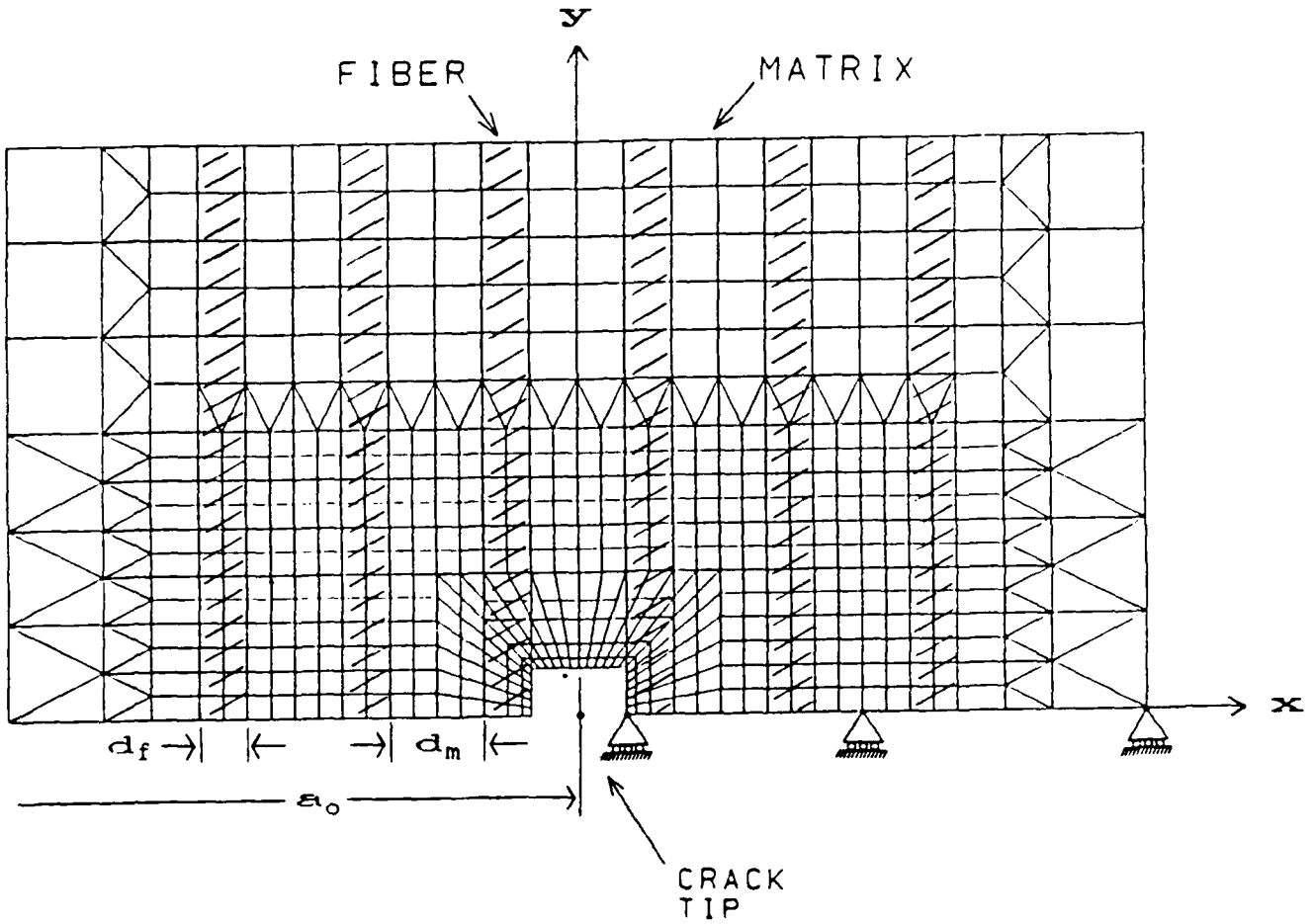
Figure 4.3. The micromechanics mesh representing the discrete fiber (V_f = 1/3) and matrix around the crack tip. This mesh fills the rectangular void in the global mesh of Fig. 4.2.
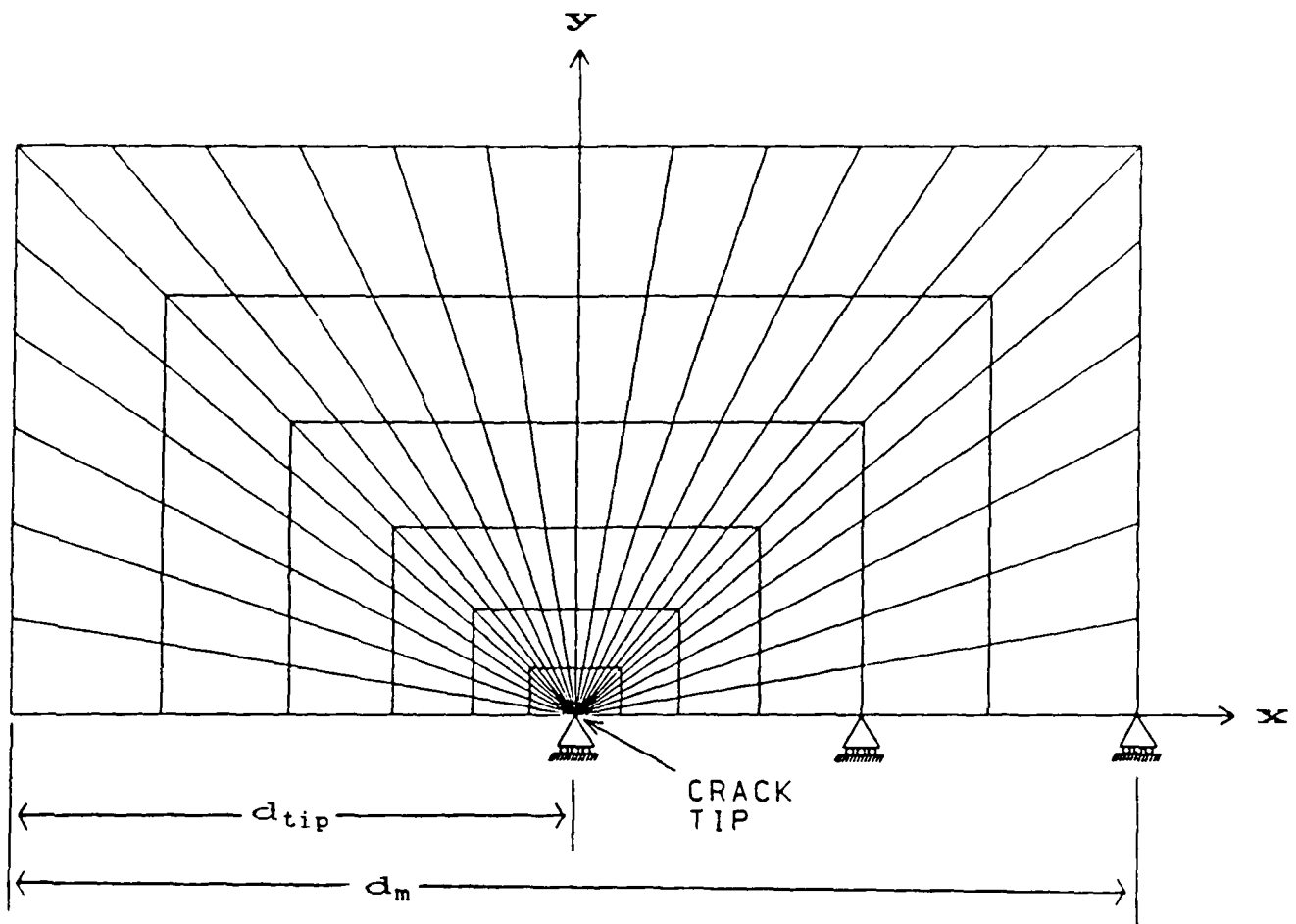
Figure 4.4a. A typical singular mesh representing the crack-tip singular region with $d_{tip}/d_m = 50.0\%$. The singular meshes fill the rectangular void in the micromechanics mesh of Fig. 4.3.
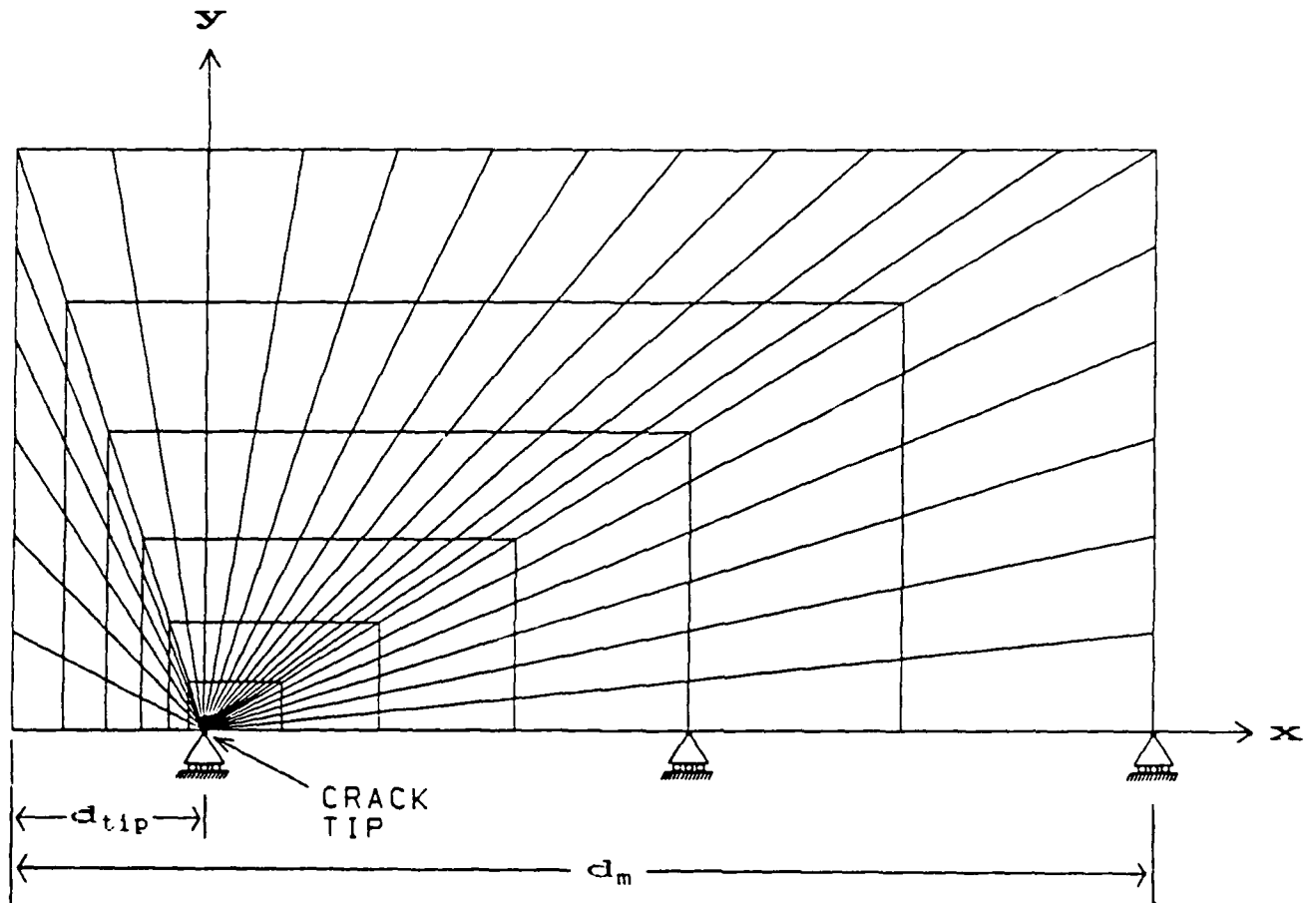
Figure 4.4b. The singular region mesh with $d_{tip}/d_m = 16.7\%$.
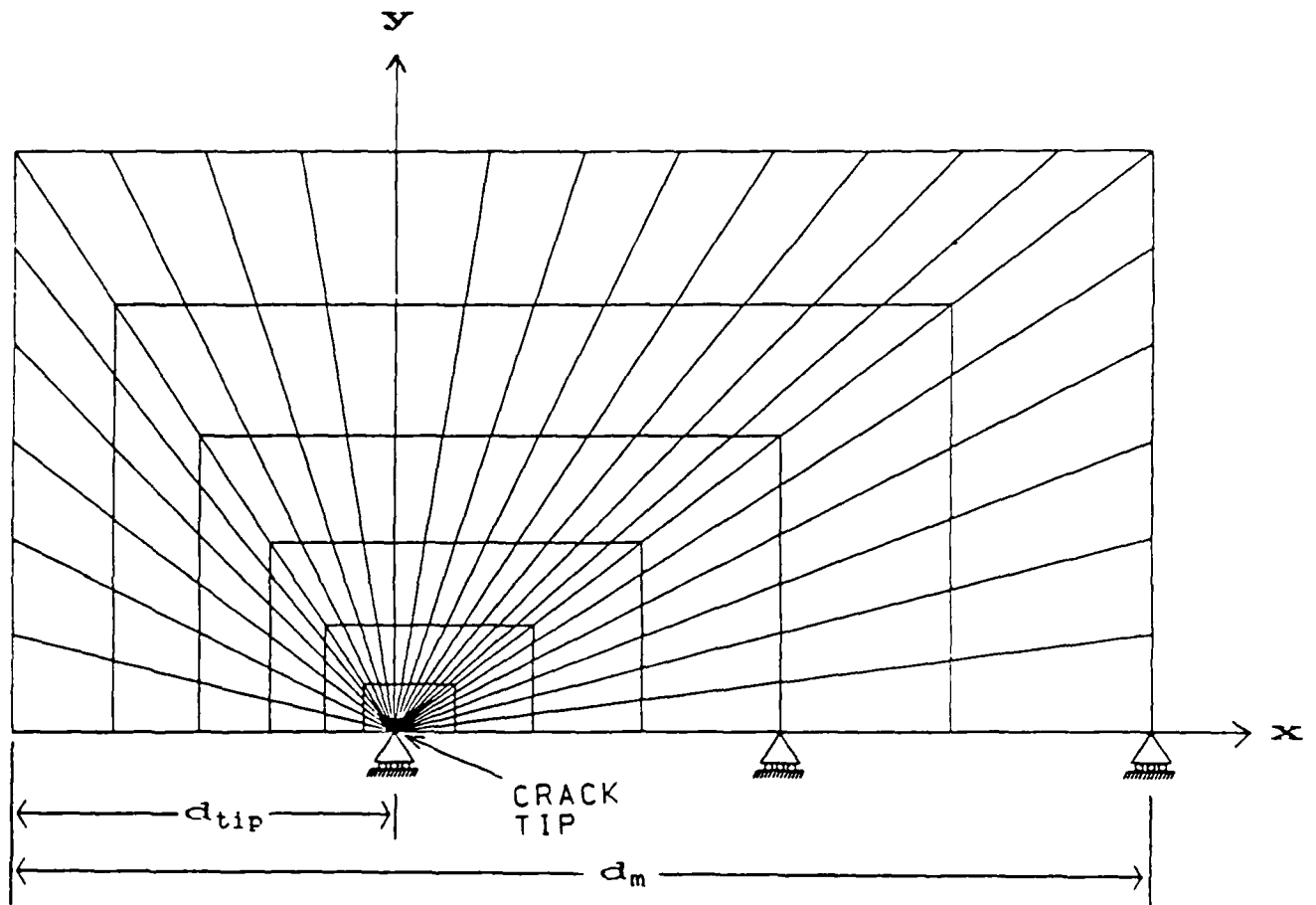
Figure 4.4c. The singular region mesh with $d_{tip}/d_m = 33.3\%$.
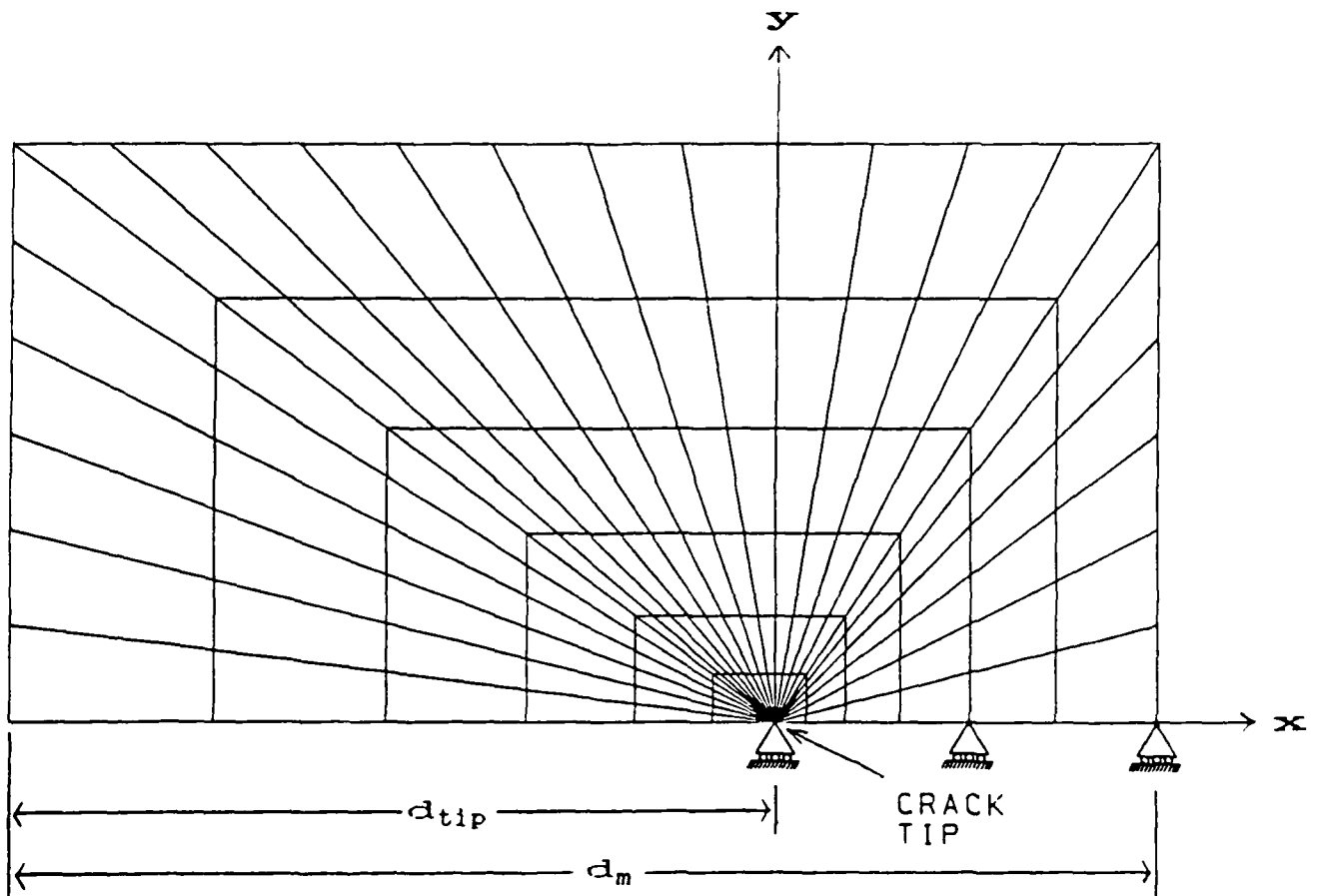
Figure 4.4d. The singular region mesh with $d_{tip}/d_m = 66.7\%$.
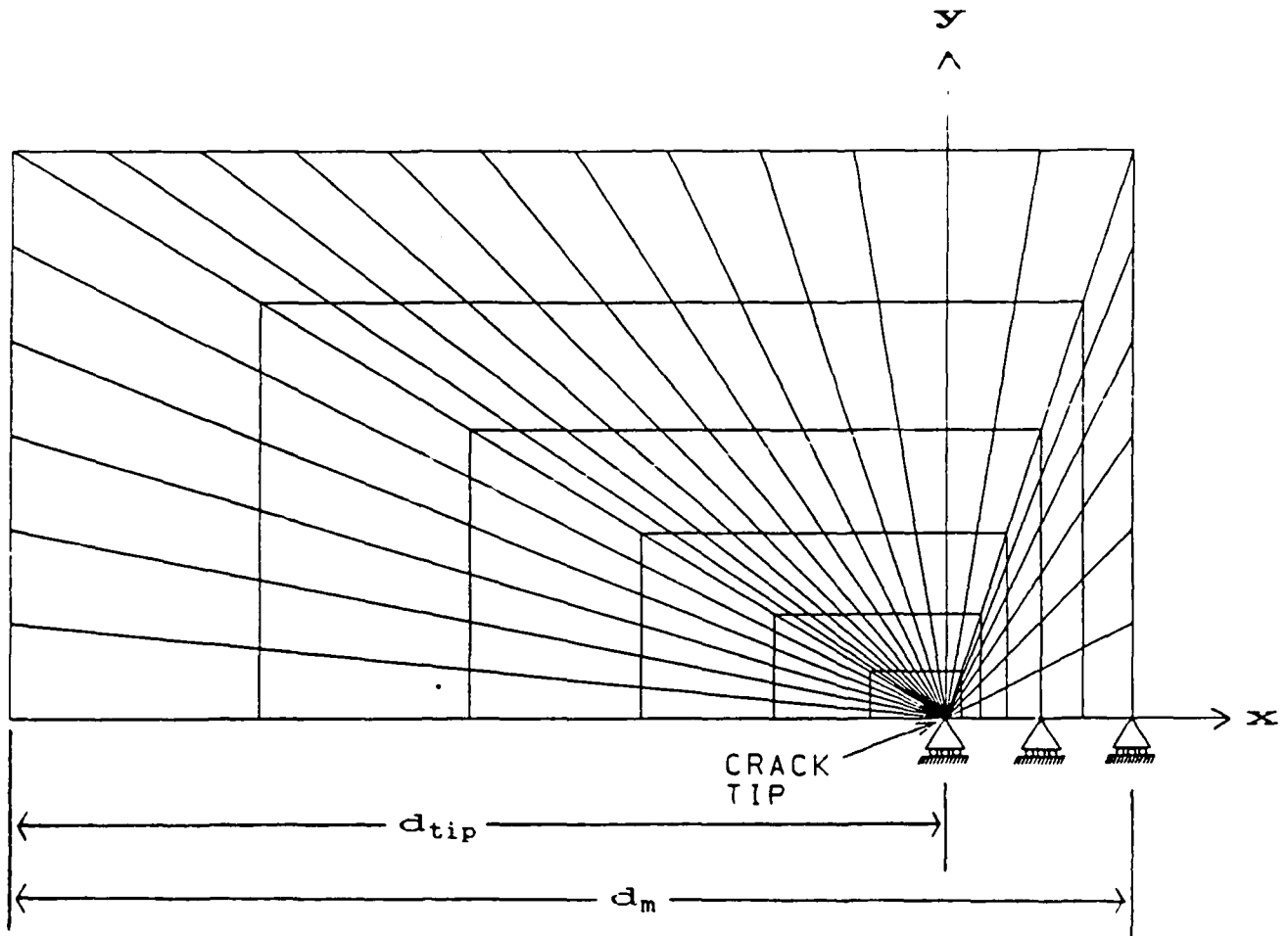
Figure 4.4e. The singular region mesh with $d_{tip}/d_m = 83.3\%$.
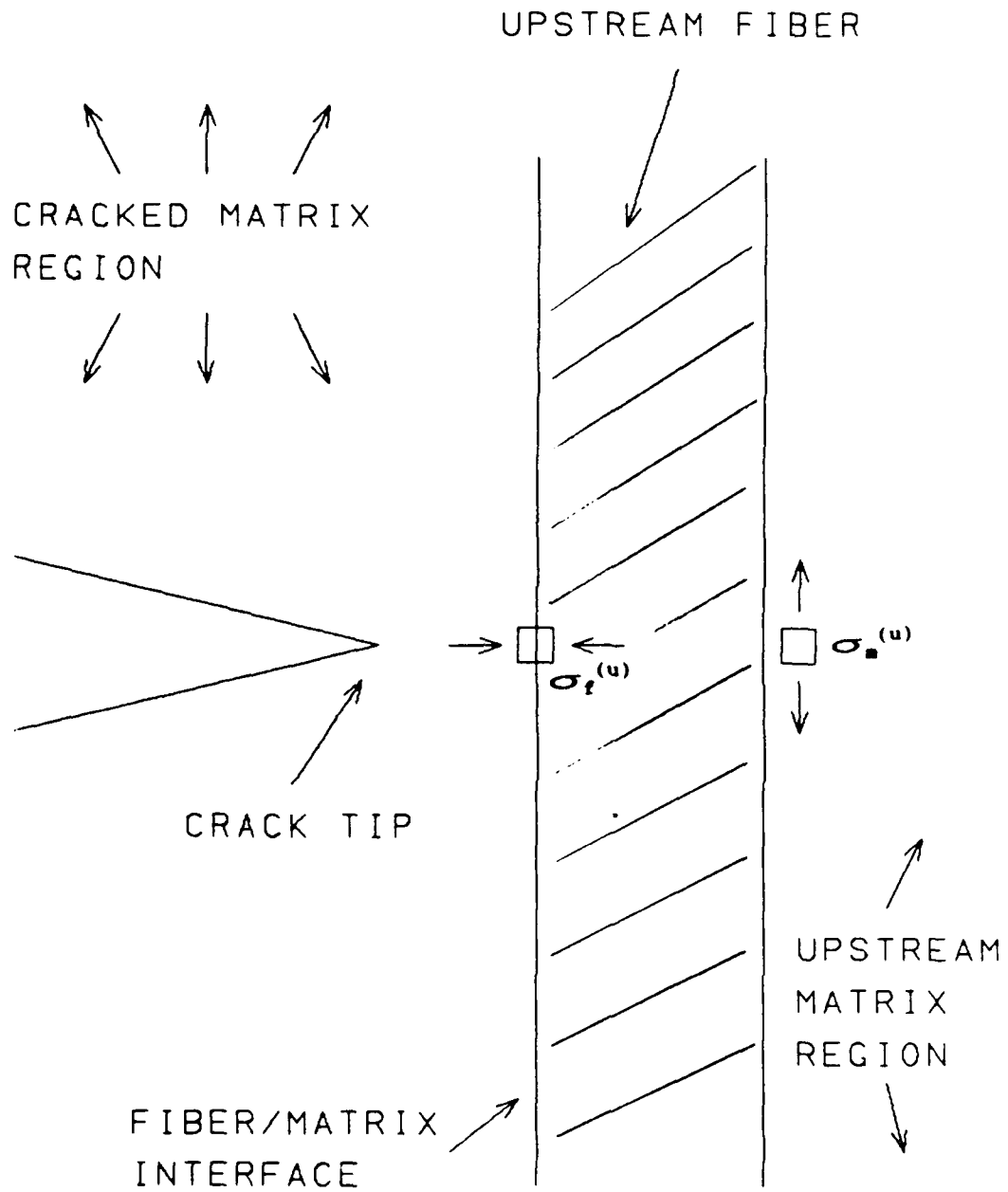
Figure 4.5. Location and orientation of the upstream interface compressive stress $\sigma_i^{(u)}$ and matrix tensile stress $\sigma_m^{(u)}$.

114
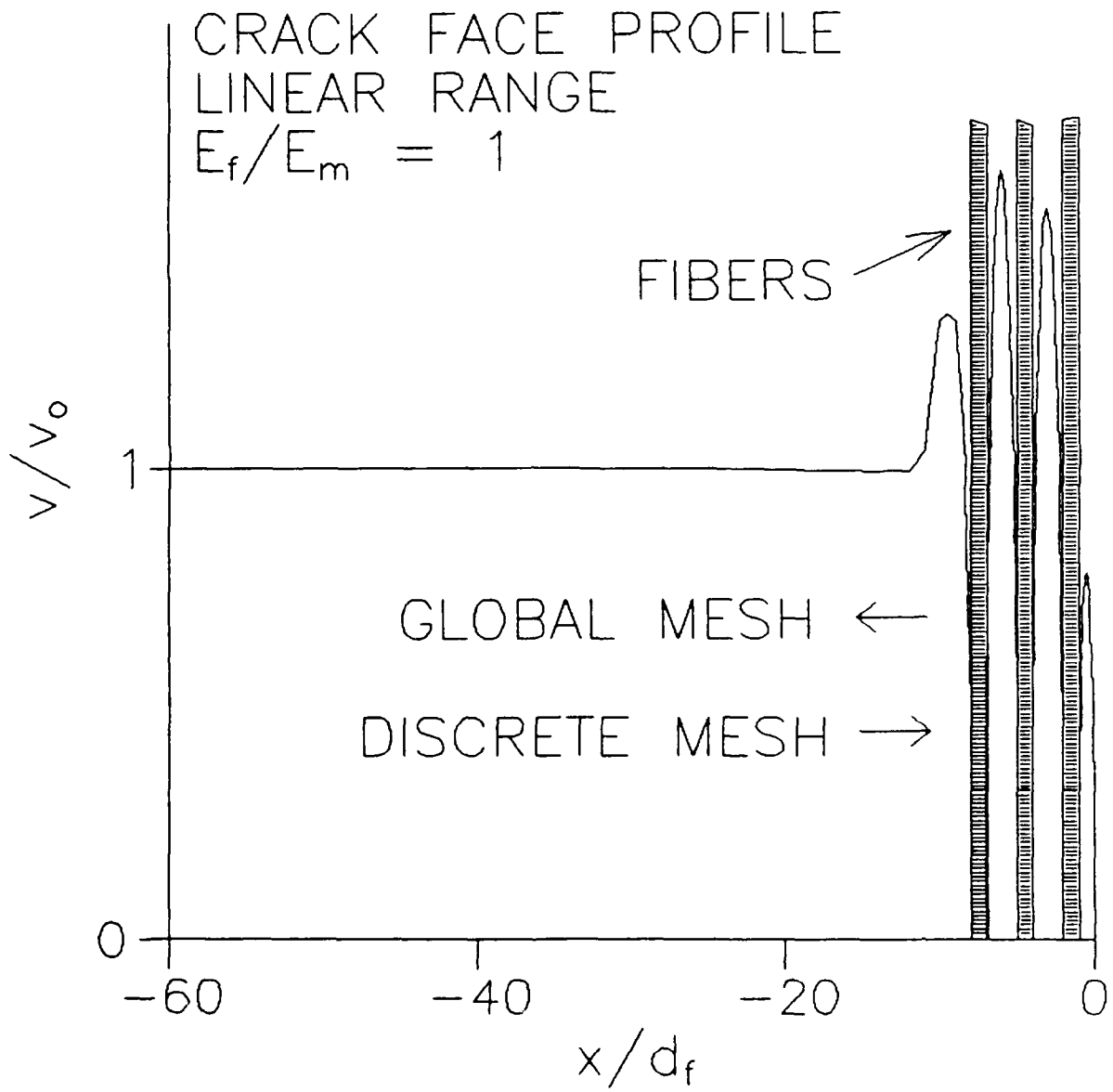
Figure 4.6a. Typical crack face profile when $E_f/E_m = 1$ and the fibers are sticking. The matrix crack opening displacement v is zero at the fiber/matrix interface. (Note the discrete local and smeared-out global bridging regions.)
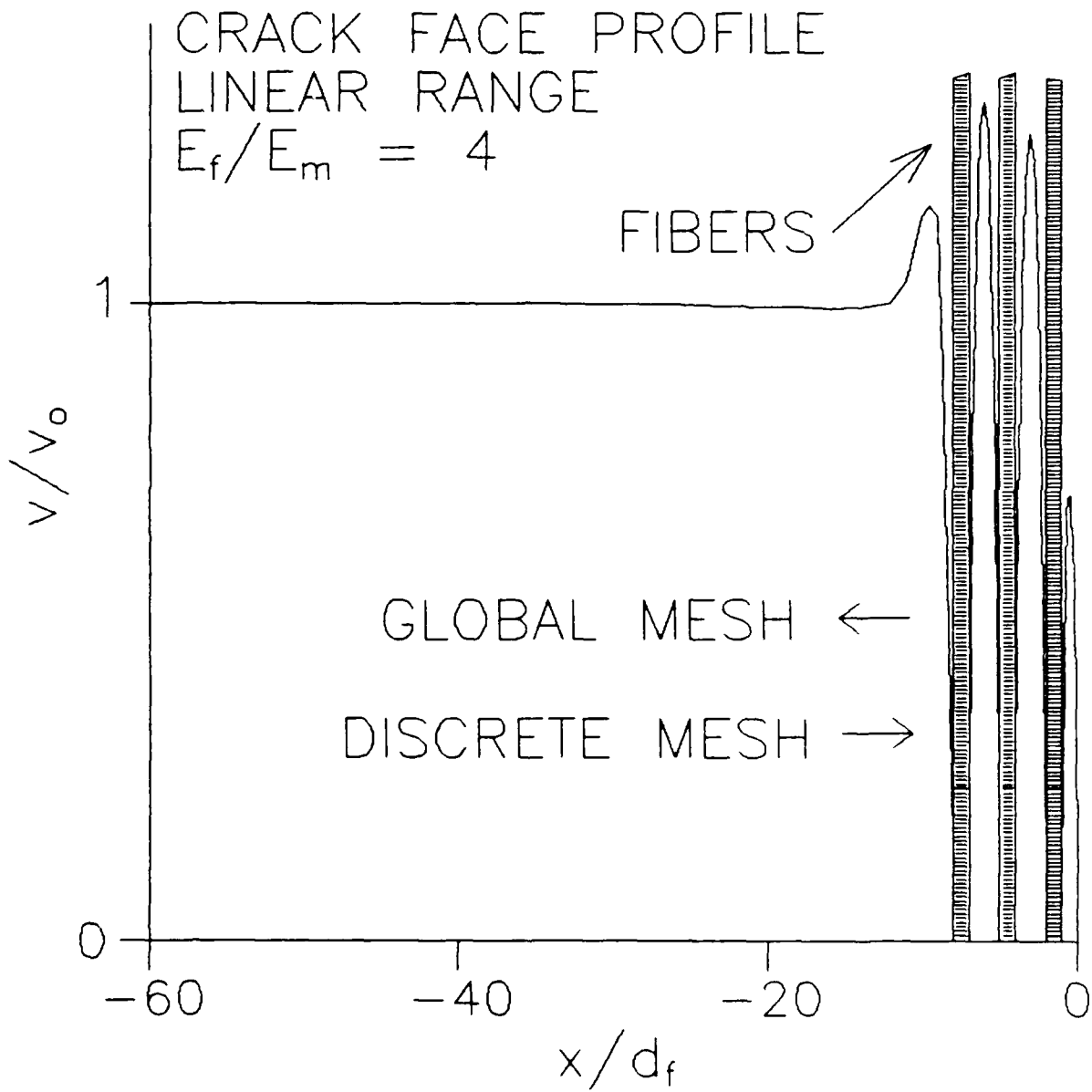
Figure 4.6b. Typical crack face profile when E_f/E_m = 4 and the fibers are <u>sticking</u>. The matrix crack opening displacement v is zero at the fiber/matrix interface in the discrete region.
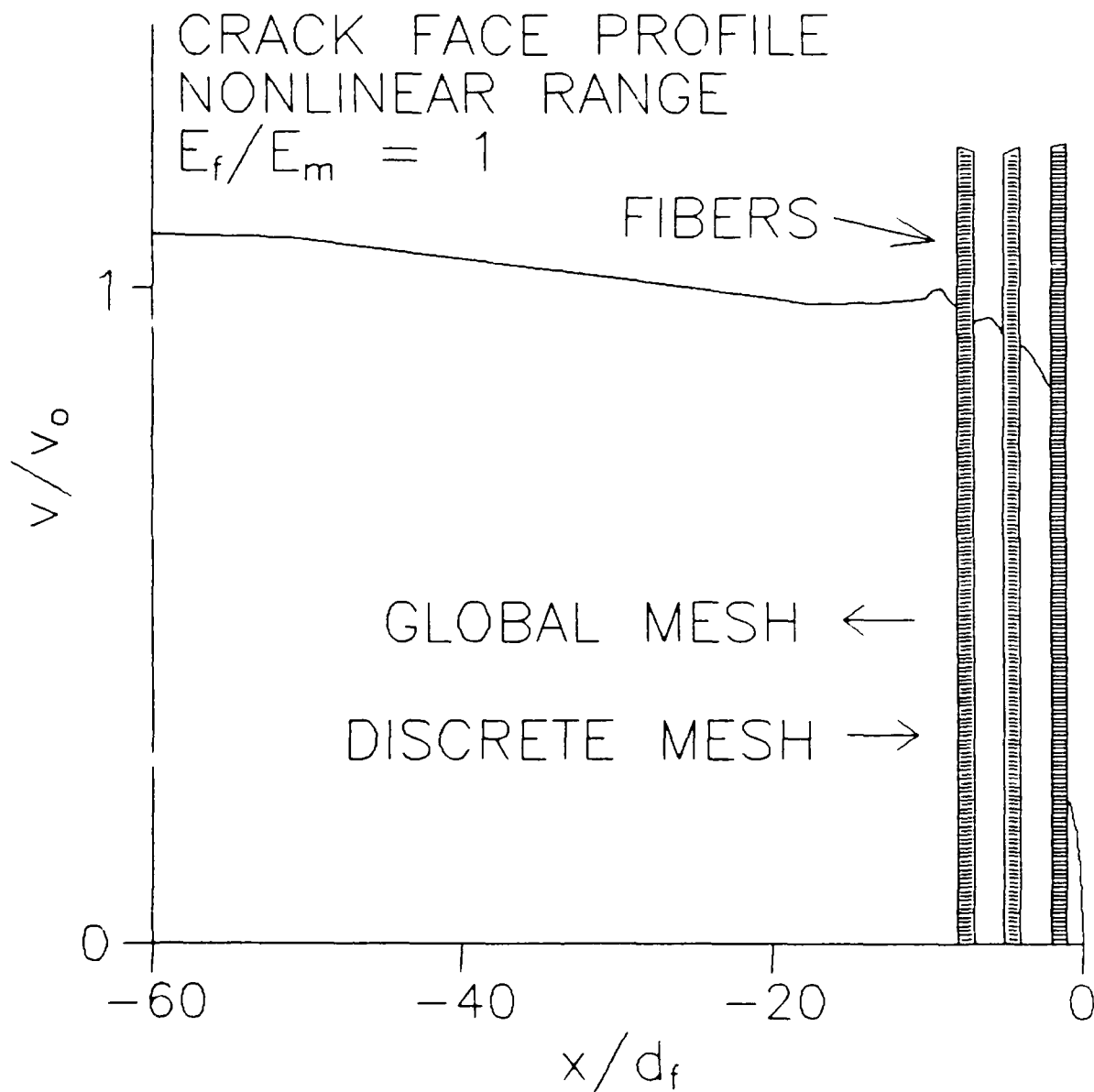
Figure 4.7a. Typical crack face profile when $E_f/E_m = 1$ and the bridging fibers are _slipping_. The matrix crack opening displacement v is non-zero at the fiber/matrix interface in the discrete region.

117
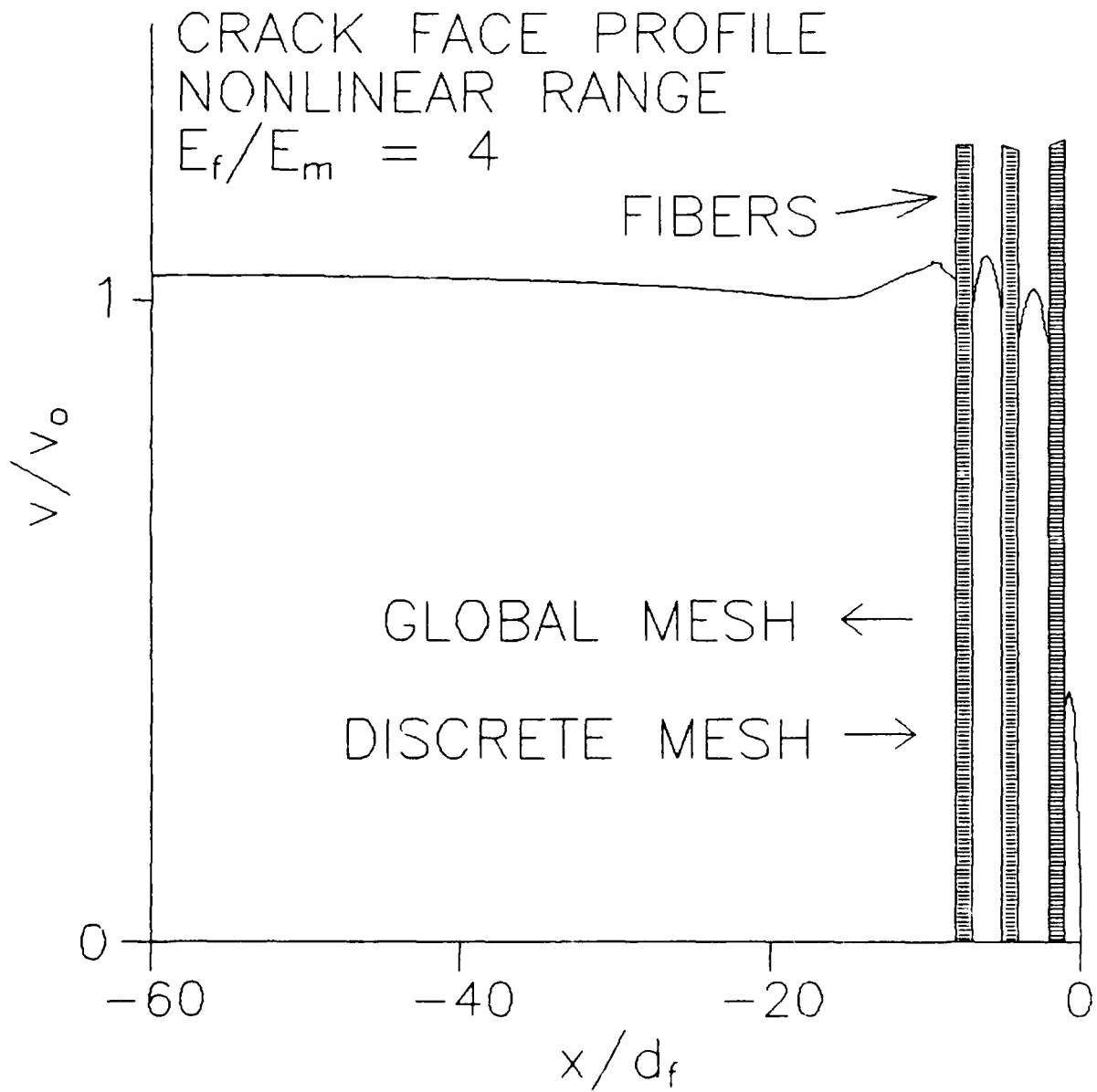
Figure 4.7b. Typical crack face profile when $E_f/E_m = 4$ and the bridging fibers are slipping. The matrix crack opening displacement v is non-zero at the fiber/matrix interface in the discrete region.
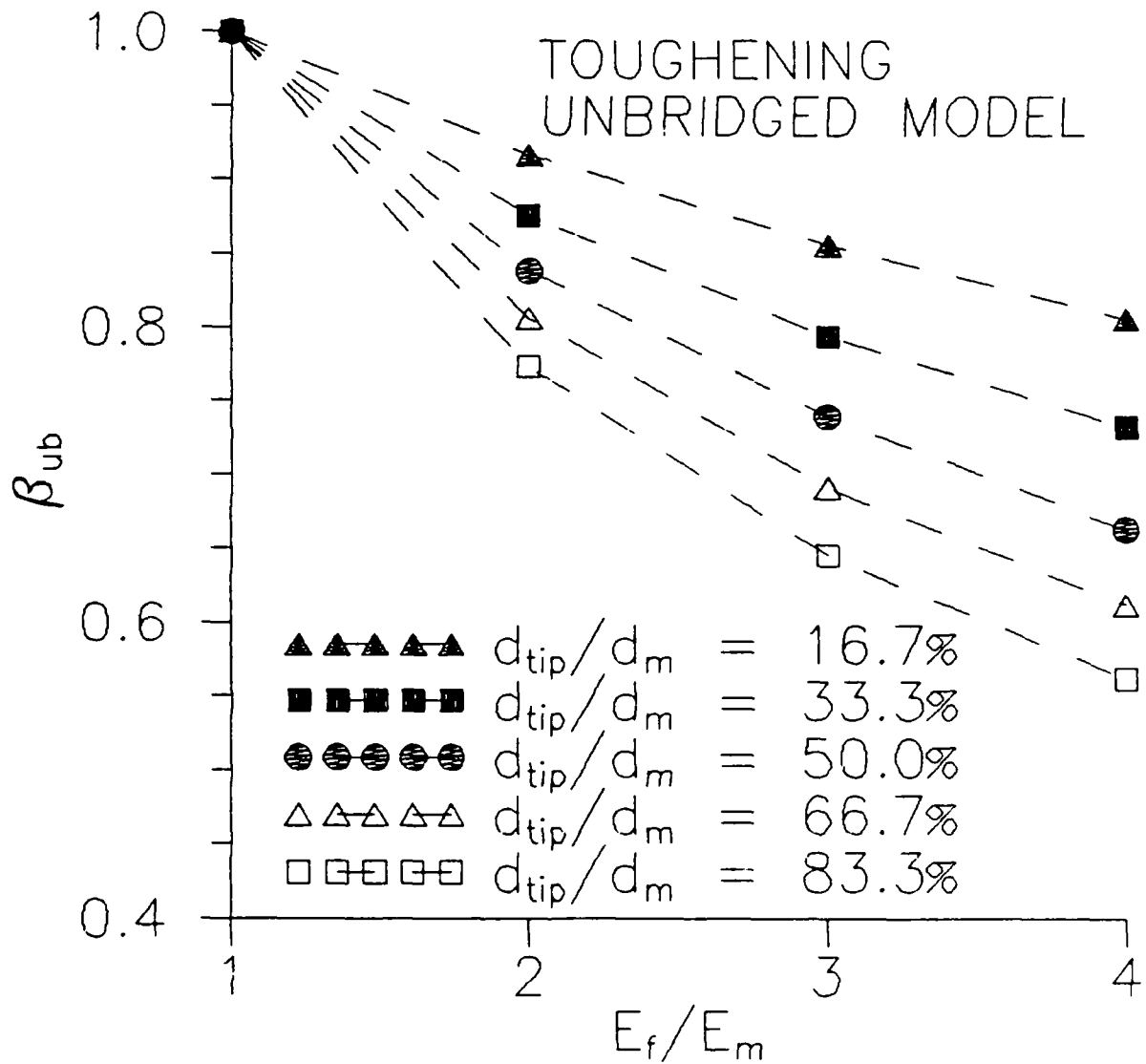
Figure 4.8. Variation of the unbridged toughening parameter β_{ub} with stiffness ratio E_f/E_m and crack tip position d_{tip}/d_m.
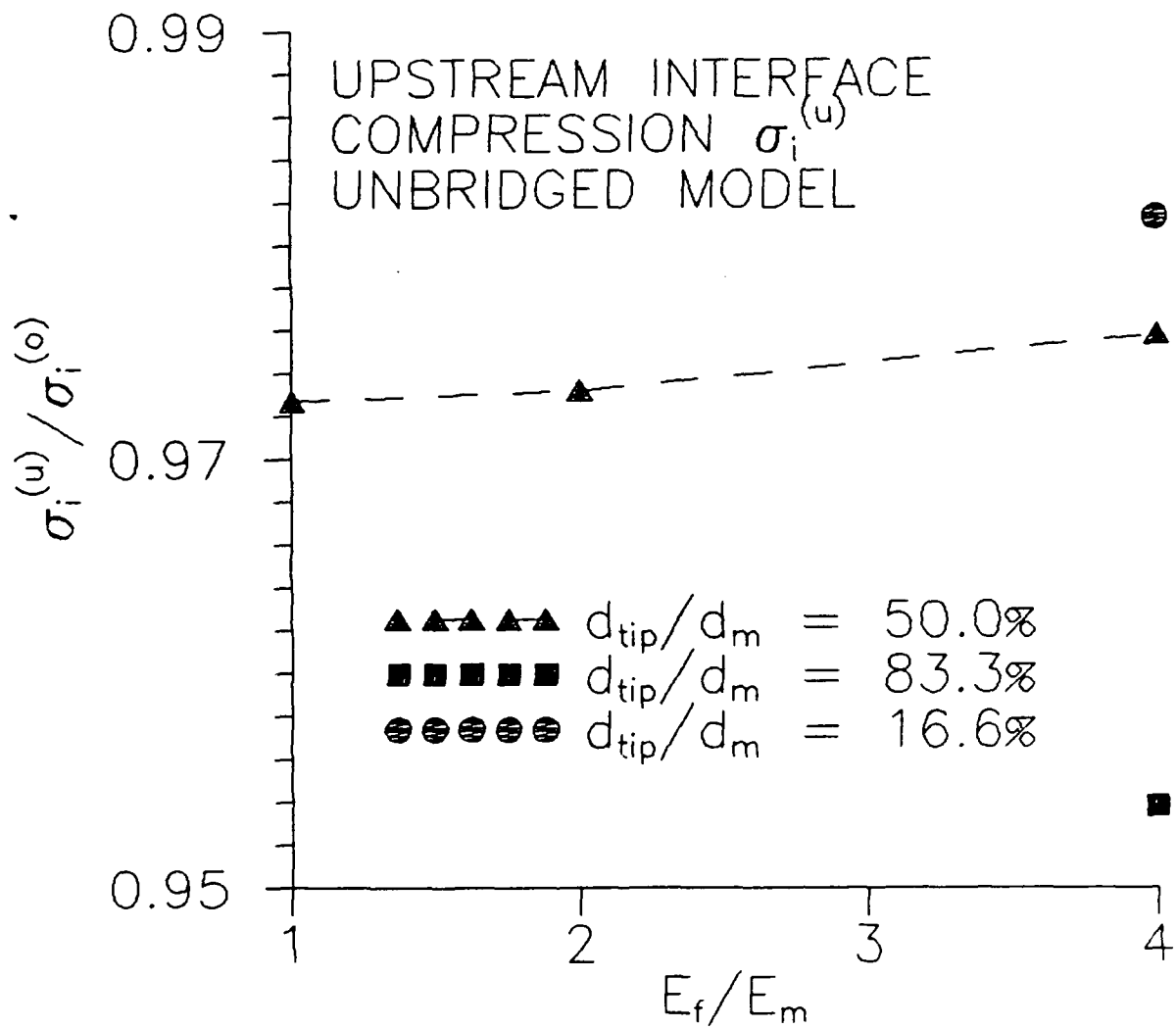
Figure 4.9. Variation of the immediate upstream interface compressive stress $\sigma_i^{(u)}$ with E_f/E_m and d_{tip}/d_m in the unbridged model.
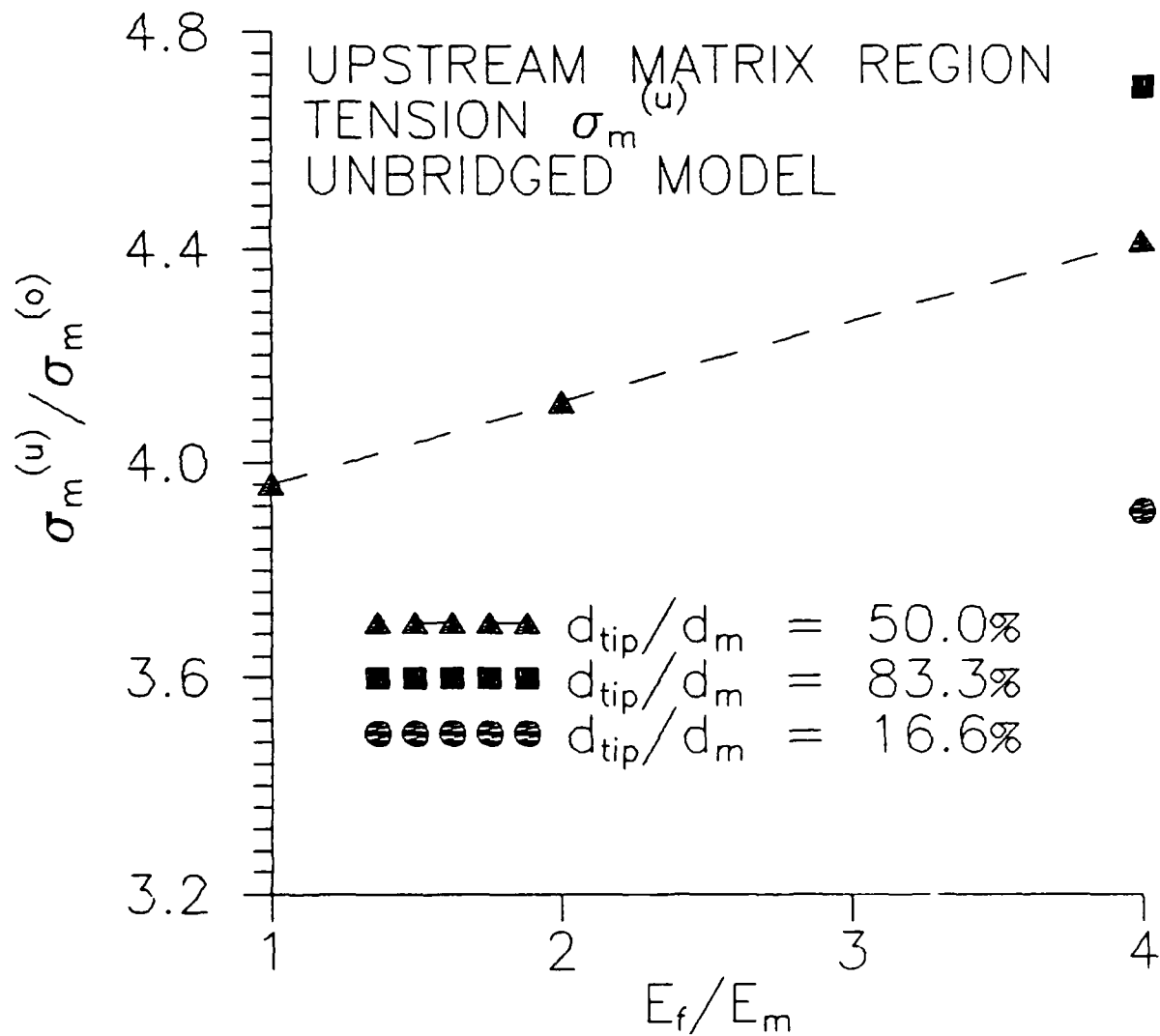
Figure 4.10. Variation of the highest principle stress in the first upstream matrix region σ_m^u with E_f/E_m and d_{tip}/d_m in the unbridged model.
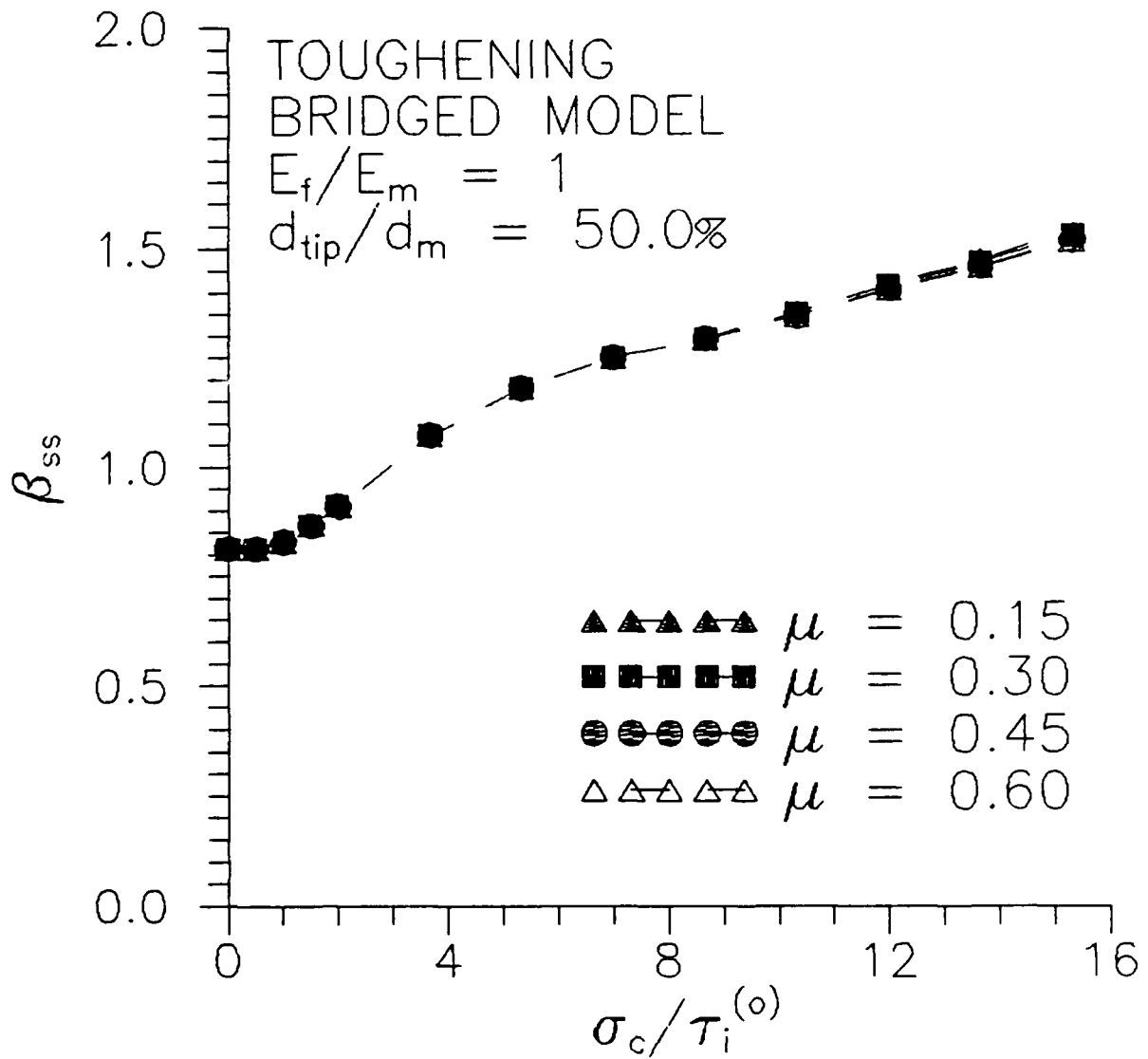
Figure 4.11a. Variation of the bridged toughening parameter β_{ss} with friction coefficient μ and remote applied loading σ_c when $E_f/E_m = 1$ and $d_{tip}/d_m = 50.0\%$. The toughening is independent of μ.
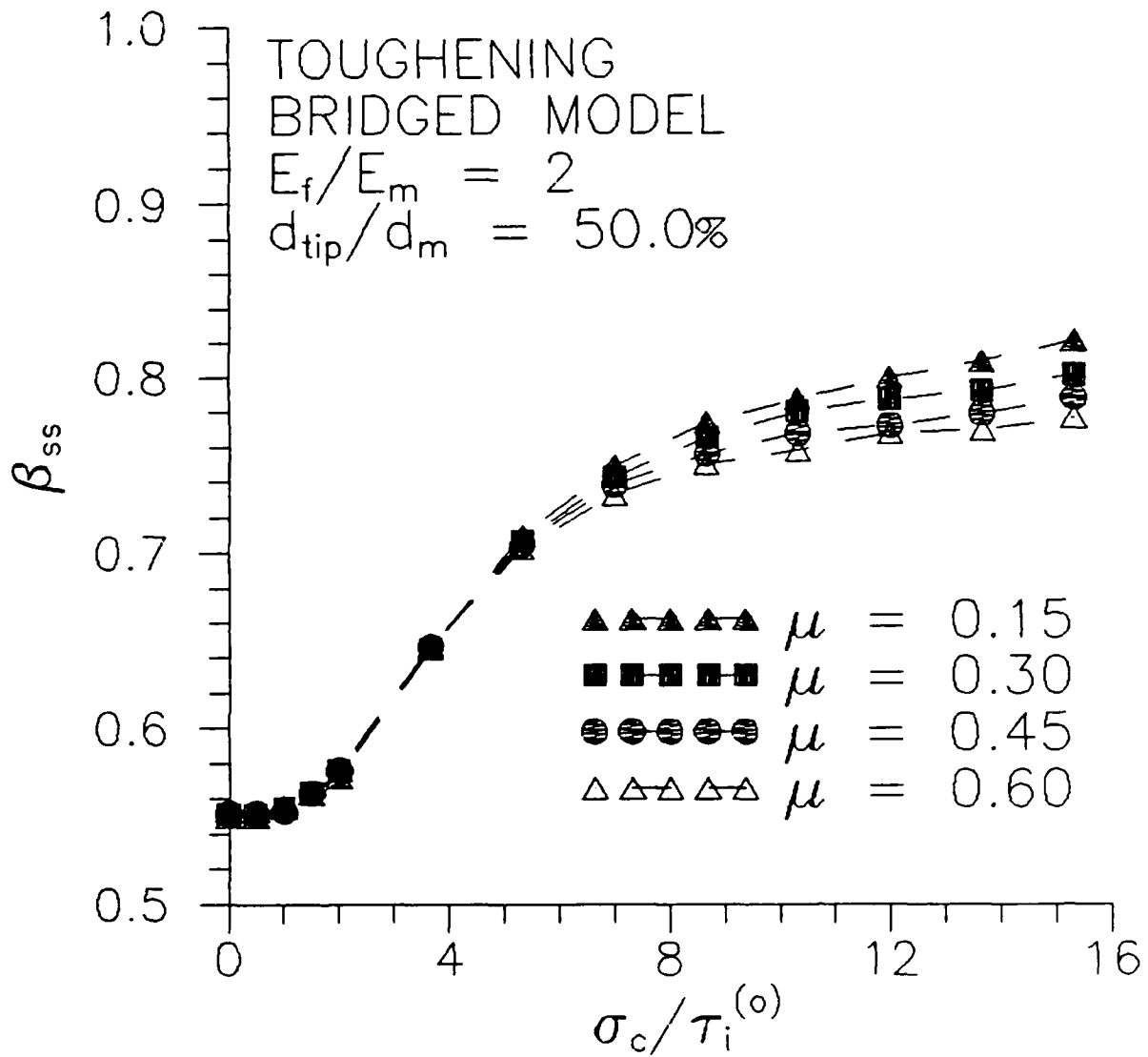
Figure 4.11b. Variation of the bridged toughening parameter β_{ss} with friction coefficient μ and remote applied loading σ_c when $E_f/E_m = 2$ and $d_{tip}/d_m = 50.0\%$.
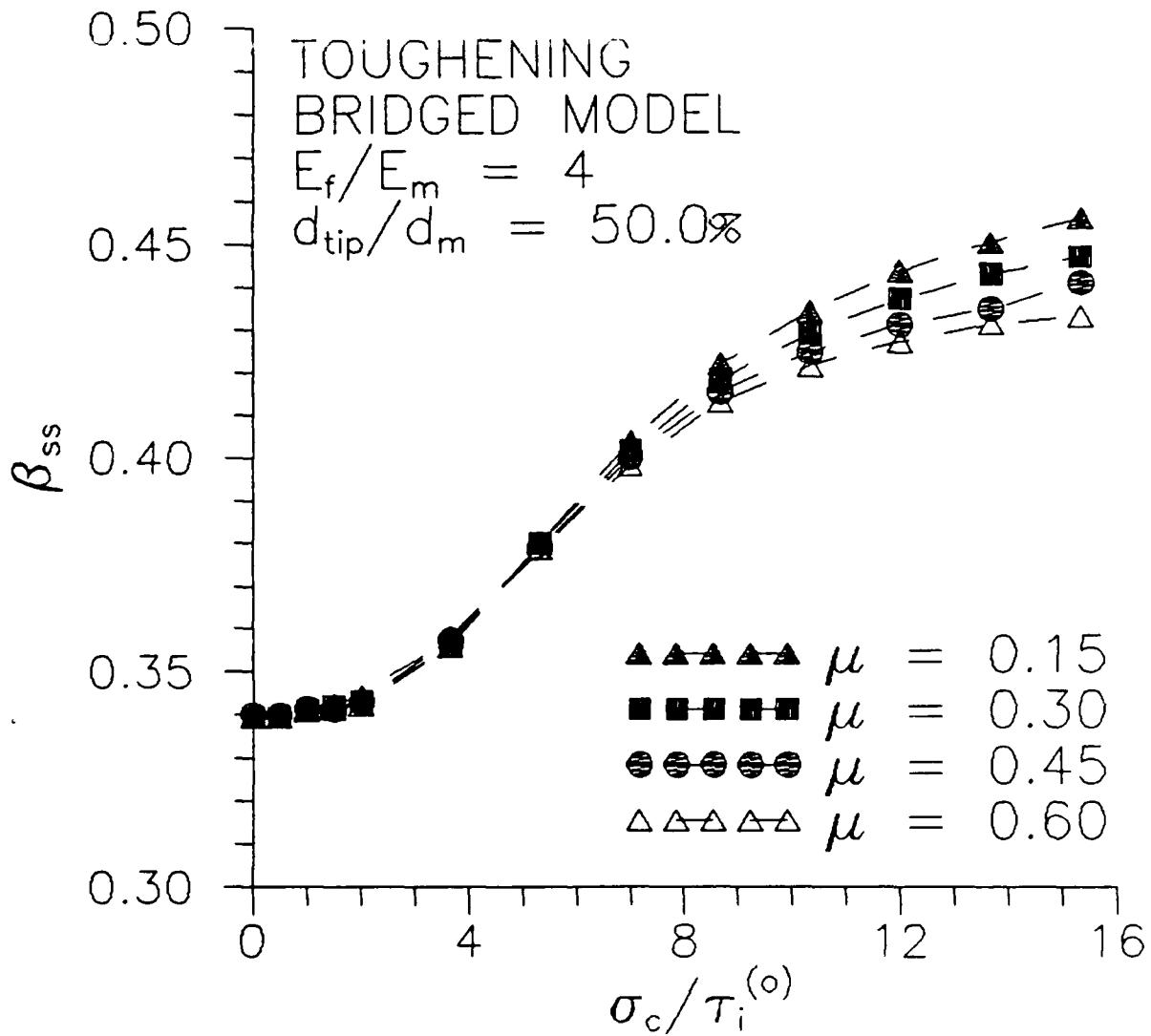
Figure 4.11c. Variation of the bridged toughening parameter β_{ss} with friction coefficient μ and remote applied loading σ_c when $E_f/E_m = 4$ and $d_{tip}/d_m = 50.0\%$.
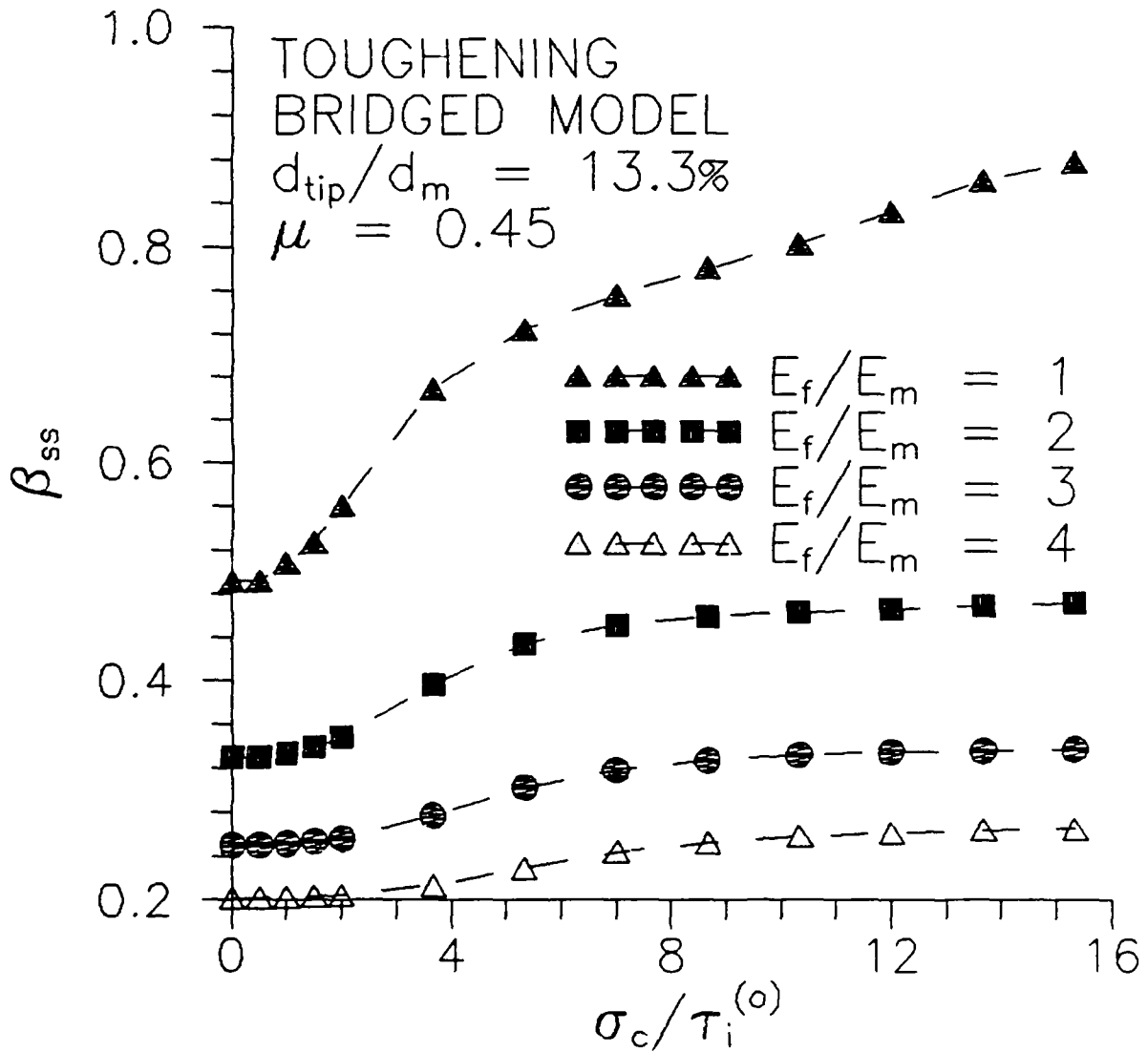
Figure 4.12a. Variation of the toughening parameter β_{ss} with stiffness ratio E_f/E_m and remote applied loading σ_c when $d_{tip}/d_m = 16.7\%$ and $\mu = 0.45$. The toughening increases with E_f/E_m.
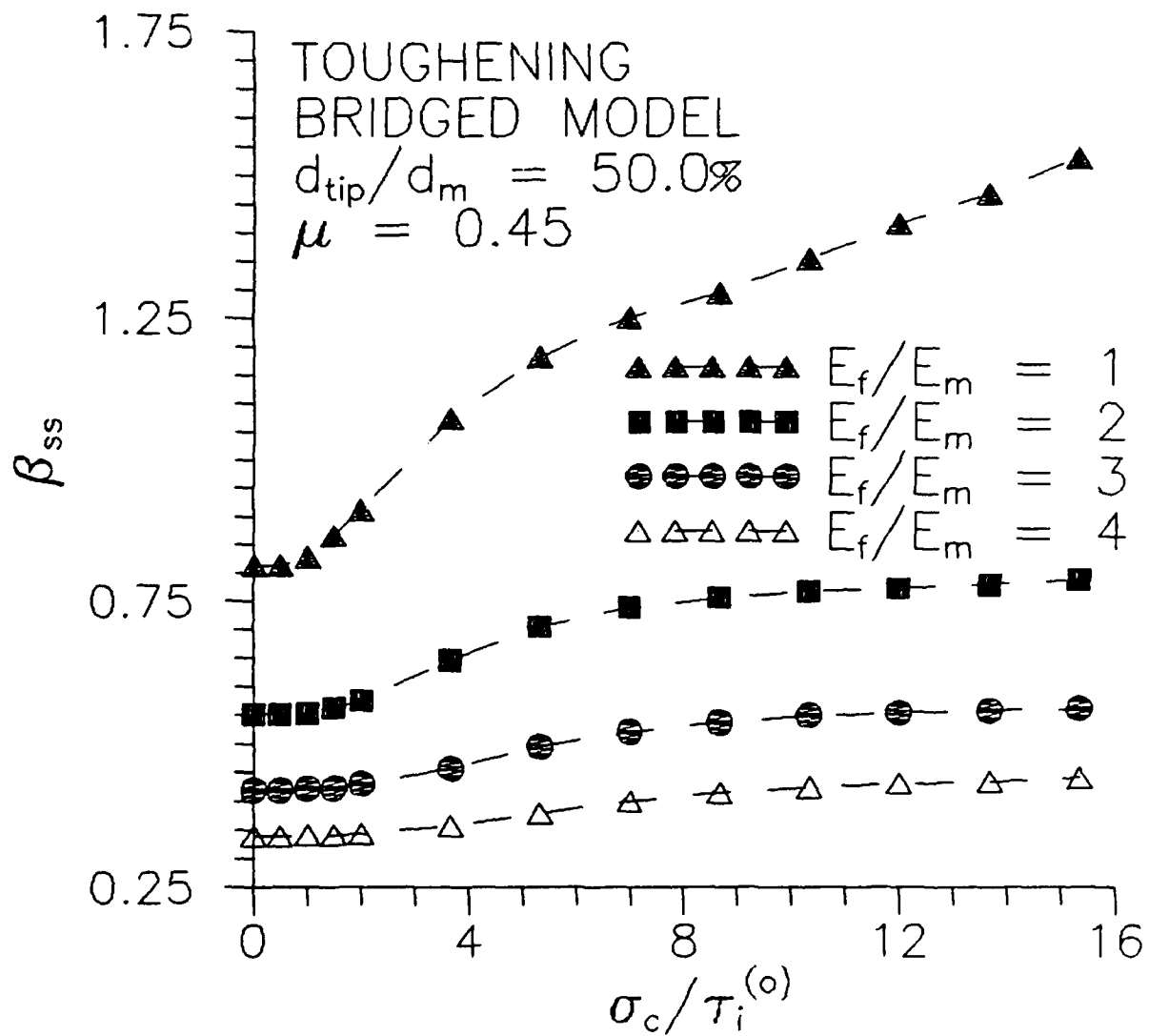
Figure 4.12b. Variation of the bridged toughening parameter β_{ss} with stiffness ratio E_f/E_m and remote applied loading σ_c when $d_{tip}/d_m = 50.0\%$ and $\mu = 0.45$.
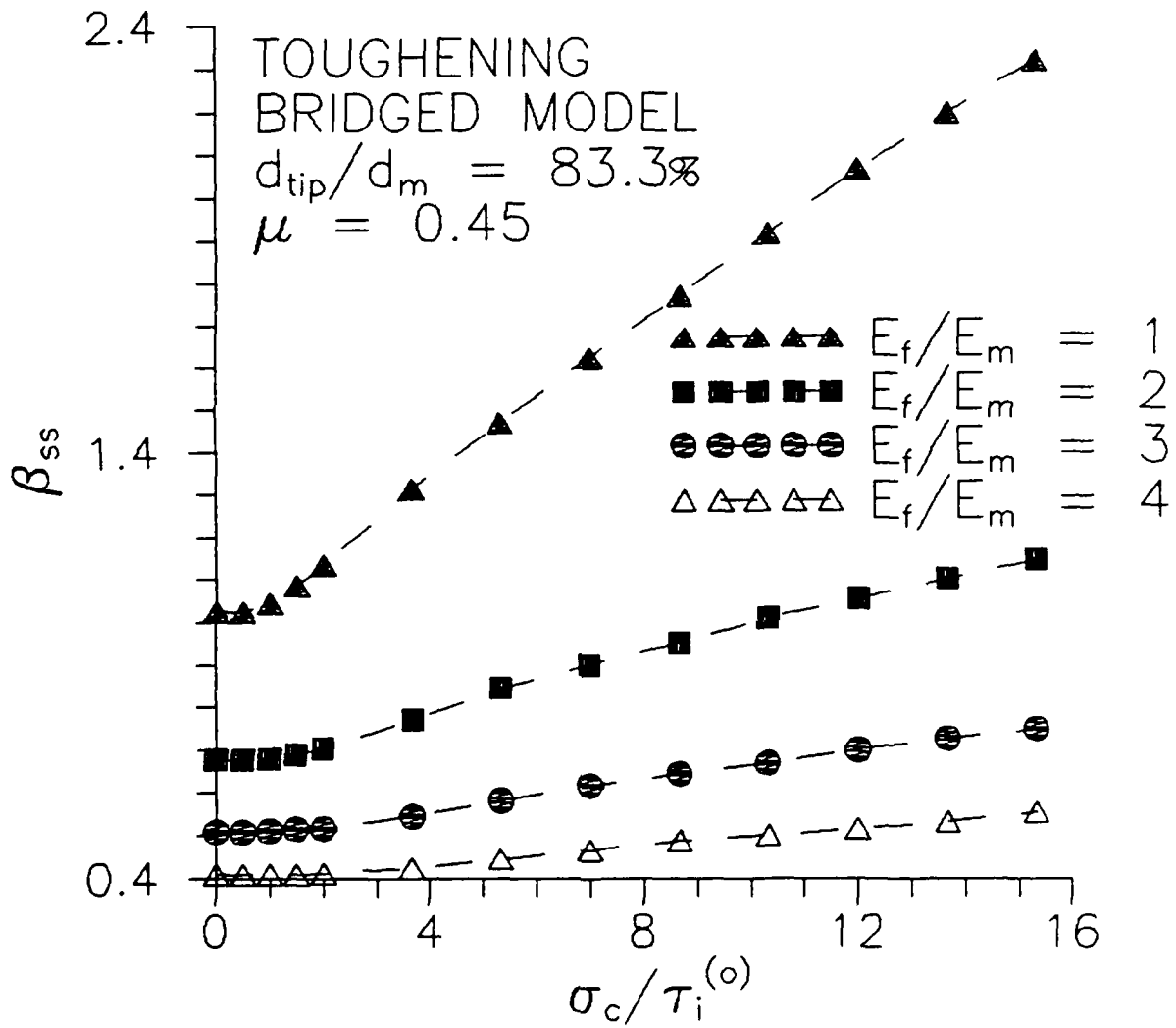
Figure 4.12c. Variation of the bridged toughening parameter β_{ss} with stiffness ratio E_f/E_m and remote applied loading σ_c when $d_{tip}/d_m = 83.3\%$ and $\mu = 0.45$.
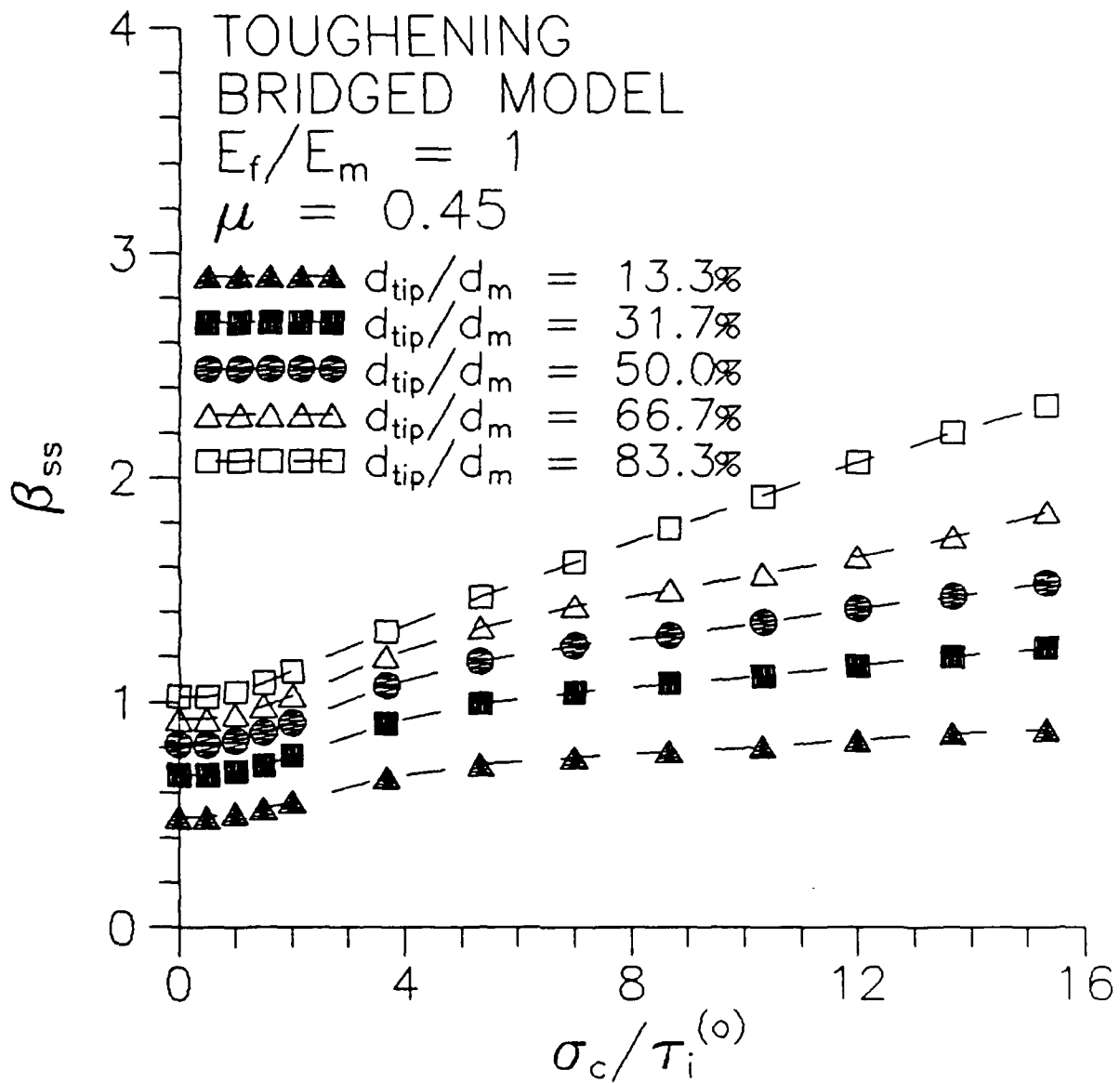
**Figure 4.13a.** Variation of the bridged toughening parameter β_{ss} with crack tip position d_{tip}/d_m and remote applied loading σ_c when $E_f/E_m = 1$ and $\mu = 0.45$.
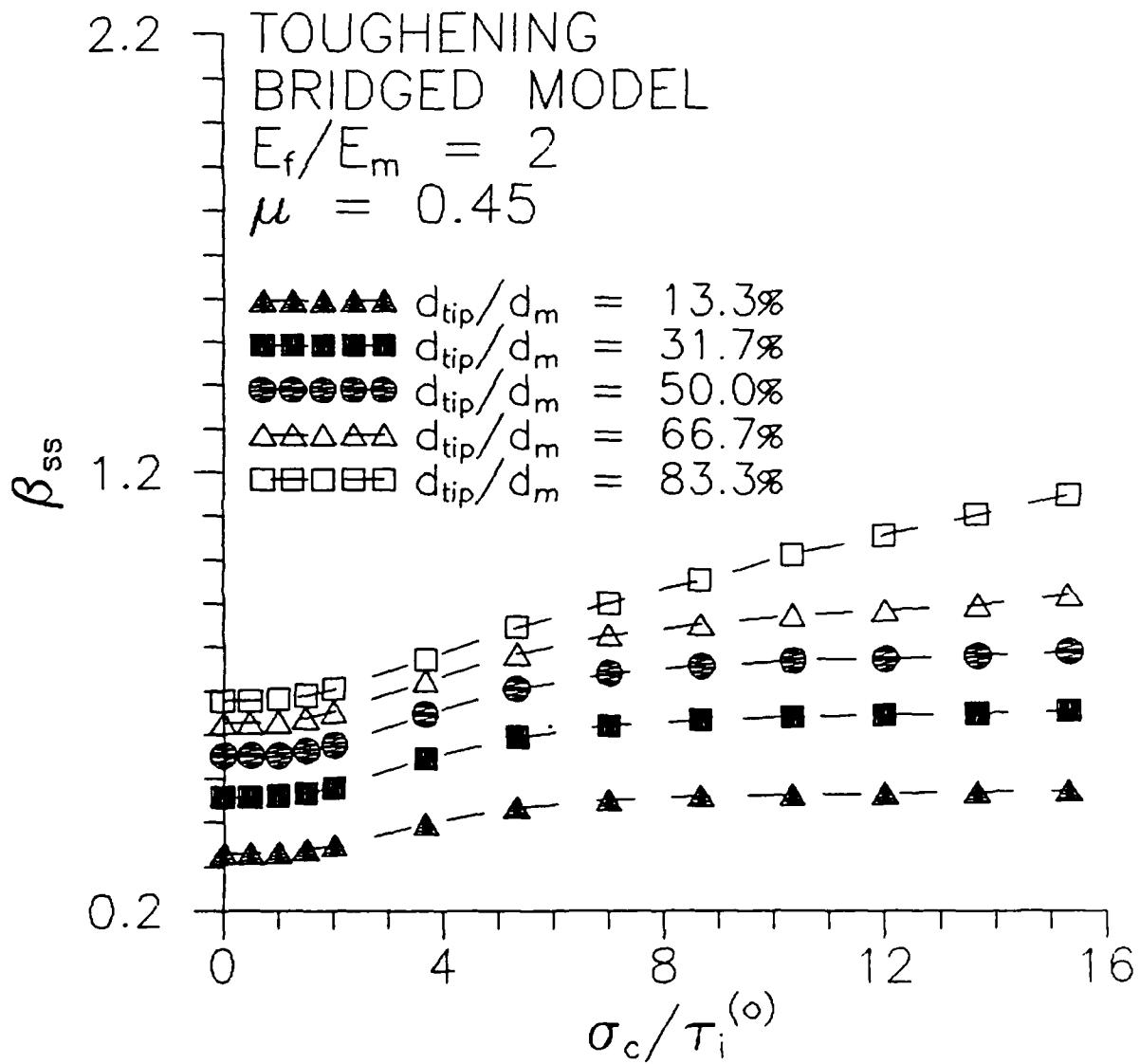
Figure 4.13b. Variation of the bridged toughening parameter β_{ss} with crack tip position d_{tip}/d_m and remote applied loading σ_c when $E_f/E_m = 2$ and $\mu = 0.45$.
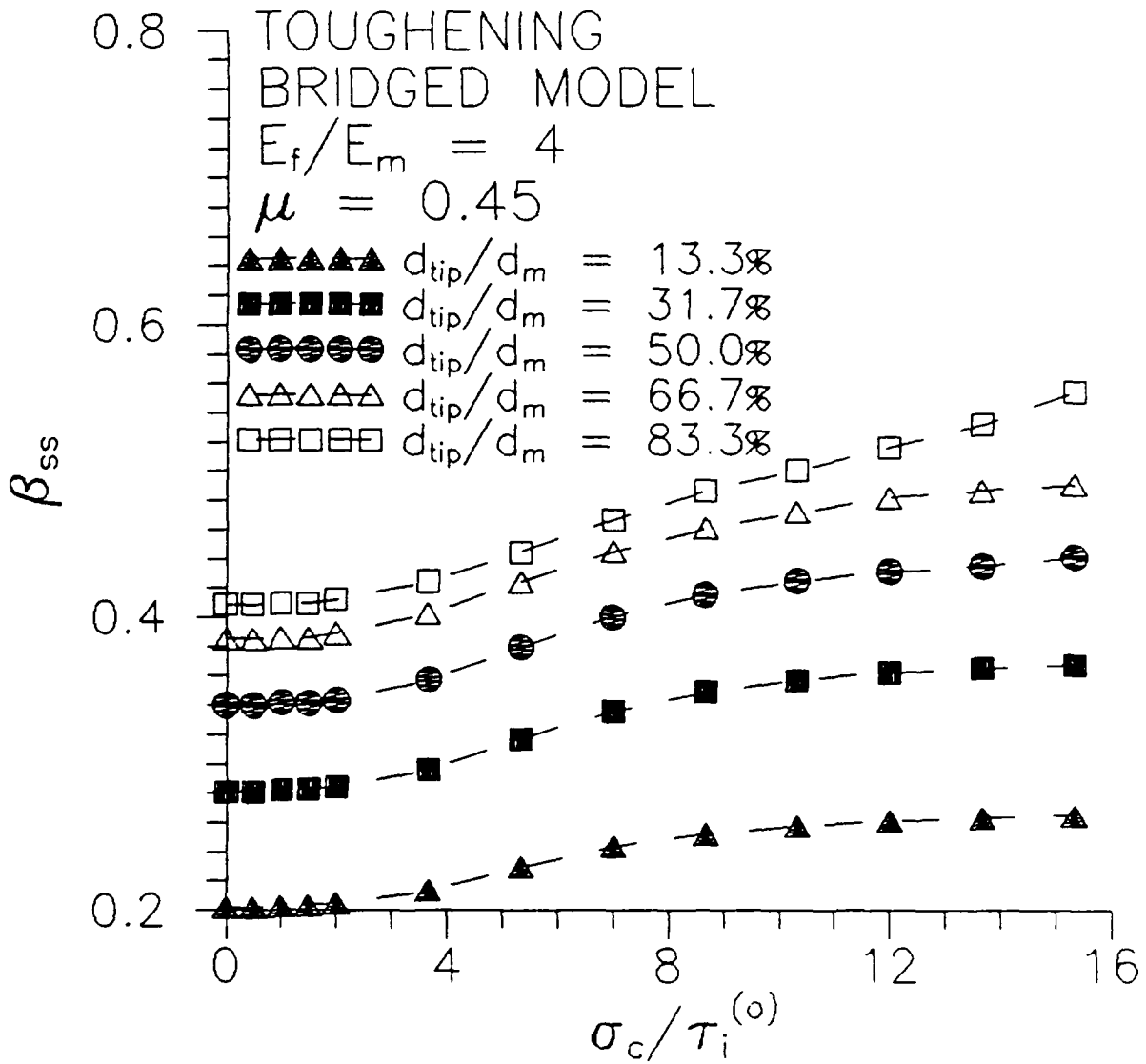
Figure 4.13c. Variation of the bridged toughening parameter β_{ss} with crack tip position d_{tip}/d_m and remote applied loading σ_c when $E_f/E_m = 4$ and $\mu = 0.45$.
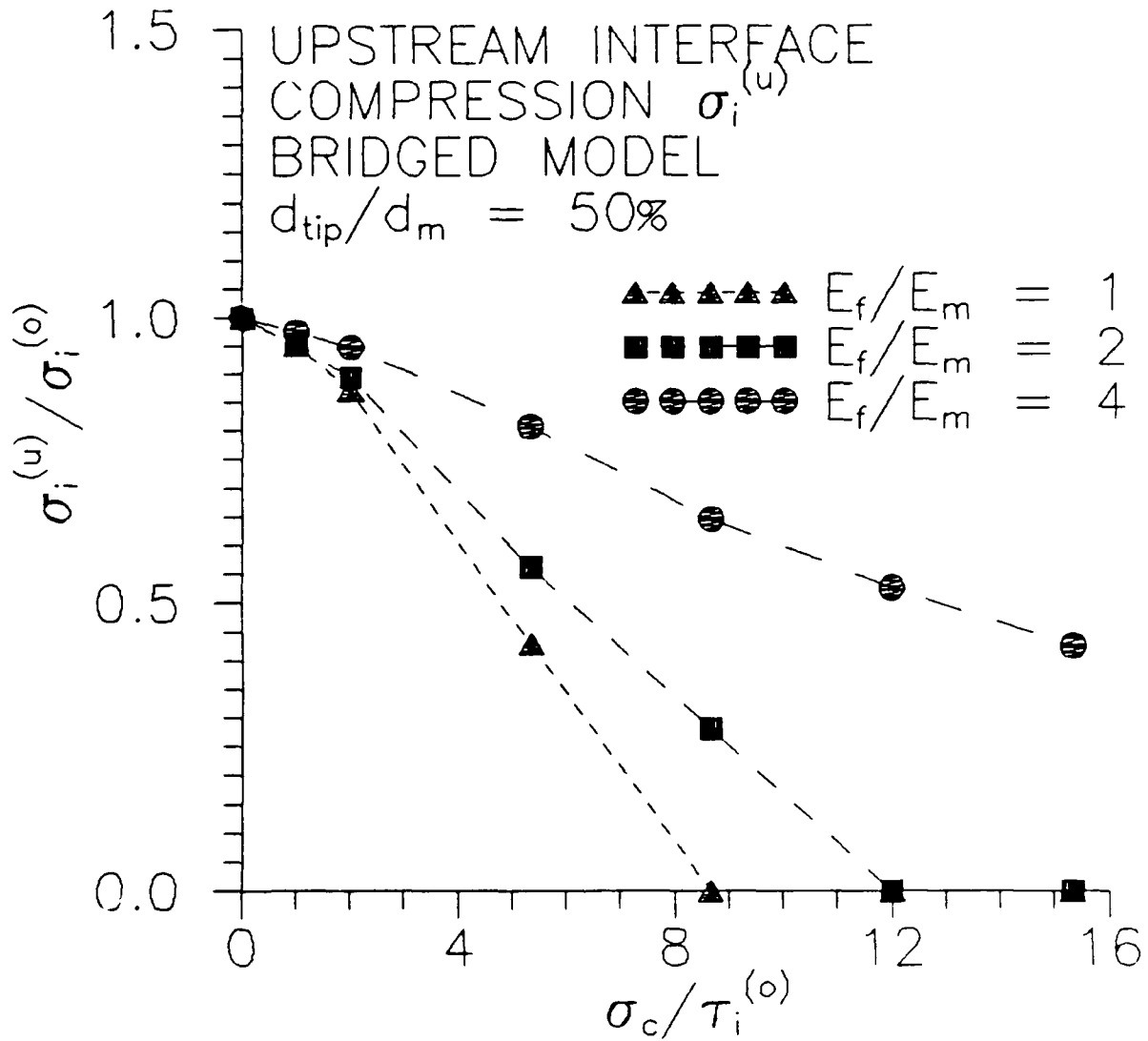
Figure 4.14. Variation of the immediate upstream interface compressive stress $\sigma_i^{(u)}$ in the bridged model with stiffness ratio E_f/E_m and remote applied loading σ_c when $\mu = 0.45$ and $d_{tip}/d_m = 50.0\%$.
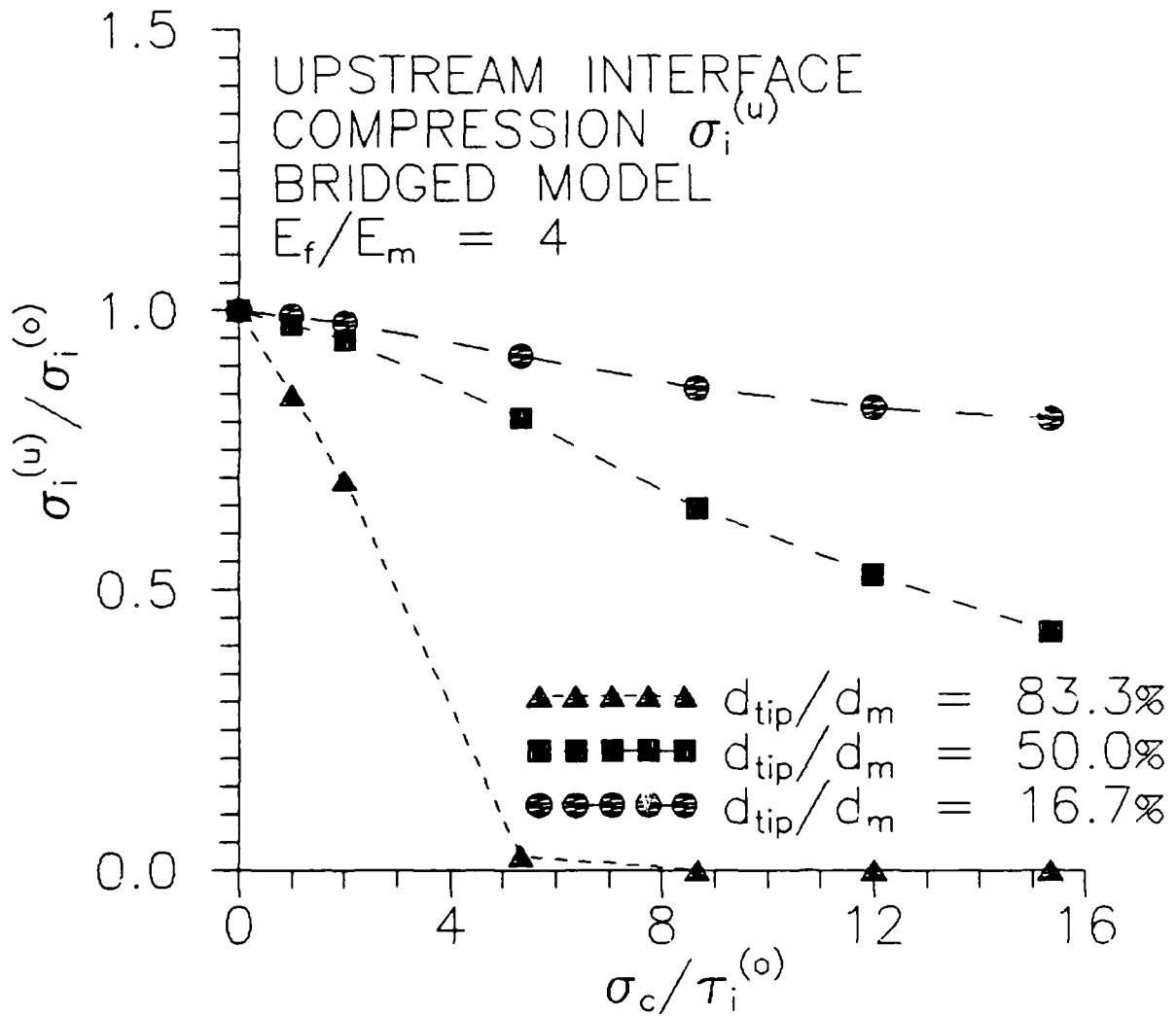
Figure 4.15. Variation of the immediate upstream interface compressive stress $\sigma_i^{(u)}$ in the bridged model with crack tip position d_{tip}/d_m and remote applied loading σ_c when $E_f/E_m = 4$ and $\mu = 0.45$.
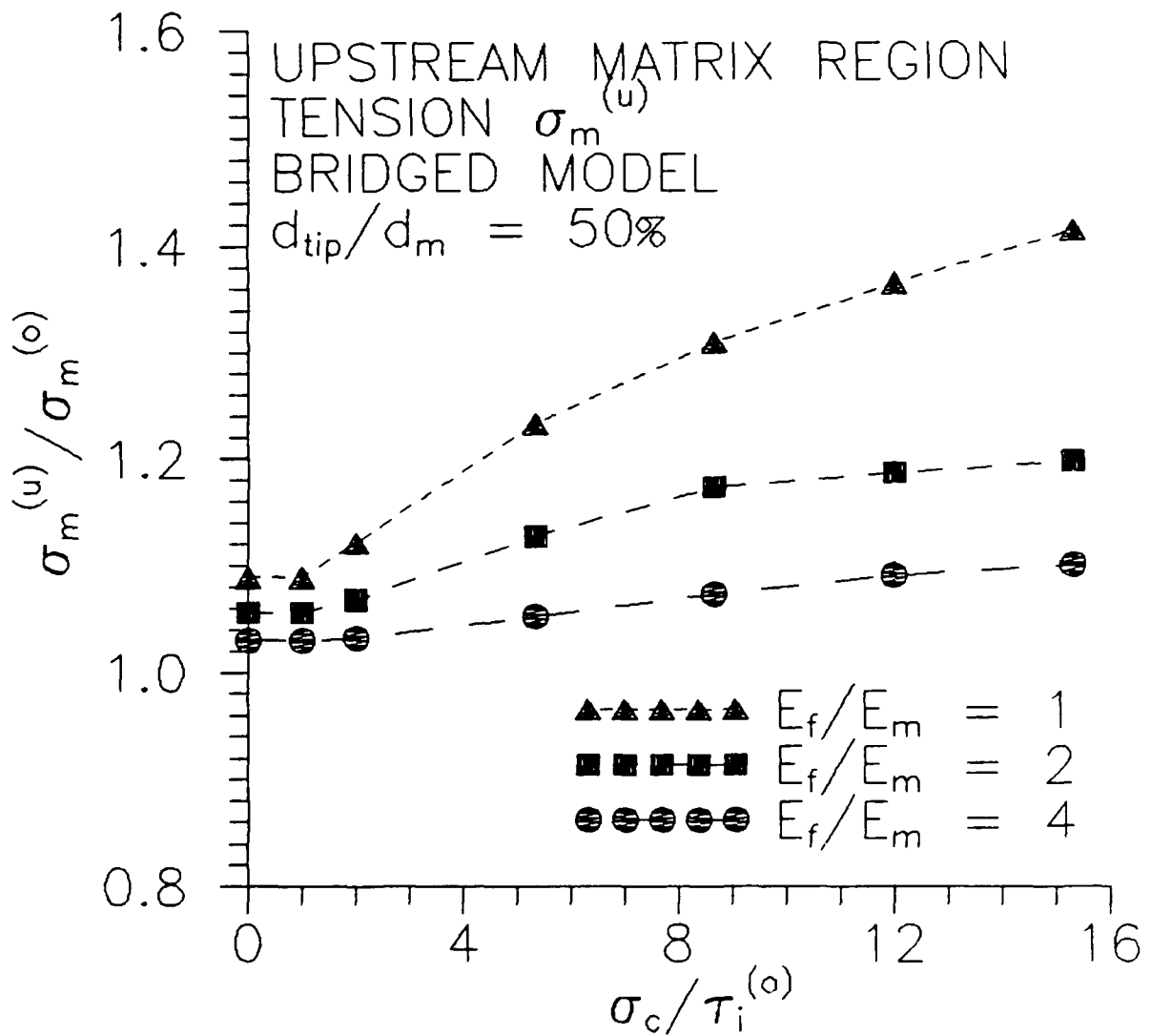
Figure 4.16. Variation of the highest principle stress in the first upstream matrix region $\sigma_m^{(u)}$ in the bridged model with E_f/E_m and remote applied load σ_c when $d_{tip}/d_m = 50.0\%$ and $\mu = 0.45$.
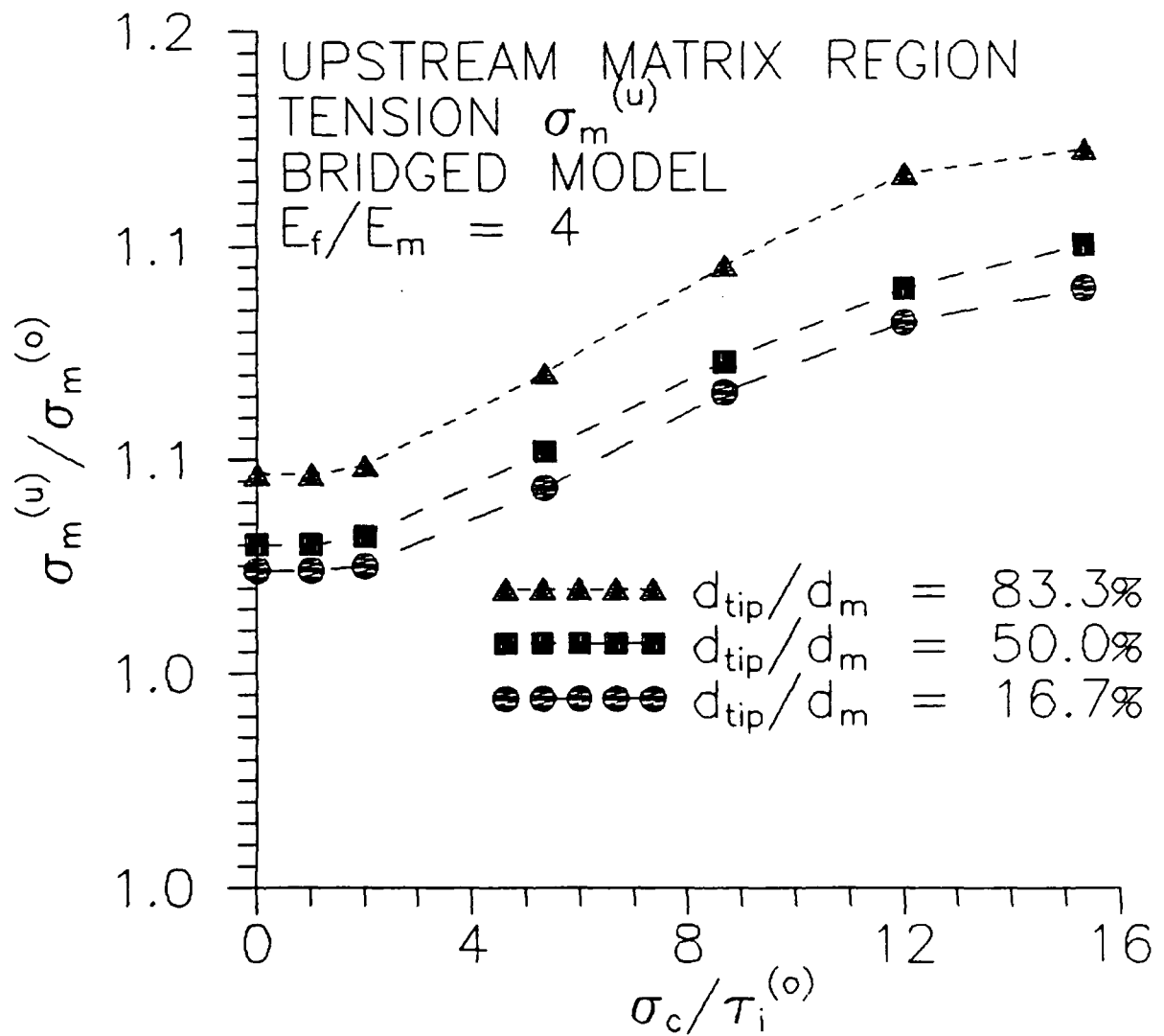
Figure 4.17. Variation of the highest principle stress in the first upstream matrix region $\sigma_m^{(u)}$ in the bridged model with d_{tip}/d_m and remote applied loading σ_c when $E_f/E_m = 4$ and $\mu = 0.45$.

APPENDIX 1

SLIPPING REGION INTERFACIAL SHEAR STRESS

The results of the finite element pullout model of Chapter 3 suggest that the interfacial shear stress may behave exponentially in y in the slipping region of the steady-state fiber pullout unit cell. A simplistic shear–lag mechanics argument supports this observation. From equilibrium we expect (roughly)

$$\langle \sigma_{yy} \rangle \; \alpha \; \int \tau_i \, dy + C \qquad (A.1)$$

where $\langle \sigma_{yy} \rangle$ is the average stress on any surface y = constant and τ_i is the interfacial shear stress. Due to Poisson effects and the constant displacement conditions at the vertical boundaries (see Fig. 3.2),

$$\sigma_i \; \alpha \; \langle \sigma_{yy} \rangle \qquad (A.2)$$

where σ_i is the interfacial normal stress. Also, Coulomb friction requires that

$$\tau_i = \pm \mu \sigma_i \qquad (A.3)$$

in the slipping region. Equations (A.1), (A.2) and (A.3) then yield

$$\tau_i \; \alpha \int \tau_i \, dy,$$

which is satisfied when the slipping interfacial shear stress τ_i is exponential.